LIFETIME MEASUREMENTS OF CERTAIN EXCITED STATES OF LEAD ISOTOPES

Thesis

presented by

RAMJEE PRASAD SINGH, B.Sc., M.Sc. (Patna)

for the degree of

DOCTOR OF PHILOSOPHY

University of Edinburgh

May, 1968.

ACKNOWLEDGEMENTS

I wish to express my gratitude to Professor N. Feather, F.R.S., for making available the facilities of the department. I am deeply indebted to my supervisor, Mr. J. Kyles, M.A., O.B.E., F.R.S.E., for all his helpful suggestions and guidance regarding the work presented in this thesis. Much of what I have learned during my study period here is due to his constant encouragement and sympathetic attitude.

All scientific research involves team work and the work described here being no exception, I would therefore like to thank all the members of the general workshop for assistance in the construction of the apparatus, and Mr. C. McAnna and his colleagues for the maintenance of the electronics. I am specially grateful to Mr. A. Headridge, ex-head of the technical staff, to Mr. D.F. Thompson, Chief Technician and to Mr. W.B. Wilson, Stores Manager, for the prompt attention that my requests have received from them at all times.

It is a pleasure to acknowledge my grateful thanks to Mr. J.C. McGeorge, B.Sc., for reading the manuscript and making several valuable suggestions, to Dr. K.C. Mathur, M.Sc., Ph.D. (Delhi) for his help in comparing the typescript and to Mrs. R.W. Chester for painstakingly typing the manuscript.

I would also like to record my gratitude to the University of Bihar, India, for the study leave and to the University of Edinburgh for the grant of a Post-graduate Studentship during part of the research period.

Finally, not least, I would like to thank my wife for her unfailing support throughout.

CONTENTS

C O N T E N T S (Contd.)

C O N T E N T S (Contd.)

CHAPTER I

INTRODUCTION

1.1 Electromagnetic Transitions and the Importance of Life-time Measurements

The predominant modes by which the majority of excited nuclear states decay to a state of lower excitation are the electromagnetic transitions which result from the interaction of the nucleus with the electromagnetic field. These electromagnetic modes of decay are, (i) γ-emission, (ii) internal conversion and (iii) internal pair production. The electromagnetic transitions have been classified into electric 2^{ℓ} pole and magnetic 2^{ℓ} pole types, the former involving a parity change of $(-1)^{\ell}$ and the latter of $(-1)^{\ell+1}$. Internal pair production can only occur when the energy available for decay is greater than 1.02 MeV which is the energy required for the production of an electron-positron pair. Internal conversion can always compete with γ-emission and becomes particularly important for low energy transitions of high multipolarities in elements of high Z number. The relative frequency with which γ-emission and internal conversion occur in a given transition is a matter of great importance in nuclear spectroscopy and is expressed by a quantity called the internal conversion coefficient. This coefficient is defined as $\alpha = \frac{N_e}{N_\gamma}$, the ratio of the number of electrons to the number of photons emitted.

Since, in principle, the electrons can be emitted from any shell, the total internal conversion coefficient α is given by

$$\alpha = \alpha_K + \alpha_L + \ldots\ldots ,$$

where α_K, α_L etc. refer to the coefficients related to the various atomic shells. Of course, unless higher multipoles are involved, the most strongly converted electrons are those in the K-shell. The conversion coefficient increases rapidly with the atomic number ($\sim$ as Z^3) and decreases as the γ-energy increases. The value of α has been tabulated by Rose[1] and also by Sliv and Band[2] as a function of these two variables and of the multipolarity of the transition. The two calculations are based on slightly different methods of treating nuclear size effects. Nevertheless, the results of the two calculations do not show any significant difference.

Since the electromagnetic field is well understood, the transition probability (T) for each of the decay processes can be calculated by the familiar methods of quantum electrodynamics. The total transition probability of the decaying state is the sum of the partial transition probabilities for each of these processes. The partial transition probabilities are given by the reciprocal of the corresponding mean lives ($T_\gamma = \frac{1}{\tau_\gamma}$ etc.) which are related to the partial level widths (Γ_γ, Γ_{ic}, Γ_{ip}) by the uncertainty principle. Thus, for radiative transitions,

$$\Gamma_\gamma \tau_\gamma \simeq \hbar$$

$$\text{or,} \quad \Gamma_\gamma \text{ (e.V.)} \simeq \frac{6.58 \times 10^{-16}}{\tau_\gamma \text{ (secs.)}} \qquad (1.1)$$

The transition probability for γ-emission from an excited state involves a function, $F(\ell, E')$ containing the multipolarity, ℓ and the decay energy, E' of the transition, and a factor, $B(6\ell, I_i \longrightarrow I_f)$, called the reduced transition probability (6 stands for the electric E or magnetic M type of transition). The latter depends sensitively on the wavefunctions of the two nuclear states involved in the transition. Because of this dependence, significant information regarding nuclear wavefunctions can be obtained from a comparison of experimental γ-decay transition probabilities with the theoretical values calculated on the basis of specific models of the nucleus. The enhancement or retardation given by $T_{exp.}/T_{th.}$ can be interpreted in terms of the adequacy or otherwise of the assumed model. In cases where the choice of model is sufficiently justified, the deviation leads to additional selection rules whose violation, while not completely inhibiting the transition, may retard it to a considerable extent. The lifetime measurements of excited nuclear states thus provide an invaluable tool for understanding nuclear structure.

1.2 Transition Probability for Radiative Emission[3,4,5]

The interaction energy between the nucleus and the radiation field giving rise to the emission and absorption of a photon is given by

$$H' = -\int \left[\frac{1}{c}\,\underline{J}(r).\underline{A}(r) + \underline{\mu}(r).\underline{H}(r)\right]dv \quad , \qquad (1.2)$$

where $\underline{J}(r)$ is the current density, $\underline{A}(r)$ is the vector potential of the electromagnetic field, $\underline{\mu}(r)$ is the magnetic dipole moment per unit volume due to the distribution of spins and $\underline{H}(r)$ is the magnetic field. $\underline{J}(r)$ is related to the charge density, ρ by the continuity equation,

$$\nabla.\underline{J} + \frac{\partial \rho}{\partial t} = \nabla.\underline{J} + \frac{i}{\hbar}\left[H, \rho\right] = 0 \qquad (1.3)$$

The electromagnetic field can be expanded in terms of the vector potentials (A) which are eigenstates of the angular momentum (J, J_Z and S^2) and parity operators. This effectively corresponds to the decomposition of the field into electric and magnetic multipoles. For a suitable choice of gauge, the vector potential A completely describes the field of radiation and satisfies the equations,

$$\Box \underline{A} = 0 \quad , \qquad \text{and} \qquad \text{div}\,\underline{A} = 0 \qquad (1.4)$$

In operator form, A can be expressed as,

$$A_E(\ell m) = \left(\frac{2}{\pi}\right)^{1/2} \frac{1}{\{\ell(\ell+1)\}^{1/2}}\ \frac{1}{k}\,(\nabla\times\underline{L})J_\ell(kr)Y_{\ell m}(\theta,\phi), \qquad (1.5)$$

and

$$A_M(\ell m) = \left(\frac{2}{\pi}\right)^{1/2} \frac{1}{\{\ell(\ell+1)\}^{1/2}} \underline{L}\, J_\ell(kr)\, Y_{\ell m}(\theta, \phi) \qquad (1.6)$$

where $A_E(\ell m)$ is the vector potential of the electric 2^ℓ pole field,

$A_M(\ell m)$ is the vector potential of the magnetic 2^ℓ pole field,

$k = \frac{2\pi}{\lambda}$ is the wave number of the emitted radiation

$\underline{L} = -i\underline{r}\times\underline{\nabla}$,

$J_\ell(kr)$ = spherical Bessel function of order ℓ.

and $Y_{\ell m}(\theta,\phi)$ = spherical harmonics of order (ℓm).

The electric and magnetic fields are given by

$$E = -\frac{1}{c}\frac{\partial A}{\partial E} \quad , \qquad H = \text{Curl } A \, , \qquad (1.7)$$

and their parities by $(-1)^\ell$ and $(-1)^{\ell+1}$ respectively. The transition probability per second for the interaction described by equation (1.2) which takes the charged system and the field from a state $|i\rangle$ to a state $|f\rangle$ is given by the golden rule

$$T = \frac{2\pi}{\hbar} \left| \langle f | H' | i \rangle \right|^2 \frac{dN}{dE'} \quad , \qquad (1.8)$$

where $\frac{dN}{dE'}$ denotes the number of possible final states per unit energy interval.

In the long wavelength approximation, $kr \ll 1$, which corresponds to energy less than 10 MeV,

$$J_\ell(kr) \sim \frac{(kr)^\ell}{(2\ell+1)!!} \quad ,$$

and the contribution of the spin part of the interaction energy in eq. (1.2) is negligible. With this approximation,

it can be shown that

$\langle f \mid H' \mid i \rangle$ is proportional to $\langle f \mid \mathcal{M}(\sigma\ell) \mid i \rangle$,

where $\mathcal{M}(\sigma\ell)$ stands for the operators associated with the electric or magnetic transition multipole moment. The transition multipole operators in such a case turn out to be identical with the operators of classical multipole moments given by

$$\mathcal{M}(E\ell) = \int \rho r^{\ell} Y_{\ell m}(\theta,\phi) dv \tag{1.9}$$

and

$$\mathcal{M}(M\ell) = \int \frac{e\hbar}{m'c} \cdot \frac{1}{\ell+1} \underline{L} \cdot \operatorname{grad}(r^{\ell} Y_{\ell m}) dv \tag{1.10}$$

The multipole moment operators are irreducible tensors of rank ℓ, and their matrix elements for nuclear states of angular momentum I_i and I_f can be expressed by using the Wigner-Eckart theorem,

$$\langle I_f m_f \mid \mathcal{M}(\sigma\ell) \mid I_i m_i \rangle = (-1)^{I_f - m_f} \begin{pmatrix} I_f & \ell & I_i \\ -m_f & m & m_i \end{pmatrix} \times \langle I_i \| \mathcal{M}(\sigma\ell) \| I_f \rangle , \tag{1.11}$$

where the last factor is the reduced matrix element and $\begin{pmatrix} I_f & \ell & I_i \\ -m_f & m & m_i \end{pmatrix}$ is the Wigner 3j symbol.

The off-diagonal elements of the multipole operators give the transition multipole moments, whereas the static electromagnetic moments are given by the diagonal matrix elements of the same operators. The transition probability from a nuclear state $|I_i m_i\rangle$ to another nuclear state

$|I_f m_f\rangle$ of parities π_i and π_f respectively by emission (or absorption) of electromagnetic 2^ℓ pole radiation can, therefore, be written as

$$T(\sigma\ell;\ m_i \to m_f) = \frac{8\pi(\ell+1)}{\ell\left[(2\ell+1)!!\right]^2} \cdot \frac{1}{\hbar} k^{2\ell+1} \left|\left\langle I_f m_f \middle| \mathcal{M}(\sigma\ell) \middle| I_i m_i \right\rangle\right|^2 \tag{1.12}$$

Summing over all possible photon directions and polarisations gives the total transition probability,

$$T(\sigma\ell;\ I_i \to I_f) = \frac{1}{2I_i+1} \sum_{m_i, m_f} T(\sigma\ell;\ m_i \to m_f) \tag{1.13}$$

or

$$T(\sigma\ell;\ I_i \to I_f) = \frac{8\pi(\ell+1)}{\ell\left[(2\ell+1)!!\right]^2} \cdot \frac{1}{\hbar} k^{2\ell+1}\ B(\sigma\ell;\ I_i \to I_f), \tag{1.14}$$

where $B(\sigma\ell;\ I_i \to I_f)$ is the reduced transition probability for an electromagnetic 2^ℓ pole transition. For emission of radiation

$$B(\sigma\ell;\ I_i \to I_f) = \sum_{m_i, m_f} \left|\left\langle I_f m_f \middle| \mathcal{M}(\sigma\ell) \middle| I_i m_i \right\rangle\right|^2 \tag{1.15}$$

Using the orthogonality relation of the Wigner 3j symbol, this reduces to

$$B(\sigma\ell;\ I_i \to I_f) = \frac{1}{2I_i+1} \left|\left\langle I_f \middle\| \mathcal{M}(\sigma\ell) \middle\| I_i \right\rangle\right|^2 \tag{1.16}$$

The reduced transition probability for absorption $B(\sigma\ell;\ I_f \to I_i)$ is related to the reduced transition probability for emission $B(\sigma\ell;\ I_i \to I_f)$ by

$$B(\sigma\ell;\ I_f \to I_i) = \frac{2I_i+1}{2I_f+1}\ B(\sigma\ell;\ I_i \to I_f) \tag{1.17}$$

On writing eq. (1.14) explicitly for $E\ell$ and $M\ell$ radiations,

$$T(E\ell;\ I_i \rightarrow I_f) = \frac{8\pi(\ell+1)}{\ell\left[(2\ell+1)!!\right]^2} \cdot \frac{1}{\hbar} k^{2\ell+1} B(E\ell;\ I_i \rightarrow I_f) \tag{1.18}$$

and

$$T(M\ell;\ I_i \rightarrow I_f) = \frac{8\pi(\ell+1)}{\ell\left[(2\ell+1)!!\right]^2} \cdot \frac{1}{\hbar} k^{2\ell+1} B(M\ell;\ I_i \rightarrow I_f) \tag{1.19}$$

Eqs. (1.18) and (1.19) express the transition probabilities independent of any nuclear model and depend only on the properties of the radiation field. The selection rules governing the transition rates expressed by these equations are given by the conservation of angular momentum and parity:

$$\left|(I_i - I_f)\right| \leqslant \ell \leqslant (I_i + I_f) \tag{1.20}$$

$$\left.\begin{aligned} \Delta\pi = \pi_i\pi_f &= (-1)^{\ell} \quad \text{for } E\ell \text{ radiation} \\ &= (-1)^{\ell+1} \quad \text{for } M\ell \text{ radiation} \end{aligned}\right\} \tag{1.21}$$

$\Delta\pi = +1$ means that the initial and final states have the same parity, while $\Delta\pi = -1$ signifies a change of parity. It is obvious from eqns. (1.18) and (1.19) that the probability of emission for the higher multipoles decreases rapidly with increasing ℓ, and hence, although in principle all multipoles satisfying the selection rules (1.20) and (1.21) can occur simultaneously in a transition, in practice only the lowest multipoles are observed. However, when the lowest order radiation is magnetic, a multipole mixture is frequently observed, the most common being

M1 + E2. Since a multipole radiation with $\ell = 0$ does not exist, relation (1.20) implies that a radiative transition between two states with angular momentum $I_i = I_f = 0$ is absolutely forbidden,

$$\text{i.e.} \quad I_i = 0 \longrightarrow I_f = 0 \quad \text{(forbidden)} \qquad (1.22)$$

A $0 \rightarrow 0$ transition may, however, proceed by internal conversion and also by pair formation whenever the available energy is greater than 1.02 Mev.

1.3 The Single Particle Estimates[3,4]

A rough estimate of the transition probability has been made, independently, by Weisskopf and Moszkowski, on the assumption that the radiation is caused by a transition of one single proton which moves independently in a central potential. The wavefunction of the proton in the initial and final state can be written as a product of (a) the radial function $R_{n\ell}(r)$ which depends on the details of the potential, and (b) a spin-angular part $\phi(JM)$ independent of the potential. Thus, the electric multipole matrix element can be written as

$$\left\langle f \mid \mathcal{M}(E\ell) \mid i \right\rangle = \int_0^\infty e\, R_f\, r^\ell\, R_i\, r^2 dr \int_{4\pi} \phi_f Y_{\ell m}(\theta,\phi) \phi_i \, d\Omega , \qquad (1.23)$$

where $d\Omega$ refers to integration over all angles and summation over spins. The $E\ell$ transition rate for a single proton can then be written as

$$T(E\ell;\ I_i \rightarrow I_f) = \frac{2(\ell+1)e^2}{\ell[(2\ell+1)!!]^2}\ \frac{R_o^{\ell}}{\hbar}\ k^{2\ell+1}\ S(I_i, \ell, I_f)$$

$$\int_o^{\infty} R_f\ r^{\ell}\ R_i\ r^2\ dr\ , \qquad (1.24)$$

where $S(I_i,\ \ell,\ I_f)$ is a statistical factor arising from the angular integration and is given by

$$S(I_i, \ell, I_f) = (2I_f + 1)\ [C(I_i I_f\ \ell;\ \tfrac{1}{2}, -\tfrac{1}{2}\ 0)]^2 \qquad (1.25)$$

C is the Clebsch-Gordan Coefficient, and R_o is the nuclear radius. The value of S for all relevant cases has been tabulated by Bohr and Mottelson. The radial integral has been evaluated on the assumption that the radial wave functions, R for both initial and final states are constant throughout the interior of the nucleus $(r < R_o)$ and vanish outside $(r > R_o)$. On the basis of this constant density model of the nucleus, the radial integrals are given by

$$\int_o^{\infty} R_f\ r^{\ell}\ R_i\ r^2\ dr = \frac{3R_o^{\ell}}{\ell+3} \qquad (1.26)$$

The transition probability for an $E\ell$ radiation can, therefore, be finally expressed as

$$T_W^{E\ell} = \frac{4.4(\ell+1)}{\ell[(2\ell+1)!!]^2}\ \left(\frac{3}{\ell+3}\right)^2\ \left(\frac{E'}{197\ \text{MeV}}\right)^{2\ell+1}\ R_o^{2\ell}\ S(I_i\ \ell\ I_f)$$

$$\times\ 10^{21}\ \text{sec.}^{-1} \qquad (1.27)$$

where R_o is in units of 10^{-13} cms.

A similar treatment gives for $M\ell$ transitions,

$$T_W^{M\ell} = \frac{1.9(\ell+1)}{\ell[(2\ell+1)!!]^2}\ \left(\frac{3}{\ell+3}\right)^2\ \left(\frac{E'}{197\ \text{MeV}}\right)^{2\ell+1}\ R_o^{2\ell-2}$$

$$S(I_i\ \ell\ I_f) \times 10^{21}\ \text{sec.}^{-1} \qquad (1.28)$$

The transition probabilities given by (1.27) and (1.28) are known as Weisskopf single particle estimates. These estimates for various multipoles, are listed in Table 1.

While Moszkowski's formula for electric transitions agrees with Weisskopf's, there is a slight difference in the case of magnetic transitions, the Moszkowski estimate being given by

$$T^{M\ell}_{(Mosz)} = \frac{0.19(\ell+1)}{\ell\,[(2\ell+1)!!]^2}\left(\frac{3}{\ell+2}\right)^2 \left(\mu_p \ell - \frac{\ell}{\ell+1}\right)\left(\frac{E'}{197\ \text{MeV}}\right)^{2\ell+1} \times$$

$$R_o^{2\ell-2} \times S(I_i\ \ell\ I_f) \times 10^{21}\ \text{sec.}^{-1} \qquad (1.29)$$

$(\mu_p = 2.79)$

These expressions, though derived for a proton transition, are used as standards for comparison of all experimental transition rates without any distinction between neutron and proton transitions. However, for El radiations, the single particle estimates may be multiplied by a factor of $1/4$ in both the neutron and the proton case to allow for the orbital motion of the nucleus around the centre of mass of the whole nucleus.

The single particle estimates apply only to the partial transition probability for the γ-ray emission whereas what one gets experimentally is the total transition probability for the multipole radiation. Hence, in order to compare the experimental transition probability with the theoretical estimates, the former has to be divided by $1+\alpha$ to take into account the extra transitions caused by

Table 1

Weisskopf Single Particle Estimates

Multipolarity	T_W^{SP} in sec.$^{-1}$
E1	$1.03 \times 10^{14} A^{2/3} E_\gamma^{\ 3}$
M1	$3.09 \times 10^{13} E_\gamma^{\ 3}$
E2	$0.74 \times 10^{8} A^{4/3} E_\gamma^{\ 5}$
M2	$0.22 \times 10^{8} A^{2/3} E_\gamma^{\ 5}$
E3	$0.35 \times 10^{2} A^{2} E_\gamma^{\ 7}$

internal conversion. Thus, the actual radiative transition probability is given by

$$T = T_{exp} / 1+\alpha \quad .$$

In many cases, a given level decays by the emission of several parallel multipole radiations. The experimental measurement in such cases provides the total life-time of the level from which the radiative life-time of any particular multipole emission can be determined if the intensities of the various competing transitions are known.

1.4 Comparison of Experimental Transition Probabilities with Single Particle Estimates.

A general study of the experimental results on life-time measurements of E1 and M1 transitions reveals the following facts[6]:

(a) E1 transitions are all slower by a factor which is widely spread between 1 and 10^{16}. This hindrance factor is in general larger in heavy nuclei than in light ones.

(b) M1 transitions cluster around a hindrance of 100 in the range 1 - 10^6, though in a few cases an enhancement of up to 10 has also been observed. Statistically, there is a noticeable trend towards the Weisskopf value as energy increases.

Although a discussion of higher multipole transitions is not relevant to the work presented in this thesis, it may be mentioned that in contrast with other multipoles, the majority of E2 transitions are enhanced. The enhancement factors, while always less than 1000, lie mostly

between 10 and 500.

In view of the fact that the Weisskopf estimates are based on a very naive picture of the nucleus, the statements made above are not surprising. Nevertheless, the various refinements in the nuclear model[7-11] - shell model with configuration mixing, Nilsson model envisaging individual particle motion in spheroidal potential and rotational vibrational model of Bohr and Mottelson - have gone a long way in explaining the observed discrepancies. It is now well known that the large enhancements of the E2 transitions in the region of deformed nuclei, particularly in the rare earths, are due to the collective motion superimposed on the intrinsic shell model structure of the Nilsson type. For El transitions in heavy nuclei the agreement between theory and experiment is not very good, though the gap has been considerably bridged by extending the Nilsson model to include the effects of nucleon pairing correlation, coriolis coupling and octupole vibration-particle coupling. Such stipulations impose additional selection rules apart from those given by (1.20) and (1.21), and the enhancement or retardation of a particular transition is interpreted in terms of the degree to which these rules are violated.

For low Z nuclei, the concept of isotopic spin (T) as a good quantum number under conditions of charge independence leads to the selection rules,

$$\Delta T = 0, \pm 1 ,$$

with a stronger rule for El transitions,

$$T = 0 \rightarrow T = 0 \quad \text{(forbidden)},$$

and for self-conjugate nuclei $(N = Z)$,

$$\Delta T = 0 \qquad \text{(forbidden)}.$$

An additional single particle selection rule for M1 transitions is

$$\left.\begin{aligned} \ell_i &= \ell_f \\ n_i &= n_f \end{aligned}\right\} \quad \text{(allowed)}$$

This implies that only spin flip M1 transitions of the type $1p_{3/2} \rightarrow 1p_{1/2}$ would be allowed. Nevertheless, M1 transitions with $\Delta\ell = 2$ and $\Delta I = 1$ have been observed and ascribed to configuration mixing. In odd Z nuclei such ℓ-forbidden transitions are found to be retarded[12, 13]. In odd N nuclei, on the other hand, the ℓ-forbidden transitions are observed[14] to be fast by a factor of ~ 5. The reason for this enhancement is not known. The systematics of forbiddenness of E1 and M1 transitions in low Z nuclei has been reviewed by Wilkinson[15].

The large retardations for the E1 transitions in distorted nuclei are usually explained in terms of the K-selection rule of the unified model and the selection rules for transitions between intrinsic particle states of the Nilsson model. The K-selection rule of Alga[16] governing the transitions of multipolarity ℓ between states of different rotational bands is

$$\Delta K = |K_i - K_f| < \ell \qquad \text{(allowed)}$$

where K is the total angular momentum along the symmetry axis of the nucleus. This rule is strictly obeyed when the

intrinsic and rotational motions are completely independent. If $\Delta K > \ell$, the transition is forbidden. The degree of forbiddenness represented by $\nu = \Delta K - \ell$ determines the extent to which the transitions are retarded. Examples of K-forbiddenness have been observed in Tm^{169}, Os^{190}, Hf^{178} and many other nuclei. K-forbiddenness also explains why the E1 transitions in distorted nuclei usually do not go to the ground state.

The quantum numbers used for the classification of the intrinsic particle states described in the Nilsson model are N, η_z, Λ and Σ, where N is the principal oscillator quantum number, η_z is the oscillator quantum number along the symmetry axis of the nucleus, Λ is the orbital angular momentum along this axis, and Σ is the component of intrinsic spin along the symmetry axis. Obviously, $K = \Lambda + \Sigma$. N, η_z, Λ and Σ are called the asymptotic quantum numbers. The selection rules governing the change in these quantum numbers for E1 transitions are reproduced in Table 2 from reference (16).

Table 2

Multipole	ΔK	ΔN	$\Delta \eta_z$	$\Delta \Lambda$	$\Delta \Sigma$
E1	± 1	± 1	0	1	0
	0	± 1	± 1	0	0

Selection rules for allowed changes in asymptotic quantum numbers.

These rules seem to provide an adequate explanation for the

hindrance of E1 transitions in many distorted odd A nuclei. Several authors have considered the effects of coriolis mixing (rotation-particle coupling) in attempting to explain the remaining anomalies. In some E1 transitions with $\Delta K = \pm 1$ the general agreement is found to improve when the retarding effects of the pair correlations between the nucleons is taken into account, though the same procedure causes poorer agreement for $\Delta K = 0$ transitions. There is no answer to this puzzling anomaly. Based on these lines of approach, several papers[17-20] devoted to the retardation of E1 transitions in deformed odd A nuclei have appeared in the past few years. The general conclusion seems to be that although the Nilsson model represents a large improvement over the spherical shell model, the theoretical predictions still remain unsatisfactory. By extending the Nilsson model to two particle states, Conlon et al.[20] have provided an explanation for the retardation of the 67 keV E1 transition in $_{71}Lu^{172}$ and also of the 391 keV E1 transition in $_{74}W^{180}$. The 391 keV E1 γ-ray in W^{180} is ascribed to the transition $K^{I\pi} = 8, 8, - \rightarrow 0, 8, +$ thus making it heavily K-forbidden ($\Delta K = 8$). This is in agreement with the prediction $\Delta K = 7.3$ of Rusinov's empirical formula for the K-forbiddenness of E1 transitions in even-even nuclei,

$$\log_{10} \frac{1}{|M|^2} \approx 2(\Delta K - \ell) , \qquad (1.30)$$

where $|M|^2$ is the reduced matrix element. W^{180} is one

of only a few heavy even-even nuclei in which the retardation of El transition has been theoretically accounted for. It must be admitted that, in general, the reasons for the hindrance of El transitions in such nuclei are not well understood, and hence much remains unexplained.

1.5 The Object of the Present Experiment

A lifetime measurement of the 1720 keV El transition in $_{82}Pb^{206}$ following K-capture decay of $_{83}Bi^{206}$ is presented in this work. Two values for the lifetime of this transition have already been published. The first measurement performed in 1959, by Brunner et al.[21], gave a retardation of about 50 compared with the single particle estimates, whereas in more recent work, Wu et al.[22] have reported a retardation of about 600. Both groups have obtained the lifetime by measuring the intensity of the monoenergetic K-positron associated with this transition. The reason for the observed discrepancy is not obvious, though it is certainly not surprising because of the uncertainties involved in the estimation of the positron intensity. This will be discussed more fully in section 2.7 where lifetime measurements by observations on monoenergetic positron emission will be described. Of all the existing methods of lifetime measurement, no other is suitable for such El transitions, and hence no alternative method of checking the results is available.

A new method for measuring the lifetime of El transitions based on the observations of K-X ray satellites

associated with such transitions has been evolved in this laboratory and already applied[23] to the 1409 keV E1 transition in Sm^{152}. As a further test, this new method is applied in the present work to the 1720 keV E1 transition of Pb^{206}. The choice of this particular transition is because of the existing discrepancy referred to above. Before the new method is described in Chapter IV, the existing methods of lifetime measurement are reviewed in Chapter II. Chapter III is a collection of information on X-ray satellites and other associated phenomena relevant to later discussions.

CHAPTER II

LIFETIME MEASUREMENTS OF NUCLEAR EXCITED STATES

This chapter presents a brief resume of the existing methods for measuring lifetimes of the nuclear excited states in the range 10^{-6} - 10^{-16} seconds. It is not intended to go into the details of the experiments, rather only the principles and techniques involved are outlined.

The important methods of lifetime measurements may be listed as follows:-

(1) Delayed coincidence method.

(2) Recoil and Doppler shift method.

(3) Nuclear Resonance Fluorescence method.

(4) Mössbauer effect.

(5) Coulomb excitation method.

(6) Inelastic electron scattering method.

(7) Monoenergetic positron emission method.

2.1 Delayed Coincidence Method

The fundamental principle involved in a delayed coincidence experiment is that a coincidence circuit produces an output pulse only when it has received two input pulses within a short time, τ_o of each other. τ_o is called the resolving time of the coincidence unit. The use of coincidence method in measuring the mean life of a nuclear excited state may be understood from figures 1(a) and 1(b).

Let X_1 and X_2 be two nuclear radiations emitted

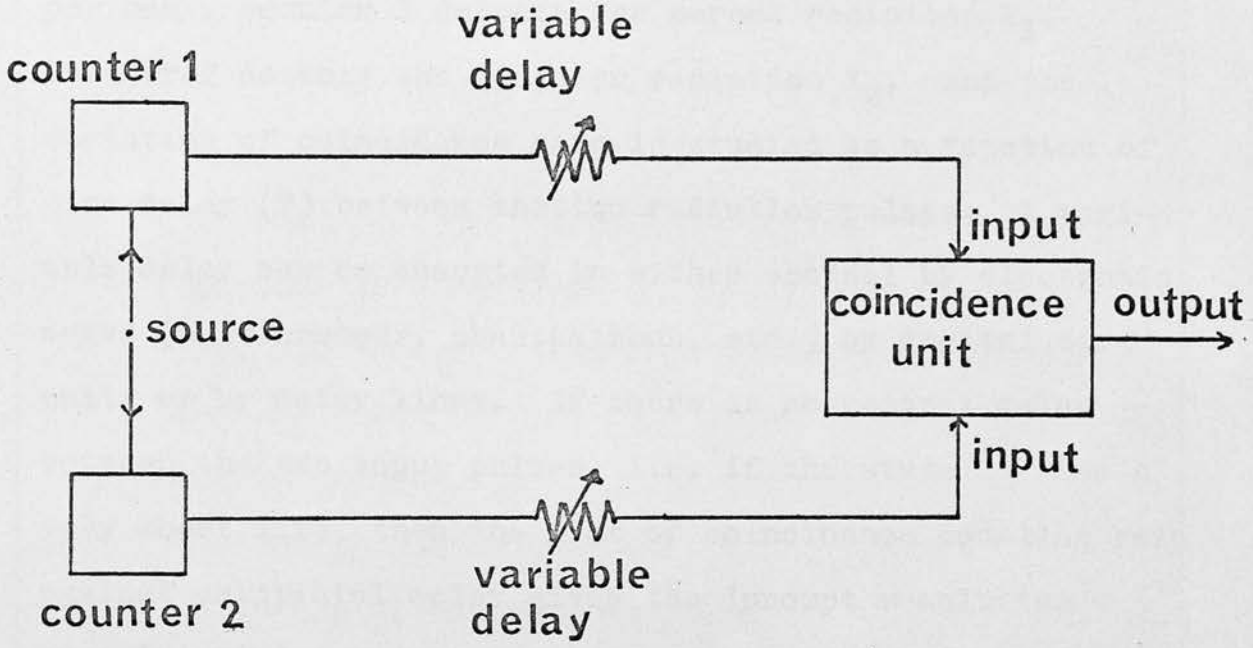
counter 1
variable
delay
input
coincidence
unit
output
source
input
counter 2
variable
delay

(a)

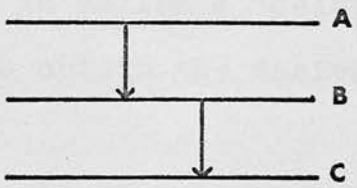
A
B
C

(b)

FIG.1

in cascade, and B be the excited state whose mean life, τ, is to be determined. In a typical coincidence experiment, counter 1 detects the parent radiation X_1, counter 2 detects the daughter radiation X_2, and the variation of coincidence rate is studied as a function of time delay (T) between the two radiation pulses. A variable delay can be inserted in either channel by electronic means (univibrators, phantastrons, etc.), by digital circuits or by delay lines. If there is no natural delay between the two input pulses, i.e. if the state B has a very short life, then the plot of coincidence counting rate against artificial delay gives the 'prompt resolution curve', P(x). But if the state B has a measurable life, the experiment then provides the time distribution, $e^{-T/\tau}$ of the coincidence rate as a function of T. The plot F(x) in this case is called a 'delayed resolution curve', and can be used to obtain the desired mean life of the state B .

The delayed coincidence experiment can be done in two different ways. In the integral delayed coincidence method developed by Feather and Dunworth[24], the parent pulses X_1 are stretched to a known duration T by pulse shaping circuits, while the daughter pulses X_2 are kept relatively short. The coincidence counting rate as a function of T is given by

$$1 - e^{-T/\tau} \quad .$$

For any particular value of T, the measured coincidence rate is the integral of the desired time distribution from

$T = 0$ to $T = T$. The original form of the time distribution, $e^{-T/\tau}$ is obtained by differentiating the measured curve, or which amounts to the same thing in practice, by taking the difference between the successive readings. This method was used to measure the half-lives of the members of the α-emitting series Po^{216} ($T_{1/2} = 0.16$ sec.) to Po^{212} ($T_{1/2} = 3 \times 10^{-7}$ sec.).

In the differential delayed coincidence method, both the pulses X_1 and x_2 are kept fixed in length, but X_1 is delayed by a known time T and the coincidence rate is studied as a function of the time delay. For any value of T, the coincidences recorded are those which occur in the interval $T \rightarrow T + \tau_o$. Hence the coincidence counting rate as a function of T is given by $e^{-T/\tau}$ which represents just an ordinary radioactive decay of the state B. The mean life of the state can be determined from a logarithmic plot of the coincidence rate against T.

Since the differential method gives the mean life of the state in a straight-forward manner, it has been universally adopted for lifetime measurements in its range of application. The integral method now remains of historical importance only.

The delayed coincidence method can be very conveniently used if the resolving time of the circuit is smaller than the lifetime to be measured. But as the resolving time of a coincidence circuit is limited, among other factors, by the speed of the detector, it puts a limitation on the applicability of this method. It was for this

reason that in the early years of nuclear spectroscopy when ionisation chambers with response time $\sim 10^{-6}$ seconds were the only detectors available, the lifetime measurement was confined only to the microsecond region. With the development of scintillation and solid state detectors having response time in the region of 10^{-9} - 10^{-10} seconds, it is now possible to have a resolving time of this order and measure lifetimes in the nanosecond region. The theoretical works of Bay[25] and Newton[26] on the interpretation of the results of the delayed coincidence experiments have led to a method of measuring mean lives much shorter than the smallest available resolving time. The method consists of a comparison between the delayed resolution curve obtained with the source under investigation and the prompt resolution curve obtained with a radiation of similar energy whose lifetime is very short. As shown by Bay, the desired mean life of the state is given by the displacement of the centroids of the curves $F(x)$ and $P(x)$, the position of the centroids being determined by a numerical integration procedure for the two curves. Bell et al.[27] have applied this idea to the lifetime measurement of the 158 keV γ-transition in Hg^{199} following β-decay of Au^{199}. These authors used a pair of lens β-spectrometers placed end to end, each being provided with a scintillation detector. The source was mounted on a thin film at the centre of the spectrometers. The delayed resolution curve, $F(x)$ was obtained by focussing one of the spectrometers on the L-conversion peak of the 158 keV Hg^{199} γ-ray and the second on the continuum of the nuclear β-rays from Au^{199}. In order to obtain

the prompt resolution curve, $P(x)$, the Au^{199} source was replaced by a Th B source and coincidences were observed between the F-line of Th B and the β-rays. The plots of $F(x)$ and $P(x)$ on linear and logarithmic scales are shown in figure 2. The half-life of the 158 keV transition as measured from the centroid shift was $(2.43 \pm .12) \times 10^{-9}$ seconds. The two curves intersect each other at the maximum of $F(x)$, and for $F(x) \gg P(x)$, the former falls off as $e^{-T/\tau}$. The half-life obtained from the slope of the falling part of $F(x)$ was $(2.26 \pm .12) \times 10^{-9}$ sec.

By a slight variation of the above technique, Bell et al.[27] evolved a self comparison method in which the delayed resolution curve is compared not to the prompt resolution curve but to its own inverse, i.e. to the delayed resolution curve obtained by reversing the roles of the two counters. Obviously, the centroid shift in this case will be 2τ. Using this method the authors found the lifetime of the 412 keV γ-transition in Hg^{198} following β-decay of Au^{198} to be $(1.0 \pm 1.7) \times 10^{-11}$ seconds.

In another variation of the delayed coincidence method which is useful for non-radioactive isotopes, a pulsed beam of particles is used to produce any particular excited state in the target nucleus by Coulomb excitation. A delayed coincidence experiment between the delayed radiation from the state so formed and the electrical pulse exciting the accelerated beam gives the lifetime of the excited state in the usual way. Several groups of workers have used this method to produce and measure the mean life

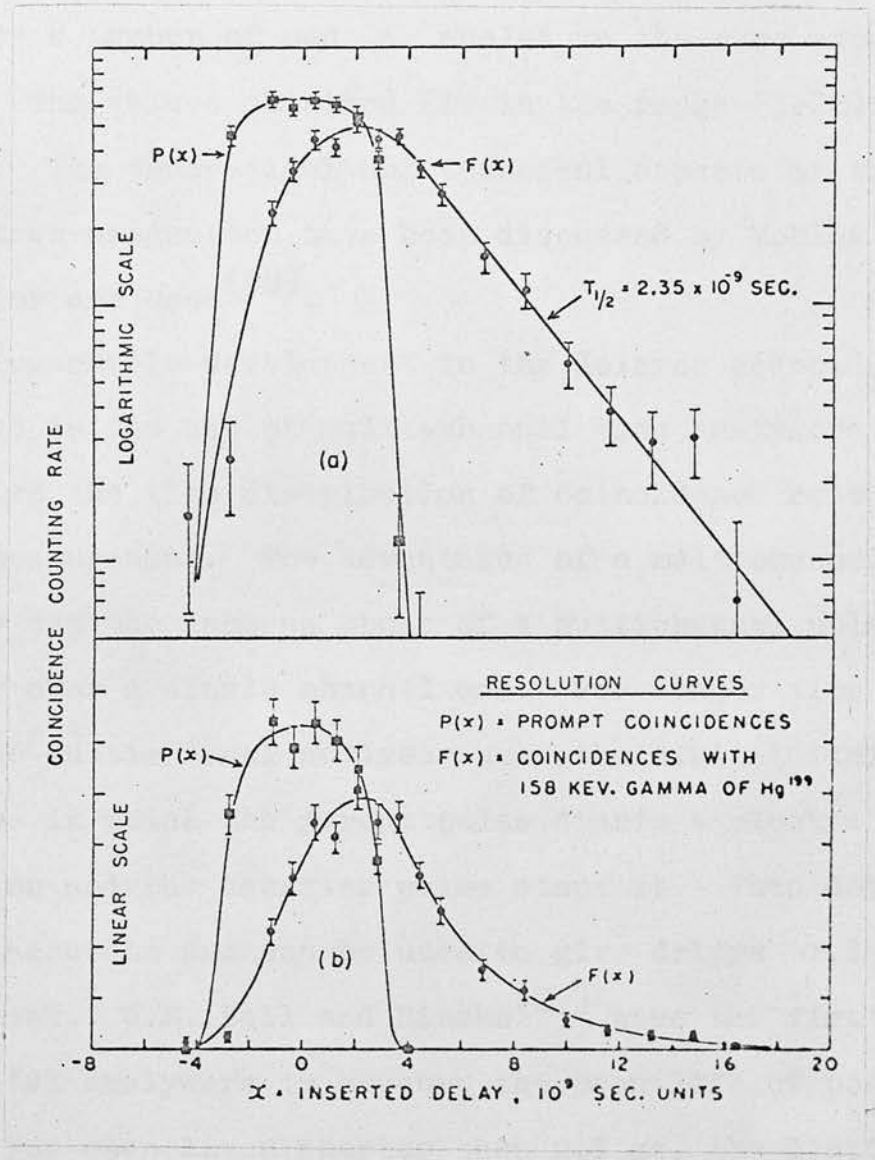

Fig. 2. Prompt and delayed resolution curve (Ref. 27).

of the first 2+ excited state in a number of even-even rotational nuclei. Using an ultrafast pulse technique which gave a time resolution of 7×10^{-11} seconds, Goldring[28] measured the mean life of some low lying levels in a number of odd A nuclei in the rare earth region. The values obtained lie in the range $(3\text{-}20) \times 10^{-11}$ seconds. The theoretical and technical aspects of the pulsed beam production have been discussed by Mobley[29], and Fowler and Good[30].

A remarkable development in the delayed coincidence technique is the use of multi-channel time analysers which give the time distribution of coincidence rate in a single measurement. The advantages of a multichannel time analyser are the same as those of a multichannel pulse analyser over a single channel one. For longer time intervals, the multichannel analyser uses the digital timing apparatus in which the parent pulse starts a clock oscillator and the daughter pulse stops it. This device is very accurate and can be used to give delays 0.1 μs per channel. W.E. Bell and Hincks[27] were the first to use digital analysers to measure the mean life of positive muons. For mean lives shorter than 0.1 μs, the digital device is replaced by time to amplitude converters. In this device, the time interval between the two input pulses is converted into a pulse whose amplitude is proportional to the corresponding intervals. This then is analysed by a multichannel amplitude analyser. A detailed account of the systematic development of the time to

amplitude converters and their use in measuring lifetimes in the nanosecond region is given in an article by Bell[4].

2.2 Recoil and Doppler Shift Method

Excited nuclei produced in typical nuclear reactions or disintegrations recoil with velocities of the order 10^8 - 10^9 cms./sec. The recoil motion can be used to measure the lifetime of the excited state either (a) by a direct measurement of the distance traversed by the nucleus before it radiates, or (b) by observations on the Doppler shift of the emitted γ-rays. The direct distance method has been used to measure lifetimes down to about 10^{-12} seconds where as with the Doppler shift the range is extended to about 10^{-14} seconds.

The Direct distance method:

For a typical radiation mean life of, say, 10^{-11} secs. a recoiling nucleus will travel a distance of about 10^{-2} - 10^{-3} cms. in vacuum before radiating. A measurement of this distance permits the mean life of the state to be estimated provided the initial velocity of recoil be known. In the simplest form of the experiment, a thin layer of the desired target placed in vacuum is bombarded with suitable particles, and the intensity distribution of the radiation emitted from the recoiling nuclei is studied as a function of distance from the target plane in the direction of recoil, the region from which radiation is

observed being defined by very narrow slits. The intensity distribution curve thus obtained is then compared to the theoretical intensity distribution curves drawn for various assumed values of the mean life (τ) of the excited state. The experimental and theoretical curves agree when the correct value of τ has been chosen (Fig. 3). This method has been used by Devons et al.[31] and Thirion et al.[32] to measure half lives in the range 10^{-8} - 10^{-12} seconds of several γ-transitions in the nuclei O^{16}, O^{17} and F^{19}. The technique has been further developed by incorporating coincidence arrangements which have the advantage of selecting a well defined beam of recoil nuclei in a definite direction. Severiens and Hanna[33] have applied this modification to measure the lifetimes of the first excited states of B^{10} and Al^{28} populated in (d,p) reactions. The values observed are $(8.5 \pm 2.0)\times10^{-10}$ and $(3.0 \pm .5) \times 10^{-10}$ seconds respectively.

The Doppler Shift method:

This method basically consists of allowing the recoil nuclei to pass through a stopping film and measuring the Doppler shift of the emitted γ-radiation. The energy of the γ-radiation will be different depending on whether it is emitted before or after the recoil nucleus is stopped in the film. Radiations from nuclei which have been stopped before they radiate show no Doppler effect while those from others do. The observed energy of the emitted γ-radiation will depend, therefore, on the slowing down

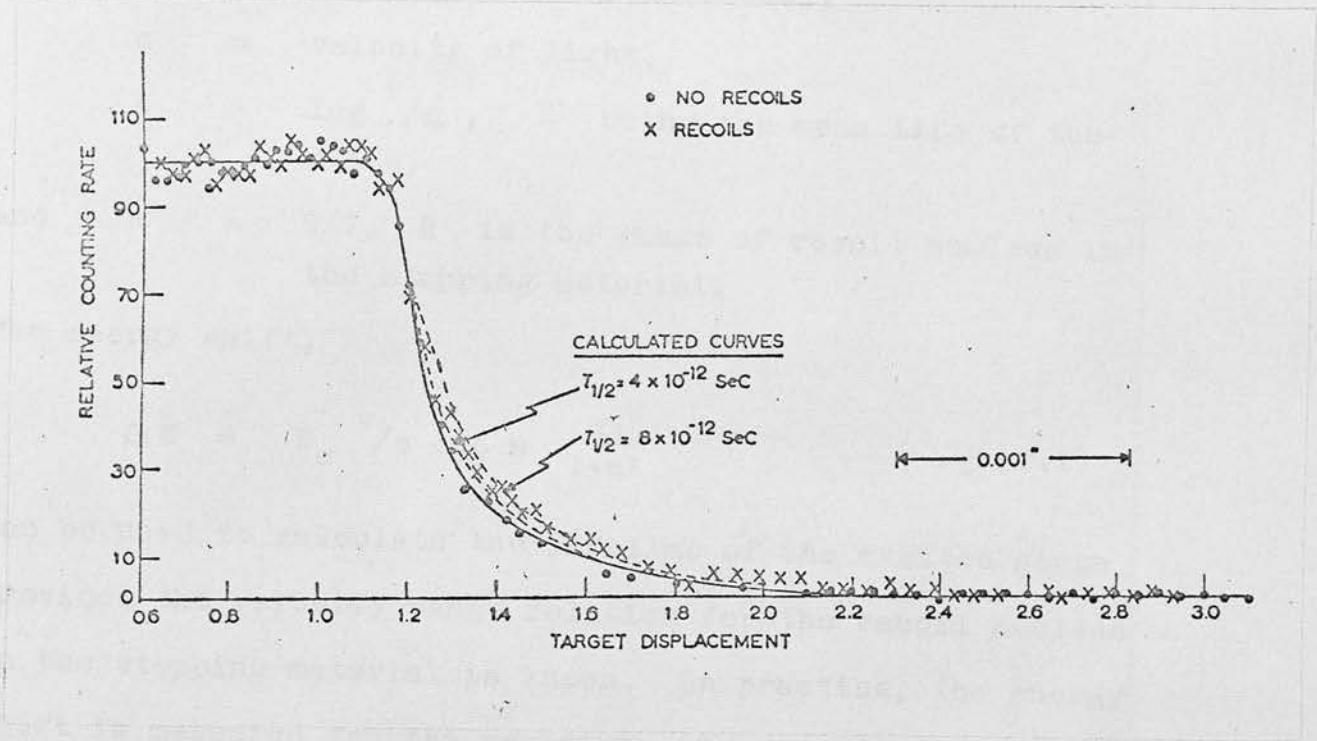

Fig. 3. Lifetime Measurement of E3 Transition in O^{16}.

time of the recoil nuclei in the stopping film. For observations at an angle θ to the direction of recoil, the energy of radiation is given by

$$E = E_o \left[1 + \frac{v}{c} \cos\theta \ \frac{\alpha\lambda}{1+\alpha\lambda}\right] , \qquad (2.1)$$

where E_o = radiation energy for nuclei at rest,

v = initial velocity of recoil,

c = velocity of light,

λ = $\log \tau^2/\tau$, τ being the mean life of the state,

and α = R/V, R is the range of recoil nucleus in the stopping material.

The energy shift,

$$\Delta E = E_o \, v/c \cos\theta \ \frac{\alpha\lambda}{1+\alpha\lambda} \qquad (2.2)$$

can be used to calculate the lifetime of the excited state provided the velocity-range relation for the recoil nucleus in the stopping material is known. In practice, the energy shift is measured for the positions $\theta = 0$ and $\theta = \pi$. The mean energy shift is then given by

$$\Delta E' = 2E_o \, v/c \ \frac{\alpha\lambda}{1+\alpha\lambda} \qquad (2.3)$$

A coincidence arrangement between the bombarding particles and the succeeding γ-rays may be incorporated in order to define a beam of recoil nuclei in a definite direction. Using this method Devons et al.[34] have obtained the limits $10^{-12} \leqslant \tau \leqslant 10^{-11}$ seconds for the mean life of the 6.13 MeV level in O^{16}.

The accuracy of the results obtained by the method described above is very much limited chiefly because the velocity-range relations for the recoiling nuclei in different materials are not well known. In a later work, Devons et al. have shown that if a light material of thickness x be sandwiched between the target and the target backing material, then the Doppler shift is given by

$$\Delta E = E_o v/c \cos\theta \left[1 - \exp(-\lambda x/v) \right]. \qquad (2.4)$$

This permits a lifetime determination independent of α.

Though Doppler shift of γ-rays has been observed as is evident from the above experiments, it is much easier to detect the shift of the corresponding conversion electrons, and for γ-energies in the X-ray region, of photoelectrons ejected from an external converter whose K-edge is fairly close to the γ-energy. Elliot and Bell[35] have measured the Doppler shift of K-photoelectron lines ejected from a uranium radiator by the 479 keV γ-ray of Li^7 produced in the reaction $B^{10}(n, \alpha)Li^7$. The slowing down time of the recoiling Li^7 nuclei was varied by using target backing materials of different density. The observed line widths were compared with the theoretical curves (Eq. (2.3)) computed for various assumed values of τ. As shown in Figures 4(a) and 4(b), the observed widths fit on to the curve which corresponds to the correct mean life of the excited state. The mean life of the 479 keV level obtained by this method was $(0.75 \pm .25) \times 10^{-13}$ seconds.

Burde and Cohen[36] have used the Doppler shift of the

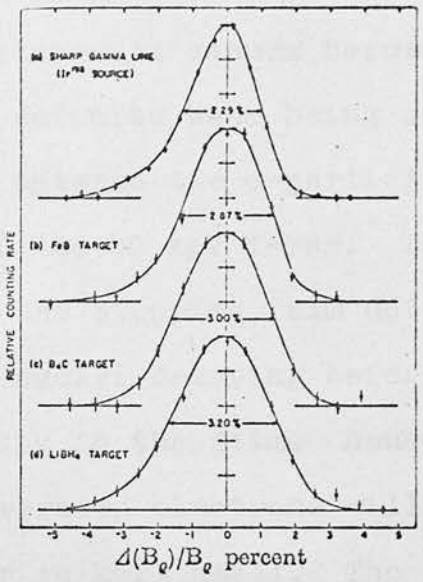

Diagram showing Doppler broadening of the 479 keV gamma ray of Li^7, (*a*) Comparison gamma ray. (*b*) (*c*) (*d*) Li^7 gamma rays from three targets of progressively decreasing density

Fig. 4(a)

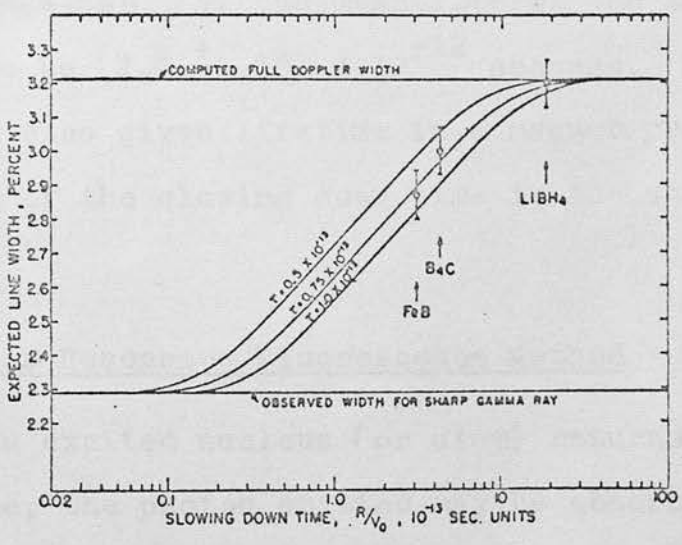

Fig. 4(b).

L-conversion line to estimate the mean life of the 40 keV excited state in Tl^{208} produced in the α-decay of Bi^{212}. The experimental arrangement used by these authors is shown schematically in Fig. 5. The recoiling nuclei from the source travel through a small distance in vacuum before entering into a stopping foil, a definite beam being selected by a coincidence arrangement between the α-particles and the L-conversion electrons of the 40 keV γ-ray. The distance (x) between the source and the stopping film determines the ratio of the number of nuclei decaying before reaching the film to those decaying in the film. Hence, the observed momentum of the conversion electrons will depend on x provided the latter is kept small. The Doppler shift (δ) in this case is given by

$$\delta = \delta_o e^{-x/v\tau} \qquad (2.5)$$

where δ_o is the shift corresponding to infinite separation ($\sim$ 2mm) between the source and the film. By plotting log δ against x/v, the mean life of the 40 keV state was found to be $(1.0 \pm .05) \times 10^{-12}$ seconds. Obviously, this method also gives lifetime in a manner practically independent of the slowing down time in the stopping medium.

2.3 Nuclear Resonance Fluorescence Method

When an excited nucleus (or atom) returns to the ground state, the photon emitted may be absorbed by another identical nucleus (or atom), which in turn is excited to the same state and subsequently emits a photon of the same

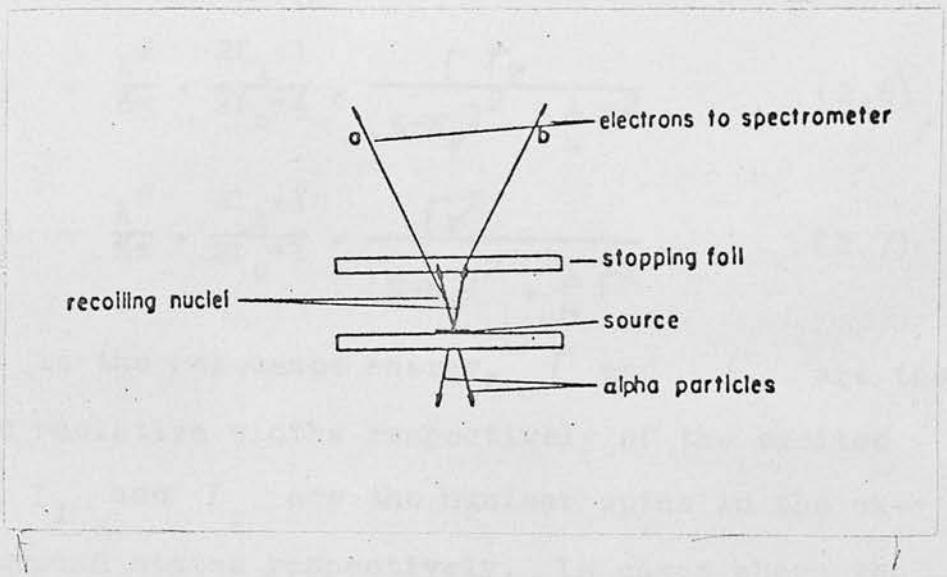

Fig. 5. Schematic diagram showing lifetime measurement of excited states produced in α-decay.

energy. This is the phenomenon of resonance fluorescence or resonance scattering, and, obviously, can be observed only for transitions going to the ground state.

Resonance experiments with γ-rays are usually performed by either measuring the scattered intensity or by determining the attenuation of the beam due to resonance absorption. The cross-section for resonance absorption and scattering by a nucleus of a γ-ray of energy E and wavelength λ is given by

$$\sigma a(E) = \frac{\lambda^2}{8\pi} \cdot \frac{2I_1+1}{2I_o+1} \cdot \frac{\Gamma \Gamma_\gamma}{(E-E_r)^2 + \frac{1}{4}\Gamma^2} \qquad (2.6)$$

and

$$\sigma s(E) = \frac{\lambda^2}{8\pi} \cdot \frac{2I_1+1}{2I_o+1} \cdot \frac{\Gamma_\gamma^2}{(E-E_r)^2 + \frac{1}{4}\Gamma^2} \qquad (2.7)$$

where, E_r is the resonance energy, Γ and Γ_γ are the natural and radiative widths respectively of the excited state, and I_1 and I_o are the nuclear spins in the excited and ground states respectively. In cases where the internal conversion coefficient is very small and γ-transition is the only mode of decay of the excited state, $\Gamma_\gamma = \Gamma$. Thus, an experimental measurement of σ will give the level width and hence the lifetime of the excited state.

An essential requirement for the resonance absorption to occur is that the emission and absorption lines must overlap - a condition which is normally not satisfied in the case of nuclear transitions. It follows from the principle of conservation of energy and momentum that if a nucleus of

mass M emits a photon of energy E, it will recoil with energy $\frac{E^2}{2Mc^2}$; an equal amount of energy is lost when the photon is absorbed by a similar nucleus. Thus the energy available for the excitation of the absorber is reduced by $\frac{E^2}{Mc^2}$ as a result of which the centres of the emission and absorption lines do not coincide. In the typical case for a γ-ray of energy 500 keV in a nucleus with A = 100, the recoil energy loss, E_R is 2.68 eV. In such a situation the emission and absorption lines can overlap only if they are sufficiently broad. But the natural widths of the most common γ-lines, E2 and M1, are too small ($\sim 10^{-3}$ eV) to make this possible, and the lines practically do not overlap in spite of the fact that they are considerably broadened due to the thermal motion of the nuclei (Fig. 6). The scattering cross-section is, therefore, too small to be measured. A high background due to the competing processes, e.g. Compton, Rayleigh and Thomson scattering, make the measurement still more difficult. The thermal motion of the nuclei referred to above which tends to broaden the emission and absorption lines has also an undesirable effect of reducing the maximum scattering cross-section (σ_0) to $\sigma_0 \Gamma_\gamma/\Delta$, where Δ is the Doppler broadening of the line shapes due to thermal motion of the nuclei and is given by

$$\Delta = \frac{E}{c}\left(\frac{2KT}{M}\right)^{\frac{1}{2}} , \qquad (2.8)$$

K is the Boltzman constant and T is the absolute temperature of the source and the absorber. In fact the Doppler

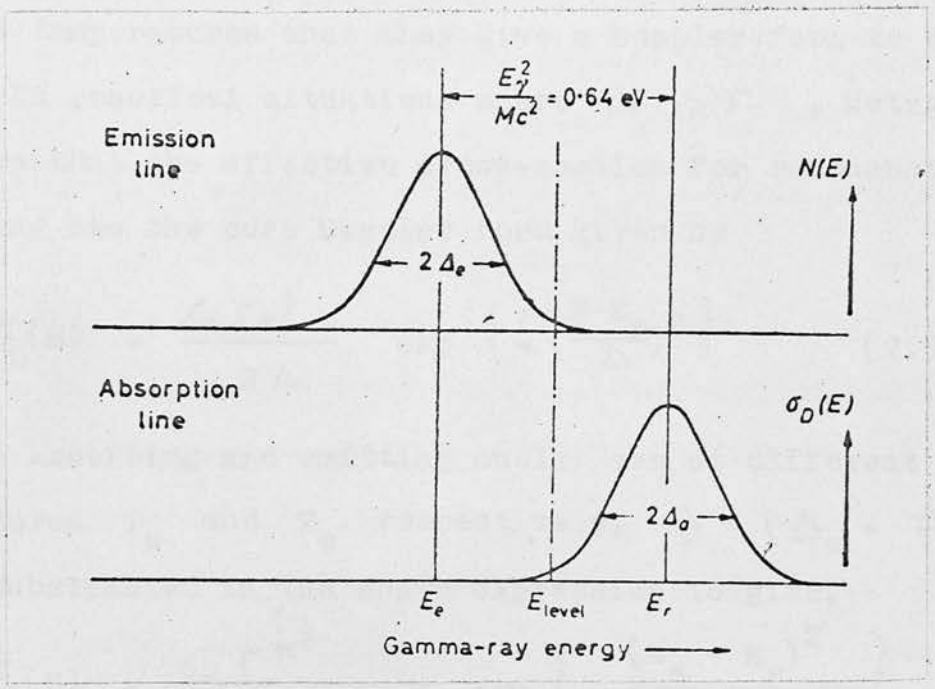

Fig. 6. Showing the Small Overlap of the Emission and absorption lines due to recoil energy loss (Ref. 38).

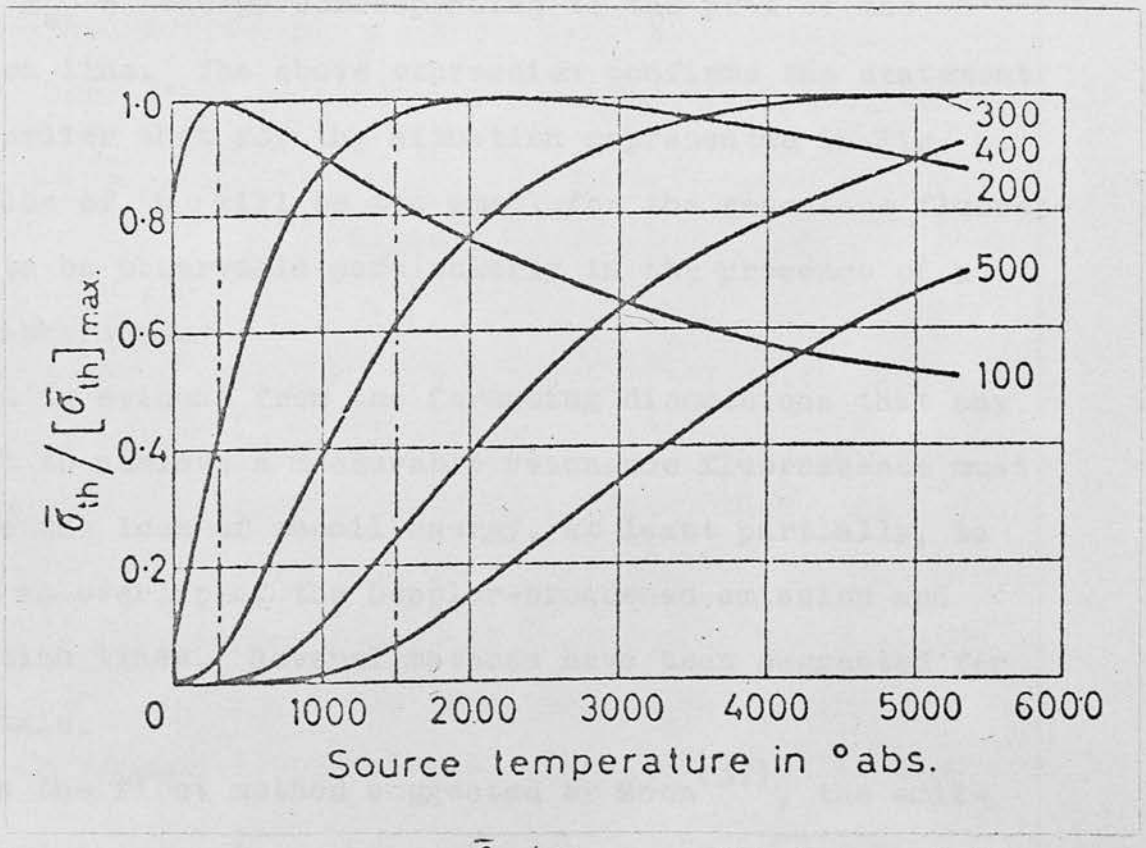

Fig. 7. Variation of $\bar{\sigma}_{Th} / (\bar{\sigma}_{Th})_{max.}$ with temperature (Ref. 38).

widths are so many times larger than the natural widths at ordinary temperatures that they give a Doppler form to these lines. In practical situations where $\Delta >> \Gamma$, Metzger has shown that the effective cross-section for resonance scattering has the pure Doppler form given by

$$\sigma_D(E) = \frac{\sigma_0 \Gamma \pi^{\frac{1}{2}}}{2\Delta} \exp\left\{-\left(\frac{E-E_r}{\Delta}\right)^2\right\} \qquad (2.9)$$

When the absorbing and emitting nuclei are at different temperatures T_a and T_e respectively, $\Delta = (\Delta_a^2 + \Delta_e^2)^{\frac{1}{2}}$ may be substituted in the above expression to give,

$$\sigma_D(E) = \frac{\sigma_0 \Gamma \pi^{\frac{1}{2}}}{2(\Delta_a^2 + \Delta_e^2)^{\frac{1}{2}}} \exp.\left\{-\frac{(E_e - E_r)^2}{\Delta_a^2 + \Delta_e^2}\right\} \qquad (2.10)$$

where E_e = energy corresponding to the peak of the emission line. The above expression confirms the statement made earlier that for the situation represented in Fig. 6, the value of σ will be too small for the resonance fluorescence to be observable particularly in the presence of a high background.

It is evident from the foregoing discussions that any attempt to achieve a measurable resonance fluorescence must restore the loss of recoil energy, at least partially, to ensure an overlap of the Doppler-broadened emission and absorption lines. Several methods have been suggested for doing this.

In the first method suggested by Moon[37], the emitting nuclei are put on the periphery of a fast rotating

centrifuge so as to give them an additional velocity towards the absorber. γ-rays emitted along a particular tangent are only allowed to strike the absorber. The tangential velocity of the emitting nuclei shifts the emission line as a whole towards the absorption line by an amount depending on the velocity of the centrifuge. If u be the relative velocity of the emitter with respect to the absorber, then the Doppler effect will increase the energy E of the emitted γ-ray, by $\frac{uE}{c}$. Hence resonance will be completely restored when $u = u_m = E/Mc$. For a γ-ray energy of about 500 keV in a heavy nucleus, the velocity needed to satisfy this condition is $\sim 10^4$ cms./sec. which is not difficult to achieve. Moon has applied this method to determine the lifetime of the 411 keV transition in Hg^{198} using liquid Hg as scatterer. The appropriate expression for scattering cross-section which takes into account the effect of thermal velocities of the nuclei is

$$\sigma = \frac{\lambda^2}{8\pi} \Gamma \left(\frac{2I_1+1}{2I_o+1}\right)\left(\frac{Mc^2}{4\pi KTE^2}\right)^{\frac{1}{2}} \exp\left[-\frac{M(u-u_m)^2}{4KT}\right] \qquad (2.11)$$

The value of Γ obtained was 2.1×10^{-5} eV which corresponds to a half life of $(2.2 \pm .5) \times 10^{-11}$ sec. In the experimental arrangement employed by Moon, large scattering angles ($\sim 115^o$) were used to filter out the Compton photons which were further suppressed by surrounding the detector with suitable shields. The problem of reducing the background in resonance fluorescence experiments has been discussed in great detail in a review article by Metzger[38].

Another method for obtaining resonance fluorescence is the thermal method, developed by Malmfors in which the emitter or the absorber or both are heated in order to make the Doppler broadening, and hence the overlapping larger. For practical reasons, it is the source which is usually heated while the absorber is kept at room temperature. A theoretical plot of $\frac{\bar{\sigma}_{Th}}{(\bar{\sigma}_{Th})_{max}}$ ($\bar{\sigma}_{Th}$ = cross section appropriate to this process) against the source temperature for different γ-energies (see Fig. 7) shows that the thermal method is most suitable for γ-energies between 150 keV and 450 keV. Malmfors[38] used this method to measure the lifetime of the 411 keV transition in Hg^{198} and obtained a value of 8×10^{-6} eV for the level width which is much smaller than Moon's value. The discrepancy was attributed to the small scattering angle used by Malmfors in which case the assumption of isotropic distribution of the scattered radiation is not justified. A correction on this account gives $\Gamma = 1.3 \times 10^{-5}$ eV or 3.5×10^{-11} sec. for the half life. Metzger and Todd repeated the measurement with an improved technique and obtained the lifetime of $(2.2 \pm .2) \times 10^{-11}$ sec. which is in good agreement with the value observed by the centrifuge method.

The third method of obtaining resonance fluorescence utilises the recoil motion from the radiation (β or γ transition) preceding the formation of the excited state to impart Doppler broadening to the emission line. Since molecular collision times in solid sources are of the order

of 10^{-13} seconds, this method cannot be applied for lifetimes $\gtrsim 10^{-13}$ secs. with such a source. For a solid source the method is only applicable to an E1 transition provided it decays to the ground state. One of the rare examples of such a transition is the 961 keV E1 γ-ray in Sm^{152} following electron capture decay of Eu^{152}. Grodzin[39] using a solid Eu^{152} source was able to observe a measurable resonance effect entirely due to preceding neutrino recoil. The range of this method is, however, much increased if a liquid or gaseous source is used because the molecular collision times in such media are of the order 10^{-6} sec., and hence the recoil momentum from the preceding radiation can be preserved for a longer time. Grodzin found that with a liquid Eu^{152} source the scattering cross-section for the 961 keV E1 γ-ray in Sm^{152} was about 4 times larger than that with a solid source. For liquid and gaseous sources, when resonance is obtained mainly by the recoil motion of the preceding radiation, the average scattering cross-section for a thin scatterer is given by

$$\sigma_{av} = \frac{N(E_R)}{N_T} \cdot \frac{\lambda^2}{8\pi} \cdot \frac{2I_1+1}{2I_o+1} \cdot 2\pi \frac{\Gamma_r^2}{\Gamma} \qquad (2.12)$$

where $N(E_R)$ is the number of γ-rays per unit energy at $E = E_R$, and N_T is the total number of quanta in the incident beam. Since the energy resolution of the detector does not permit a direct measurement of $N(E_R)$, the ratio $\frac{N(E_R)}{N_T}$ is usually obtained from the theoretical estimate of the microspectrum. Palathingal[40] has used this idea to measure the mean life of 564 keV excited state in Tl^{122}

using a gaseous source of Sb^{122} in the form of antimony trihydride. The value obtained was $(1.05 \pm .16) \times 10^{-11}$ sec. In cases where $N(E_R)$ is not known, a self-absorption experiment can be done for the measurement of level width. The method consists of studying the absorption by putting variable amounts of resonant absorber between the source and the scatterer. If $R(x)$ and $R(o)$ be the resonance effect observed with and without the intervening absorbers, respectively, then as Metzger has shown,

$$\frac{R(o) - R(x)}{R(o)} = \frac{\Gamma\gamma}{2\Delta} \sigma_o \sqrt{\frac{\pi}{2}}\, nX \quad , \qquad (2.13)$$

where n is the number of resonant nuclei per cm^3 of the absorber. Obviously this method can be used only if the resonance effect without absorber is large. Using this method Beard[41] has measured the mean life of the 1.27 MeV state of Sn^{116} to be $(.33 \pm .07) \times 10^{-12}$ sec.

2.4 The Mössbauer Effect.

In 1958, while measuring the lifetime of the 129 keV level in Ir^{191}, Mossbauer discovered a new method of obtaining nuclear resonance fluorescence which obviated the need of compensation for the recoil energy loss. This was accomplished by simply having the emitting and absorbing nuclei bound in crystals at low temperature. The resonance observed in such cases can be accounted for by considering the crystal and the nuclei embedded in it as constituting one single quantum mechanical system in which the nuclei

interact with the crystal lattice only by exchange of vibrational quanta or phonons. Mössbauer showed that when a nuclear transition occurs in such a system the recoil momentum is taken up by the crystal as a whole, and no energy is available for the excitation of the lattice or translational motion of the nucleus. The nuclear transition energy, on the other hand, is shared, for all practical purposes, between the lattice and the γ-rays which in general, may lead to excitation of the former and corresponding depletion in the energy of the latter. There is, however, a definite probability, although small, for the occurrence of a zero phonon transition in which case there is no energy transfer to or from the lattice vibrations. When this is so, the γ-rays are emitted and absorbed without any energy loss, and at the same time they have the natural width Γ. The fraction of transitions in which γ-rays are emitted without loss of recoil energy is given by the Debye-Waller factor, $f = e^{-2\omega}$, where

$$w = \frac{2R}{K\Theta}\left[\frac{1}{4} + \left(\frac{T}{\Theta}\right)^2 \int_0^{\Theta/T} \frac{x\,dx}{e^x - 1}\right] \qquad (2.14)$$

where R = Molecular gas constant, Θ = Debye temperature
K = Boltzman constant and T = temperature of the lattice (^oK).

The fraction is larger for low photon energies, low temperatures and lattices with high vibrational frequencies. Selection of a suitable combination of source and crystal is, therefore, of utmost importance in Mössbauer experiments.

The basic set up used by Mössbauer for the lifetime

measurement of the 129 keV level in Ir^{191} is shown in Fig. 8. The source used was Os^{191}, which by β-decay goes to Ir^{191}, and the absorber was natural crystalline iridium (38.5% Ir^{191}), both being kept at 88°K. The source was mounted on a turn table whose speed of rotation could be varied, and the transmission of the 129 keV γ-rays through the absorber was studied as a function of the source velocity (v) (see Fig. 9). Fig. 10 shows the variation of scattering cross-section with the temperature of the source. Using $\Delta E = {}^{v}/_{c} E$, the abscissa in Fig. 8 can be converted to energy units. For $v = 0$, the emission and absorption lines overlap completely, which results in a maximum in the resonance absorption and hence a mimimum in the transmitted intensity. The fact that rather small relative velocities are required for the observation of the resonance curve indicatesthat the lines exhibit their natural width only. For a thin absorber, the intensity distribution of the resonant radiation exhibits Lorentzian shape with width 2Γ, showing that the experiment consists in the movement of an emission line of width Γ over an absorption line of the same width. The lifetime obtained for the 129 keV level of Ir^{191} was 1.0×10^{-10} sec.

The example considered above is the simplest and ideal one. In actual experiments, there are several factors, e.g. solid state effects, extranuclear fields etc., which tend to broaden and change the shape of lines, and thereby limit the range of transitions whose lifetime can be determined by

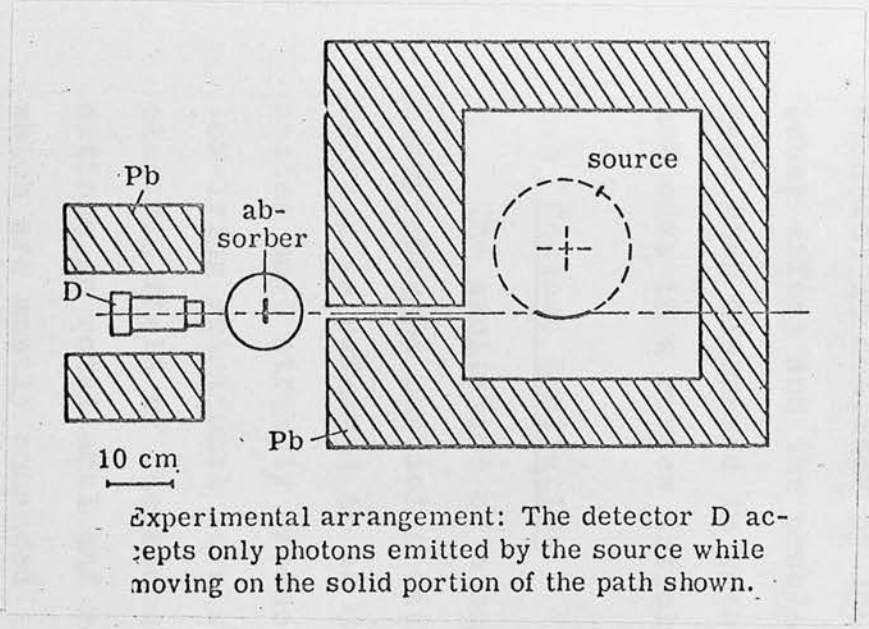

Experimental arrangement: The detector D accepts only photons emitted by the source while moving on the solid portion of the path shown.

Fig. 8. (Taken from Ref. 42).

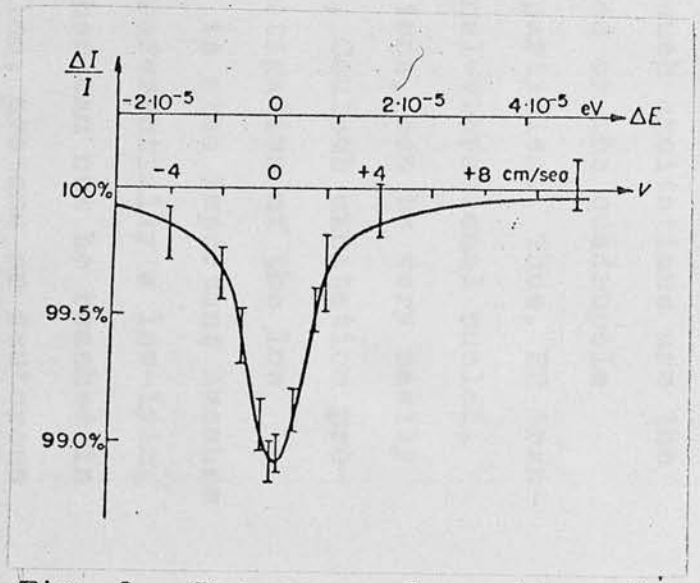

Fig. 9. Resonance absorption of 129 keV I_r^{191} γ-rays (Ref. 43).

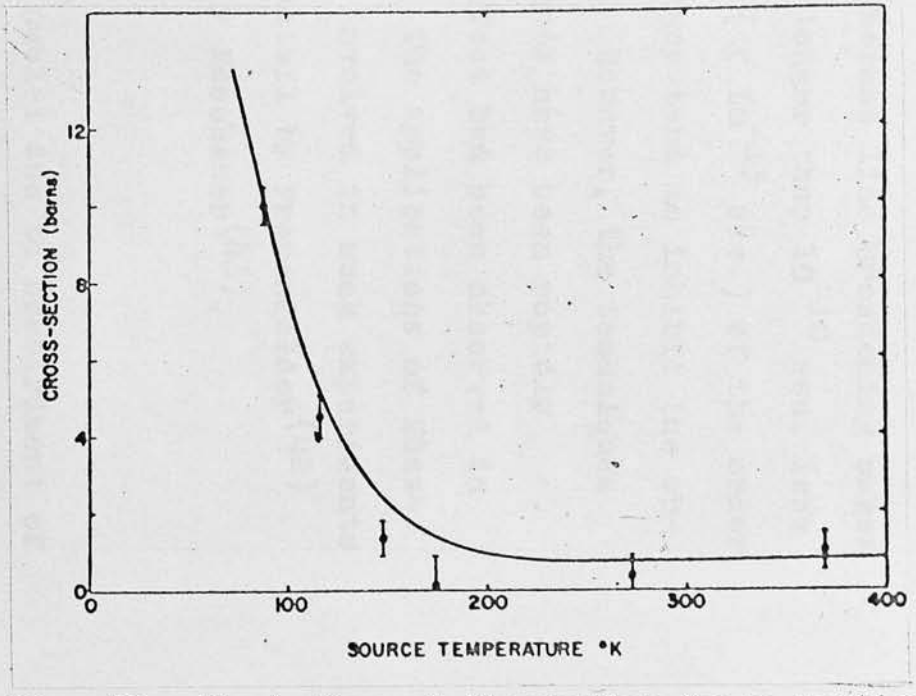

Fig. 10. Variation of Absorption Cross-section with temperature (Ref. 42.).

Mossbauer experiments. Thus whereas line broadening makes the measurements of lifetimes longer than 10^{-10} sec. less reliable, too short lifetimes ($\leq 10^{-13}$ sec.) of the order of the inverse of Debye frequency tend to inhibit the observation of Mössbauer effect. However, the techniques used in the Mössbauer experiments have been rapidly developed and the Mössbauer effect had been observed in at least 15 nuclides by 1962. The applications of Mössbauer effect and the problems involved in such experiments have been discussed in great detail by Frauenfelder[42] and also in a review article by Mossbauer[43].

2.5 Coulomb Excitation

The excitation of atomic nuclei due to bombardment of heavy charged particles with energy below the Coulomb barrier is referred to as Coulomb excitation. The nuclear states most strongly produced in such excitations are the low-lying rotational levels induced by the quadrupole electric field of the bombarding particles. Thus, E2 transitions in rotational and rotational-vibrational nuclei, which are mostly enhanced transitions, can be very easily observed by this method. In fact, Coulomb excitation provides a very useful tool for investigation of the low energy states in such nuclei. It is also important because it provides a means of exciting preferentially a low-lying state which for some reason or other can not be reached in radioactive decay. With α-particles, protons or deuterons of energy in the range 3-10 MeV, it is usually the first and second rotational levels that are excited. Higher

states can be excited in a step-wise process by multiple Coulomb excitation. Such processes, however, require heavy ions, e.g. O^{16}, Ar^{40} etc., with high energy (100-200 MeV). Stephens et al.[44], using a heavy ion accelerator, have succeeded in exciting rotational states up to 12+ in U^{238} and 10+ in Th^{232}.

Though lifetime measurements are the main objective of the Coulomb excitation experiments, they also yield other information, e.g. spin, parity, etc. concerning the excited states independently of any nuclear model. Several review articles[45-49] deal with these problems in great detail. What follows below is only intended to illustrate the use of Coulomb excitation in lifetime measurements.

For nuclear excitations produced by low energy particles (3-10 MeV), the process can be treated by first order perturbation theory, the interaction between the electric field of the nucleus and that of the incident particle causing the transition of the nucleus from the ground state to the excited state. In such a treatment, the differential and total cross-sections for Coulomb excitation corresponding to the most important case of quadrupole electric transition are given by

$$\frac{d\sigma_{E2}}{d\Omega} = \left(\frac{Z_1 e}{\hbar v}\right)^2 a^{-2} B(E2; I_i \rightarrow I_f) \frac{df_{E2}}{d\Omega}(\theta, \xi, \eta) \qquad (2.15)$$

and

$$\sigma_{E2} = \left(\frac{Z_1 e}{\hbar v}\right)^2 a^{-2} B(E2; I_i \rightarrow I_f) f_{E2}(\xi, \eta) \qquad (2.16)$$

where,

$$\xi = \frac{Z_1 Z_2 me^2}{\hbar v} \cdot \frac{\Delta E}{2E} , \quad \eta = \frac{Z_1 Z_2 me^2}{\hbar v}$$

$a \simeq \frac{Z_1 Z_2 e^2}{\hbar v}$, v, Z_1 and m are the velocity, atomic number and reduced mass of the incident particle, Z_2 = atomic number of the target nucleus, E = energy of the incident particle, ΔE = energy of the excited state, θ = angle through which ions are inelastically scattered, and $B(E2; I_i \rightarrow I_f)$ = reduced transition probability for excitation. The variation of the functions $\frac{df_{E2}}{d\Omega}$ and f_{E2} with the parameters involved are given in a series of tables and graphs by Alder et al.[45]. A measurement of the total or differential cross-section allows the determination of $B(E2; I_i \rightarrow I_f)$ which is related to the reduced transition probability, $B(E2; I_f \rightarrow I_i)$ for de-excitation by

$$B(E2; I_f \rightarrow I_i) = \frac{2I_i+1}{2I_f+1} B(E2; I_i \rightarrow I_f)$$

The transition probability or lifetime ($\tau = \frac{1}{T}$) of the state is given by expression (1.18),

$$T(E\ell; I_i \rightarrow I_f) = \frac{8\pi(\ell+1)}{\ell[(2\ell+1)!!]^2} \frac{1}{\hbar} K^{2\ell+1} B(E\ell; I_f \rightarrow I_i)$$

From expressions (2.15), (2.16) and (1.18), it is obvious that the lifetime of a state formed in Coulomb excitation can be determined by measuring the cross-section for the corresponding excitation.

The most commonly used method for measuring the Coulomb excitation cross-section is by measuring the total yield of de-excitation γ-rays for thick targets using a

scintillation spectrometer. The total yield may be determined directly by using 2π geometry (Heydenburg and Temmer[50]) or by observing the γ-yield (Stelson and McGowan[51]) at fairly large angles ($\sim 235^{\circ}$) with respect to the beam in which case only a small known correction for the angular distribution of γ-rays has to be applied. Knowing the variation of photopeak efficiency of the NaI crystal with the γ-energy, the experimentally observed yield is converted into absolute yield. The determination of cross-section from the total yield is complicated since the cross-section changes as the incident particle slows down in its passage through the target material. The cross-section, therefore, has to be integrated over the track length of the slowing down particle. A method of doing this has been suggested by Huus and Mottelson[50]. The γ-ray yield thus obtained is then corrected for the background arising partly from the external sources, and partly from the characteristic X-rays, bremsstrahlung etc. The value of B(E2) extrapolated from the yields has to be multiplied by the factor $(1 + \alpha)$ to take account of the downward transitions occurring by internal conversion. A knowledge of total internal conversion coefficient, α, is thus needed to determine the correct value of B(E2). All these factors limit the accuracy of the B(E2) values to about $\pm$ 8%. A detailed discussion of the background corrections and the optimum conditions for the experiment has been given by Alder et al.[45].

The observation of the internal conversion electrons of the de-excitation γ-rays provide an alternative method of measuring the cross-section for Coulomb excitation,

particularly when the γ-rays are heavily obscured by background radiations. The method is more easily applicable to low energy transitions in heavy elements where an appreciable fraction of excitations decay by internal conversion. The internal conversion electrons are analysed in a β-ray magnetic spectrometer, using a thin target to minimise the self-absorption of electrons. The main background in the conversion spectrum arises from the tightly bound electrons which may be ejected with sufficiently high energies. However, by considering the cross-section for production of such electrons, an optimum condition can be found to give a maximum signal to noise ratio. The cross-section for Coulomb excitation is given by the total electron yield

$$Y(n) = C(p) \frac{P(n)}{p} D \quad , \qquad (2.17)$$

where $P(n)$ is the area of the conversion line at momentum p, $C(p)$ is the counting loss factor, and D is the transmission factor of the spectrometer. The latter two quantities are determined empirically as described by Rester et al.[52]. The accuracy in the value of B(E2), thus extracted, is limited to about $\pm$ 10% which is mainly due to the uncertainties in the knowledge of the transmission factor of the spectrometer. Using the conversion electron method Rester et al. have obtained the value of $B(E2; 0 \rightarrow 2)$ for a number of even A isotopes of Os, Th and U. The values obtained by these authors are about 25% larger than the corresponding values from the γ-ray yield method by Stelson and McGowan.

The most straightforward method of measuring the Coulomb excitation cross-section is by observations of the inelastically scattered projectiles. The scattered particles, consisting of the inelastic group resulting from Coulomb excitation and the elastic group due to Rutherford scattering (the separation between the two being of the order of 100 keV) are analysed by means of a high resolution magnetic spectrometer and recorded photographically. Since the background due to accidentally scattered particles is very high at forward angles ($\theta = 0$), measurements are usually made at an angle of 145° which is found to give the best ratio between the inelastically scattered group and the background. A graphical plot of the number of tracks per mm. as a function of distance along the photographic plate enables one to obtain the ratio of the intensities of inelastically and elastically scattered group of particles. This is also the ratio of the differential cross-sections for the two processes. Since the elastic scattering can be calculated from Rutherford's law, the differential cross-section for inelastic scattering can be determined, from which the value of B(E2) can be obtained. In general, the B(E2) values obtained by this method have an accuracy of about 3-5%. The main advantage of this method is that the yield is independent of the decay mode of the excited state and hence a knowledge of total internal conversion coefficient is not required for the determination of B(E2). Elbek et al.[53] and also several other groups of workers have used this method for lifetime measurements of the first 2+ excited state in rare earth nuclei.

2.6 Inelastic Electron Scattering

Inelastic scattering of high energy ($\sim$ 100 MeV) electrons, like Coulomb excitation, may result in the excitation of nuclear levels, and hence can be used to determine the lifetime and multipolarity of the excited states[54]. Though still in a state of infancy, it provides one of the few means of studying nuclear resonance transitions with excitation greater than a few MeV accompanied by a fairly large change in angular momentum ($\gtrsim 3\hbar$).

The differential cross-section for nuclear excitation by inelastic electron scattering calculated on the Born approximation theory is given by

$$\frac{d\sigma_{E\ell}}{d\Omega} = \left(\frac{e}{\hbar c}\right)^2 \frac{4\pi(\ell+1)}{\ell[(2\ell+1)!!]^2} \frac{q^{2\ell}}{K_i^2} \left\{ \frac{\ell}{\ell+1} B(C\ell,q)\, V_L(\theta) + B(E\ell,q) V_T(\theta) \right\} \qquad (2.18)$$

for electric 2^ℓ pole excitations, and

$$\frac{d\sigma_{M\ell}}{d\Omega} = \left(\frac{e}{\hbar c}\right) \frac{4\pi(\ell+1)}{\ell[(2\ell+1)!!]^2} \frac{q^{2\ell}}{K_i^2} B(M\ell,q)\, V_T(\theta) \qquad (2.19)$$

for magnetic 2^ℓ pole excitations, where q and K represent the momentum and energy transfer in the process of collision, $B(E\ell,q)$ and $B(M\ell,q)$ are the reduced nuclear transition probabilities for excitation, $B(C\ell,q)$ is the reduced transition probability resulting from the instantaneous Coulomb interaction, V_L and V_T are the functions representing the contributions of the longitudinal (Coulomb) and transverse interactions, respectively, and θ

is the angle of scattering. Since the instantaneous Coulomb operator involves a $\ell = 0$ term, it is obvious that unlike Coulomb excitation, E0 transitions can also be excited in the inelastic electron scattering. In the limit as $q \rightarrow 0$ and excitation energy $(E_x) \ll$ initial electron energy, it turns out that the transition operators are identical with the radiative electric and magnetic multipole moments $\left[B(C\ell,0) = B(E\ell)\right]$ and the inelastic cross-section at $\theta = 0$ for electric and magnetic 2^ℓ pole transitions are related to the radiative lifetime τ of the excited state by

$$\tau_{E\ell}^{-1} = \frac{\ell+1}{2\ell} \frac{e^2}{a^2\hbar^2K^2} (E_x)^5 \frac{2I_i+1}{2I_f+1} \cdot \frac{d\sigma_{c\ell}}{d\Omega} (\theta \rightarrow 0) \qquad (2.20)$$

$$\tau_{M\ell}^{-1} = \frac{e^2}{a^2\hbar^2K^2} (E_x)^5 \frac{2I_i+1}{2I_f+1} \frac{d\sigma_{M\ell}}{d\Omega} (\theta \rightarrow 0) \qquad (2.21)$$

A measurement of the inelastic cross-section at forward angles (near $\theta \sim 0$) will thus give the radiative lifetime of the excited state directly through the above relations.

In practice, however, because of a large background due to radiative tail and bremsstrahlung at angles close to zero, the cross-section measurements are made at finite angles ($\sim 40^\circ$). In this case, the transition operators are not identical with the radiative multipole moments, and expressions (2.20) and (2.21) can no longer be used for lifetime determination. For measurements at finite angles,

the differential cross-section for inelastic scattering exciting an electric multipole transition of order ℓ may be written as

$$\frac{d\sigma}{d\Omega} = \left(\frac{d\sigma}{d\Omega}\right)_{Mott} \left[F^2_{L\ell}(q) + (\tfrac{1}{2} + \tan^2 \theta/2) F^2_{T\ell}(q)\right] \qquad (2.22)$$

where $F_{L\ell}$ and $F_{T\ell}$ can be regarded as 'form factors' due to longitudinal and transverse parts of the interaction respectively, $\left(\frac{d\sigma}{d\Omega}\right)_{Mott}$ is the differential cross-section for elastic scattering by a point charge $(Z_2 e)$. A graphical plot of $\left(\frac{d\sigma}{d\Omega}\right)_{obs} / \left(\frac{d\sigma}{d\Omega}\right)_{Mott}$ as a function of $\tan^2 \theta/2$ enables the form factors to be determined for the experimental value of q which in turn gives the value of $B(c\ell, q)$ through the relation

$$\left| F^2_{L\ell}(q) \right|^2 = \frac{4\pi q^{2\ell}}{Z_2^2 \left[(2\ell+1)!!\right]^2} B(c\ell, q) \qquad (2.23)$$

Measurement of lifetime of the excited state, however, requires the value of B corresponding to $q \to 0$. If $\rho_\ell(r)$ be the ℓ-th order radial transition density, then the form factor can be expressed as

$$\left| F_{E\ell}(q) \right|^2 = \left[4\pi \int_0^\infty \rho_\ell(r)\, j_\ell(kr)\, r^2\, dr\right]^2 \qquad (2.24)$$

This relation may be used to calculate F assuming some model for the transition charge distribution. The model that gives agreement with the measured value of F may then be extrapolated to very small values of q to give $B(E\ell)$ from which the lifetime of the excited state can be determined. This method of lifetime measurement is thus

model dependent. The different models used in various measurements have been discussed by Bishop[55]. Using the model suggested by Helm[56], Crannel et al. have measured the lifetime of some E1, E2, E3 and M1 transitions in Li^6, C^{12}, Mg^{24}, Ni^{60}, Ni^{58} and Pb^{208}. The values obtained are in good agreement with the values previously obtained by other methods.

A new method of extrapolation using the experimentally determined elastic and inelastic form factors has been recently employed by Crannel and Griffy[57] to obtain the radiative widths of the first three excited states in C^{12}. The method does not use any model for the transition charge distribution and applies only to the scattering angles (40° - 90° used in this experiment) where the longitudinal part of the interaction is predominant enough to permit the transverse part to be neglected in the expression (2.22). If $F_\ell(q)$ and $F(q)$ denote the inelastic and elastic form factors respectively, the latter being given by

$$\left(\frac{d\sigma}{d\Omega}\right)_{elastic} = \left(\frac{d\sigma}{d\Omega}\right)_{Mott} Z^2 \left|F(q)\right|^2 , \qquad (2.25)$$

then defining

$$R_\ell = F_\ell / q^{\ell-2} \left[1 - F(q)\right] \text{ for } \ell \neq 0 \qquad (2.26)$$

gives in the limit $q \rightarrow 0$,

$$R_\ell = A_\ell (1 - B_\ell q^2) \qquad (2.27)$$

A plot of R_ℓ against q^2 gives a straight line only for small values of q and a correct choice of ℓ. The intercept at $q^2 = 0$ yields A_ℓ which can be used in the

relation,

$$\Gamma_{E\ell} = \frac{\ell+1}{1\ell} \cdot \frac{2I_i+1}{2I_f+1} \alpha \langle r^2 \rangle^2 E_x^{2\ell+1} A_\ell^2 \qquad (2.28)$$

to obtain the radiative width of the excited state.

2.7 Monoenergetic Positron Emission

Monoenergetic positron emission is a mode of nuclear decay which occurs in competition with internal pair formation. When a K-capture nucleus decays with the formation of an electron-positron pair, the electron may be captured by a vacancy in the K-shell, and only the positron emitted. The positrons produced in such a process are monoenergetic having energy,

$$E_m^K = E_\gamma - 2m_o c^2 + E_K \qquad (2.29)$$

where E_γ is the nuclear excitation energy, E_K is the binding energy of a K-electron, and $2m_o c^2$ is the rest energy of the pair. The ratio of the probability for the emission of monoenergetic K-positrons to that for the emission of γ-rays is given by

$$N_{e^+}^K / N_\gamma = \alpha_{e^+}^K P_K \left(\frac{\tau_K}{\tau + \tau_K}\right) \qquad (2.30)$$

where $\alpha_{e^+}^K$ is the coefficient for the monoenergetic K-positron formation which, for a permanent vacancy in the K-shell, is defined as the probability for emission of a monoenergetic positron per emitted γ-ray, P_K is the probability for the excitation of the initial nuclear level by K-capture, τ_K is the mean life of the atomic K-vacancy and τ is the mean life of the nuclear level to be

measured. $\tau_K/\tau+\tau_K$ is obviously the probability of nuclear transition taking place before the K-vacancy disappears.

The values of $a^K_{e^+}$ for El, Ml and E2 transitions have been calculated by Sliv[58] and more recently for El transitions by Lombard and Rys[59]. The results of the two calculations do not agree. According to the latter,

$$a^K_{e^+} \approx (2\alpha Z)^3 \times 2.4 \times 10^{-3} \times \frac{1}{k}\sqrt{\frac{k-2}{k}} \qquad (2.31)$$

where α is the fine structure constant and k is the nuclear excitation energy in units of $m_o c^2$. Since P_K and τ_K can be calculated, an experimental measurement of the monoenergetic positron intensity relative to the γ-photons yields by expression (2.30) the lifetime (τ) of the excited state. In practice, when the internal K-conversion coefficient (α_K) is known, instead of N_γ, the number of K-conversion electrons ($N^K_{e^-}$) from the same transition is measured. N_γ is then given by, $N_\gamma = N^K_{e^-}/\alpha_K$. As $a^K_{e^+}$ is largest for El transitions and so is $\tau_K/\tau+\tau_K$, it is clear that these transitions are the most suitable to be investigated by observations on the monoenergetic positrons. But, because $E_K/(E_\gamma - 2m_o c^2)$ has to be a few times larger than the instrumental energy resolution, the method can be applied only to medium and high Z nuclei.

Using high resolution spectrometers, several groups of workers[21,22,60-63] have observed K-positrons associated with some El transitions in the K-capture decay isotopes of Eu^{152}, Bi^{205} and Bi^{206}. Applying the method outlined above,

Brunner et al.[21] have obtained for the lifetime of the 1720 keV E1 transition in Bi^{206} a retardation of 50 compared with the value predicted by single particle estimates. Wu et al.[22] have reported a retardation of 600 for the same transition. The reason for this discrepancy is not obvious. It may, however, be mentioned that the method of monoenergetic positron emission relies on the calculations of $\alpha^K_{e^+}$, and, as already pointed out, the calculations of this quantity by Sliv, and Lombard and Rys, differ considerably. Besides, the high background due to the β^+ continuum tends to obscure the faint monoenergetic positron peak and make its intensity estimation extremely difficult and uncertain.

2.8 The Limitation of the Methods

From the discussions of the preceding sections it is obvious that the coincidence method is the most universal method for measuring lifetimes of the nuclear excited states in the range 10^{-6} - 10^{-11} seconds. The other methods have only limited applicability and may be regarded as complementary to this method. The recoil and Doppler shift methods are capable of measuring lifetimes down to 10^{-13} seconds. The nuclear resonance methods are applicable only to those states which decay directly to the ground state. Excitation by charged particles provides a means of investigating nuclear levels in non-radioactive isotopes, but as mentioned earlier, Coulomb excitation has been mostly used with the low-lying E2 states in a limited class

of nuclei, though inelastic electron scattering has the potentialities of exciting higher states as well. All these methods work in more or less the same range and permit the measurement of lifetime up to 10^{-13} sec. Although these methods satisfactorily cope with most of the E2 and M1 transitions available in the radioactive decays, they are not capable of measuring lifetimes of E1 transitions which are of the order of 10^{-16} secs. The only E1 γ-ray whose mean life has been measured by the resonance method is the 961 keV transition in Sm^{152}. The inelastic electron scattering method can have very limited application to such transitions because very few of these go to the ground state directly. Thus, observations on the monoenergetic positron emission is the only means available for the study of E1 transitions with energy greater than 1.02 MeV. A new method for measuring lifetime of the E1 transitions by observations on X-ray satellites will be described in Chapter IV of this thesis. The method is applicable to transitions with energy $\sim$ 1 MeV in medium to high Z-nuclei.

CHAPTER III

AUGER EFFECT AND X-RAY SATELLITES

3.1 Some Definitions:-

When a vacancy has been created in an inner electron shell of an atom, the atom may reorganise itself in one of two ways. The vacancy may be filled within $10^{-14} - 10^{-17}$ sec. by an electron transition from some outer shell, thus shifting the vacancy to an outer shell. The difference of the binding energies of the two shells concerned in the transition may then be emitted as a characteristic X-radiation. Alternatively, this energy may be transferred to an electron in an outer shell which is ejected from the atom. This latter process of radiationless reorganisation is known as the Auger effect and the ejected electrons are known as Auger electrons. In principle, both of these processes are well understood. The radiative transition can be adequately explained in terms of the multipole theory which predicts that by far the most important mode is the electric dipole. The non-radiative, or Auger, transitions may be regarded as a direct interaction of the two electrons with the ejection of one of them, or as one in which a quantum of X-radiation arising from an inner shell transition is internally converted in an outer shell so that an electron is ejected from that shell.

The most important measure of the Auger effect is the fluorescence yield of an atomic shell, which for the i-th shell is defined as the probability that a vacancy in that shell is filled by a radiative transition, i,e.

$$\omega_i = \frac{\text{Number of i-X rays emitted}}{\text{Number of primary i-vacancies}} \qquad (3.1)$$

The Auger yield of the same shell is defined as the probability that an electron is emitted when the vacancy is filled from a higher shell, i.e.

$$a_i = \frac{\text{Number of i-Auger electrons emitted}}{\text{Number of primary i-vacancies}} \qquad (3.2)$$

Obviously for the K-shell,

$$a_i = (1 - \omega_i) \qquad (3.3)$$

The situation is more complicated in the case of higher atomic shells. In the L shell, for instance, there are three subshells L_1, L_2, L_3 and though one may define fluorescence yields ω_1, ω_2 and ω_3 for the three subshells but in practice what is measured is the average fluorescence yield $\bar{\omega}_L$. Since ω_1, ω_2, ω_3 are not in general equal, $\bar{\omega}_L$ depends on the ratio of the primary vacancies in these subshells and hence on the way in which the L shell is ionised.

Another complicating factor which occurs in certain regions of the periodic table is the radiationless transitions of a particular kind known as Cöster-Kronig transition in which a vacancy created in a subshell is moved to another subshell of the same major shell before it is filled by an electron from an outer shell. The corresponding Coster-Kronig yield (f_{xy}) is defined as the probability that a vacancy is filled with an electron making a non-radiative transition from an outer subshell in the

same major shell. For the L shell, Cöster-Kronig transitions could be represented as L_1L_2X, L_1L_3X and so on, where X refers to outer shells M, N, etc.

From the definition of fluorescence yield, Auger yield and the Cöster-Kronig yield for the L shell, the following relationships between them are obvious:

$$\begin{aligned} \omega_3 + a_3 &= 1 \\ \omega_2 + a_2 + f_{23} &= 1 \end{aligned} \qquad (3.4)$$

and

$$\omega_1 + a_1 + f_{12} + f_{13} = 1$$

Another quantity of interest is the width of an energy level which is the sum of the partial widths of all processes by which the level can decay (i.e. processes by which a vacancy can be filled). This is defined as

$$\Gamma_T(i) = \Gamma_i^R + \Gamma_i^A + \sum_{K>i} \Gamma_{iK} \qquad (3.5)$$

where $\Gamma_T(i)$ = total width,

Γ_i^R = radiative width,

Γ_i^A = Auger width,

and Γ_{iK} = Cöster-Kronig width, all referring to the i-th level.

From the definitions of ω_i, a_i and f_{iK}, we have

$$\begin{aligned} \omega_i &= \frac{\Gamma_i^R}{\Gamma_T(i)} \\ a_i &= \frac{\Gamma_i^A}{\Gamma_T(i)} \end{aligned} \qquad (3.6)$$

and $$f_{iK} = \frac{\Gamma_{iK}}{\Gamma_T(i)}$$

3.2 Classification, Energy and Intensity of Auger Electrons

A detailed treatment of the Auger process has been given by Burhop[64] (1952). More recent developments have been summarised in review articles by Bergström and Nordling[65], and M.A. Listengarten[66].

3.2.1 Classification of Auger electrons:-

An atom with a single vacancy, or hole, is left, as a result of the Auger effect, with two holes. A series of Auger electrons (e.g. K-series, L-series, etc.) is labelled by the shell in which the initial vacancy occurs, whereas a group (e.g. the K-LL, K-LM, K-MN groups of the K-series) is labelled by the shells containing the two holes resulting from the Auger effect. Obviously, each group will consist of several Auger electron lines of different energy.

The notation used for the different Auger lines of any group depends on the method one uses to characterise the states of the doubly ionised atom, and this varies according to the coupling scheme chosen for the different regions of atomic number. In general, the L-S, the intermediate and the J-J couplings are applicable for small Z ($Z < 20$), intermediate Z ($20 \lesssim Z \lesssim 40$) and high Z ($Z > 40$) respectively. The number of lines in the K-LL group, for instance, according to these coupling schemes will be as follows:-

(a) L-S Coupling:- Six lines: $^1S\ (s^0p^6)$, ^1P, $^3P\ (s^1p^5)$

and ^1S, ^1D, ^3P ($s^2 p^4$).

(b) Intermediate Coupling:- nine lines: K-L_1L_1 (^1S_o), K-L_1L_2 ($^1P_1$), K-L_1L_2 (^3P_o), K-L_1L_3 ($^3P_1$), K-L_1L_3 ($^3P_2$), K-L_2L_2 (^1S_o), K-L_2L_3 ($^1D_2$), K-L_3L_3 (^3P_o) and K-L_3L_3 ($^3P_2$).

(c) J-J Coupling:- Six lines: K-LL_1 ($s^o_{1/2}\ p^2_{1/2}\ p^4_{3/2}$), K-$L_1L_2$ ($s^1_{1/2}\ p^1_{1/2}\ p^4_{3/2}$), K-$L_1L_3$ ($s^1_{1/2}\ p^2_{1/2}\ p^3_{3/2}$), K-$L_2L_2$ ($s^2_{1/2}\ p^o_{1/2}\ p^4_{3/2}$), K-$L_2L_3$ ($s^2_{1/2}\ p^1_{1/2}\ p^3_{3/2}$) and K-$L_3L_3$ ($s^2_{1/2}\ p^2_{1/2}\ p^2_{3/2}$).

Out of the nine lines in the intermediate coupling, three, namely K-L_1L_2 (^3P_o), K-L_1L_3 ($^3P_2$) and K-L_3L_3 (^3P_o) are very weak, and invariably they fuse into six lines as in LS or JJ coupling. In fact, in most cases J-J coupling provides the most useful analysis of the Auger spectrum.

3.2.2 The energy of Auger electrons:-

The energy calculations of Auger electrons have been carried out by several investigators, but there is no satisfactory agreement between the theoretical and experimental values. However, the semi-empirical calculations of Asaad and Burhop[67] which have been made in the non-relativistic approximations but include factors to take account of the relativistic and screening effects, give the relative positions of the lines very well. More accurate calculations of the energies of the KLL group lines

giving better agreement with the experimental data, (probably within .05%), for $30 \leq Z \leq 85$, have been reported by Hornfeldt[65].

For heavier elements, the Auger electron energies are given by

$$E(V_o - X_i Y_j) = E(V_o) - E(X_i) - E\left[Y_j(X_i)\right] \qquad (3.7)$$

where V_o denotes the shell with the initial vacancy, X_i and Y_j are the shells in which vacancies are produced by Auger transition, $E(V_o)$, $E(X_i)$ refer to the binding energies of the electrons in these shells, and $E\left[Y_j(X_i)\right]$ refers to the binding energy of Y_j electron when an electron is missing in the X_i shell. The quantity $E\left[Y_j(X_i)\right]$ is slightly higher than $E(Y_j)$, the binding energy of the Y_j electron in the neutral atom. A convenient empirical method of finding $E\left[Y_j(X_i)\right]$ has been suggested by Bergström and Hill[65]. According to these authors, when an atom is ionised in the X_i shell, $E(Y_j)$ increases as though it were due to some increase ΔZ in the atomic number Z of the atom. Hence,

$$E_Z(V_o - X_i Y_j) = E_Z(V_o) - E_Z(X_i) - E_{Z+\Delta Z}(Y_j) \qquad (3.8)$$

The value of ΔZ lies between 0.7 and 1.3, and in most cases can be taken to be unity.

Measurements of L Auger spectra require very high instrumental resolution and a very highly developed source preparation technique. Because of these experimental difficulties, the data available on L Auger electrons is very scanty and unreliable.

3.2.3 The intensity of Auger electrons:-

In order to calculate the Auger transition probability in the non-relativistic limit, it is assumed that the two electrons initially move in the field due to the nucleus and the average field of the remaining electrons. The Coulomb interaction energy $\frac{e^2}{r_1-r_2}$ between the two electrons then acts as a perturbation which causes a transition in which the Auger electron is ejected into continuum while the other electron goes to fill the inner vacancy.

If $\psi_i(r_1)$ and $\phi_i(r_2)$ be the Schroedinger wave functions describing the two electrons in the initial state, and $\psi_f(r_1)$ and $\phi_f(r_2)$ be their Schrödinger wave functions in the final state, then the Auger transition probability will be given by

$$W_a = \frac{2\pi}{\hbar}\left| \int\int \psi_f^*(r_1)\phi_f^*(r_2)\ \frac{e^2}{r_1-r_2}\ \psi_i(r_1)\phi_i(r_2)\,dr_1\,dr_2 \right|^2 dt \times \rho \qquad (3.9)$$

where ρ is the energy density of the final states. For a large transition rate, the wave functions of the two electrons in the initial and final states should overlap considerably, and r_1-r_2, the difference in the electron coordinates should be small. The latter condition is naturally satisfied if r_1 and r_2 refer to the neighbouring shells.

Since the electrons are indistinguishable, the Pauli's exclusion principle is taken into account by replacing the product of the wavefunctions in the above expression by

antisymmetric combination of the single electron wave-functions.

Thus, $\psi_i(r_1)\phi_i(r_2)$ becomes $\frac{1}{\sqrt{2}}\left\{\psi_i(r_1)\phi_i(r_2) - \psi_i(r_2)\phi_i(r_1)\right\}$

and similarly for $\psi_f(r_1)\phi_f(r_2)$ (3.10)

$$\therefore \quad W_a = \frac{2\pi}{\hbar}\left|\iint\left[\phi_f^*(r_2)\psi_f^*(r_1)\frac{e^2}{r_1-r_2}\psi_i(r_1)\phi_i(r_2) - \phi_f(r_1)\psi_f(r_2)\frac{e^2}{r_1-r_2}\psi_i(r_2)\phi_i(r_1)dr_1dr_2\right]\right|^2 dt \qquad (3.11)$$

The Auger transition probability has been calculated by many workers in the non-relativistic approximation. The group in which the line intensities have been most thoroughly studied is the K-LL group. A comparison of the results of these calculations with the experimental values shows that the non-relativistic theory does not give good agreement even for low values of Z. Relativistic calculations for Z = 80 in the J-J coupling limit have been carried out by Asaad[68] where screening has been taken into account through the use of the non-relativistic self-consistent Hartree field. A similar calculation for Z = 65, 81 and 92 has been done by Listengarten[69,70] taking the effect of screening into account by means of the Thomas-Fermi-Dirac statistical model of the atom. It is found that the relativistic calculations for the K-LL spectrum of heavy elements give much improved agreement with the experimental results.

Very few measurements have been made for the K-LX

and K-XY group of Auger electrons, where X and Y refer to shells other than K or L. Some graphs are, however, available showing the variation of the ratios, $\frac{K\text{-}LX}{K\text{-}LL}$ and $\frac{K\text{-}XY}{K\text{-}LL}$ with Z. Experiments on L-Auger lines are still rare due to the experimental difficulties pointed out in section 3.2.2. Recently some measurements have been reported by Tolburen and Albridge[71], and Haynes et al.[72] using a $\pi\sqrt{2}$ iron-free spectrometer with a resolution of 0.18%.

3.3 Fluorescence Yields

A knowledge of K- and L-shell fluorescence yields is of interest not only for a detailed interpretation of the X-ray spectra but also because they are required for several nuclear measurements, e.g. determination of (a) the relative probability of electron capture and positron emission for the same energy states, (b) K to L capture ratio and hence Q-values in the capture process, and (c) K-conversion coefficients. Quite a lot of work - both theoretical and experimental - has been done in this field during the last two decades. Burhop[64], Broyles et al.[73], Laberigue-Frolov and Randvanyi[74], Wapstra, Njigh and Van Lie Shout[75], Listengarten[66] and Fink et al.[76] have given comprehensive reviews of fluorescence yield measurements.

Non-relativistic calculations of the K-shell fluorescence yield of the atom has been done by Burhop[77], and Pincherle[78] using hydrogen like wavefunctions with an effective nuclear charge given by Slater's rules. Their

calculations show that the transition rate for X-radiation is proportional to Z^4 while the Auger Effect depends very weakly on Z.

Hence,

$$\omega_K = \frac{\Gamma_X}{\Gamma_K} = \frac{Z^4}{a+bZ^4} \qquad (3.12)$$

where a and b are constants.

Various authors have suggested modifications to this formula, the following semi-empirical relation being due to Burhop,

$$\left(\frac{\omega_K}{1-\omega_K}\right)^{1/4} = -A + BZ + CZ^3 \qquad (3.13)$$

The terms on the right represent the screening effect, the Z^4 dependence of the dipole transitions and the relativistic effects respectively. The constants A, B and C can be evaluated from experiment by a least squares fit. Curves of the above equation, plotted using the available experimental data, have been published in several of the papers referred to above. Though there is reasonable agreement between the experimental and the predicted values for the region $23 \leq Z \leq 57$, the differences are considerable for small and high Z. The measurements with small Z are, of course, subject to large errors due to experimental difficulties.

Relativistic calculations for ω_K have been done by Massey and Burhop[79], Asaad[68] and Listengarten[69]. Their results indicate that, for large Z, the introduction of relativistic wavefunctions tends to lower the value of ω_K by a significant amount.

Most of the K-shell fluorescence yield measurements have been done by electron intensity measurements using precision beta-spectrometers. Some measurements[76] have been made using scintillation and proportional counters with variable solid angle. Hagendoorn and Wapstra[80] have used a coincidence method to determine ω_K for nuclei decaying by electron capture, using a proportional counter in coincidence with a scintillation spectrometer. Recently, Taylor and Merritt[76] have reported some precise measurements of ω_K for some nuclei using electron capture sources. The last method which is based on absolute measurements of disintegration rates and K X-ray emission rates, gives very reliable results. Listengarten has evaluated the K-fluorescence yield for some elements from a knowledge of the total and radiation widths of their K-levels.

A comparison of all these experimental results with the various theoretical predictions shows that the agreement with experimental data is good at high Z for Listengarten's relativistic calculations and also that the latest more accurate experimental methods give results which agree best with the theoretical curve of equation (3.13).

The problem of L-shell fluorescence yield measurement is complicated. Often, therefore, only the mean fluorescence yield $\bar{\omega}_L$ has been measured. Measurements of this quantity are of limited significance, firstly because the fluorescence yields for the three L-subshells are different and secondly, because the initial distribution

of vacancies in the subshells depend on the mode of excitation. Obviously the results of such measurements apply only to the particular element and to the particular mode of ionisation. In cases where Cöster-Kronig transitions take place, the situation can be pictured in two possible ways. The view taken by Listengarten[66] is to regard the measured $\bar{\omega}_L$ as a linear combination of the subshell yields (ω_1, ω_2, ω_3) with an altered primary vacancy distribution due to the Cöster-Kronig effect. Wapstra, Njigh and Van Lie Shout[75], on the other hand, take $\bar{\omega}_L$ as a linear combination of the primary vacancy distribution and redefine the subshell fluorescence yields to take account of the Cöster-Kronig transitions. Both views are, however, equivalent, though the latter is more convenient from the experimental point of view.

A number of measurements of the mean L shell fluorescence yields, using various techniques, have been made by several investigators. An exhaustive review has been given by Fink et al.[76]. The measured values along with some of the available calculated values of $\bar{\omega}_L$ are shown in Fig. 11, reproduced from the reference[66]. Very few authors have measured the separate L subshell yields. Ross, Cochran, Hughes and Feather[81] have discussed the method of finding the L-subshell yields in great detail. Rao and Craseman[82], and Salguero et al.[83] have carried out some isolated measurements of ω_2. In general, the results do not agree well with one another, and are limited in precision.

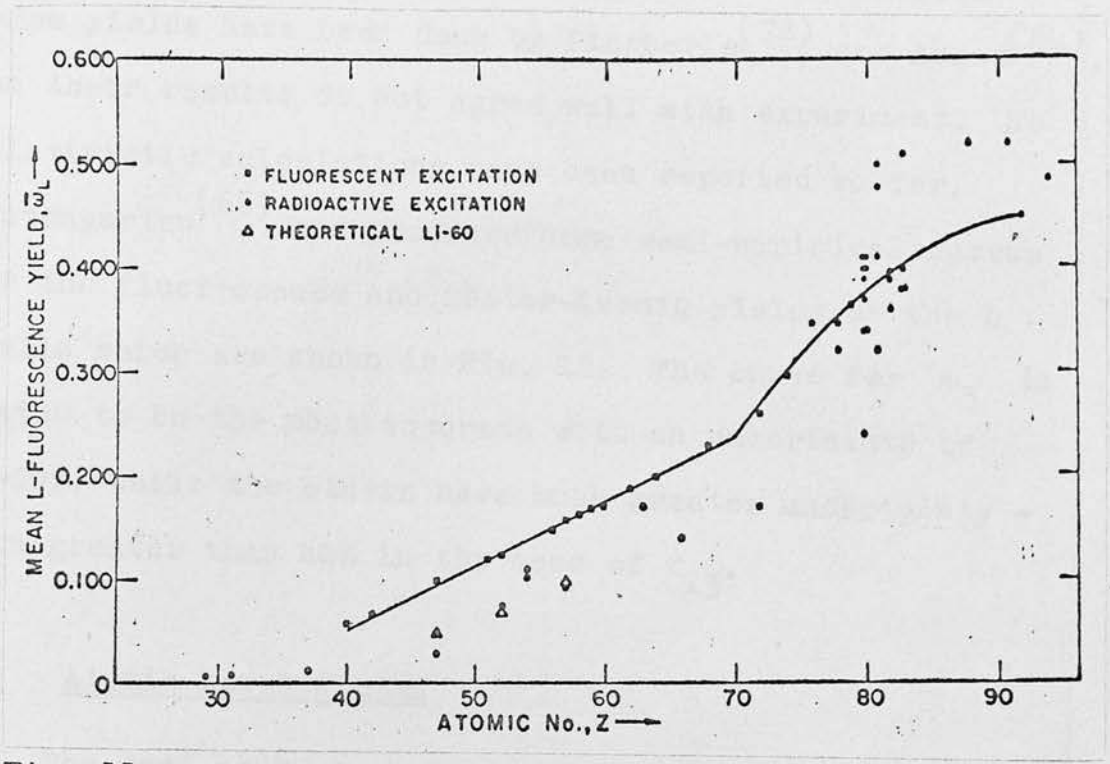

Fig. 11. Mean L-shell Fluorescence Yields (Ref. 76).

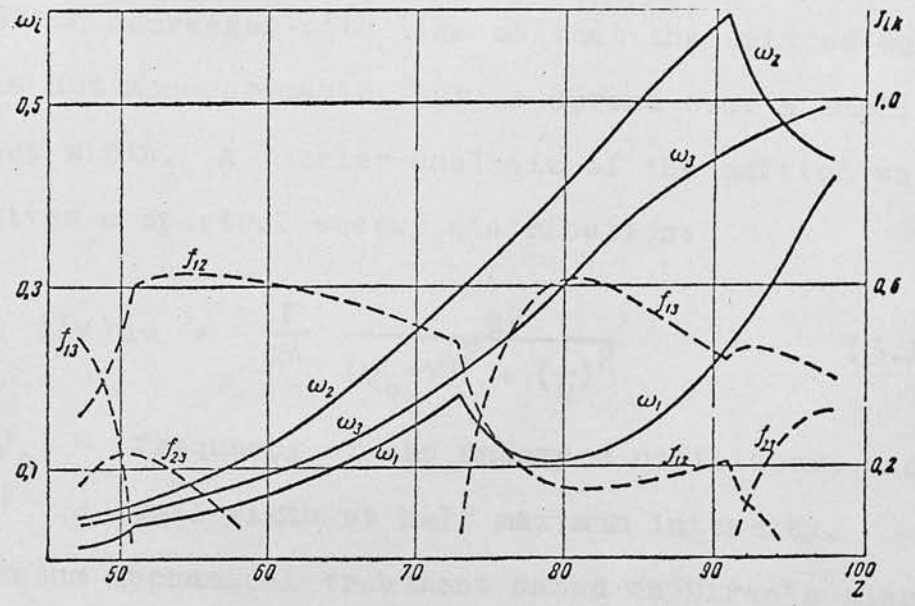

Fluorescence yields ω_i (solid curves) and Coster-Kronig yields f_{ik} (dashed curves) for the L subshells ($i, k = 1, 2, 3$).

Fig. 12. (Taken from Ref. 66).

Theoretical calculations of mean L-shell fluorescence yields have been done by Pincherle[78] and Asaad[84], but their results do not agree well with experiment. No relativistic calculations have been reported so far. Listengarten[66] has produced some semi-empirical curves for the fluorescence and Cösster-Kronig yields of the L shells which are shown in Fig. 12. The curve for ω_3 is stated to be the most accurate with an uncertainty of 10-20%, while the others have much greater uncertainty - even greater than 40% in the case of f_{13}.

3.4 Atomic Level Widths

The concept of unsharp atomic energy levels giving rise to spectral lines of finite widths belongs to the classical theory as well as to the quantum mechanical theory. In the classical theory an emitting atom is regarded as a damped harmonic oscillator whose amplitude of oscillation decreases with time so that the emitted wave train is not monochromatic, but is spread over a small frequency width. A Fourier analysis of the emitted wave train gives a spectral energy distribution:

$$I(\nu)d\nu = \frac{\Gamma}{2\pi} \frac{d\nu}{(\nu_o-\nu)^2 + (\frac{\Gamma}{2})^2} , \qquad (3.14)$$

where ν_o = frequency of the undamped oscillator, and
Γ = full width at half maximum intensity.

In a quantum mechanical treatment based on Dirac's theory of radiation, Weisskopf and Wigner (1930) have shown that

the intensity distribution in a spectral line given out in a transition from an initial state "i" to a final state "f", is given by a relation similar to (3.14):-

$$I(\nu)d\nu = \frac{\Gamma}{2\pi} \frac{d\nu}{(\nu_{if} - \nu)^2 + (\frac{\Gamma}{2})^2} \qquad (3.15)$$

where $\nu_{if} = \frac{E_i - E_f}{h}$, and Γ = full width at half maximum of the radiated line, and it is the sum of the widths Γ_i and Γ_f of the initial and final levels,

$$\text{i.e.} \quad \Gamma = \Gamma_i + \Gamma_f \qquad (3.16)$$

According to this interpretation, the width of a spectral line is the sum of the widths of the initial and final levels involved in the emission.

In quantum mechanics, the concept of the finite width of an atomic level comes as a manifestation of the uncertainty principle, according to which a measurement of the energy of a system that is carried out in a time Δt must be uncertain by an amount ΔE, so that

$$\Delta E . \Delta t \sim \hbar .$$

If τ_i is the mean life of the level "i", the above relation is equivalent to

$$\Gamma_i \tau_i = \hbar , \qquad (3.17)$$

where Γ_i = energy width of the level.

This relation is often used to find out the mean life of a level whose width is known experimentally. Since, τ_i is the reciprocal of the total transition probability (p_i) per unit

time of the state, equation (3.17) can also be written as

$$\Gamma_i = \hbar\, p_i \quad . \qquad (3.18)$$

As the radiative processes alone do not account for the observed width of the lines, the total transition probability p_i in equation (3.18) has to be taken as the sum of the transition probabilities for various processes, namely radiative, Auger and Cöster-Kronig transitions. This gives

$$\Gamma_T(i) = \Gamma_i^R + \Gamma_i^A + \sum \Gamma_{iK} \qquad (3.5)$$

which is the definition of the total width of a level given in section (3.1).

A direct method of measuring the width of an atomic level is due to Richtmyer, Barnes and Ramberg[85]. Applying the Weisskopf-Wigner spectral distribution to the case of an absorption process in which an electron is ejected into a region of unoccupied levels in which the distribution in energy is uniform and continuous, these authors have shown that the relationship between the absorption coefficient $\mu(\nu)$ and frequency (ν) of the absorbed radiation is given by

$$\mu(\nu) = C\left\{\tfrac{1}{2} - \frac{1}{\pi} \arctan\left(\frac{\nu_{E_oA} - \nu}{\Gamma/2}\right)\right\} \qquad (3.19)$$

where, ν_{E_oA} is the frequency at the centre of the absorption band,

C is the asymptotic value of $\mu(\nu)$ for high frequencies,

and Γ is the desired level width.

Fig. 13 is a theoretical plot of the above equation.

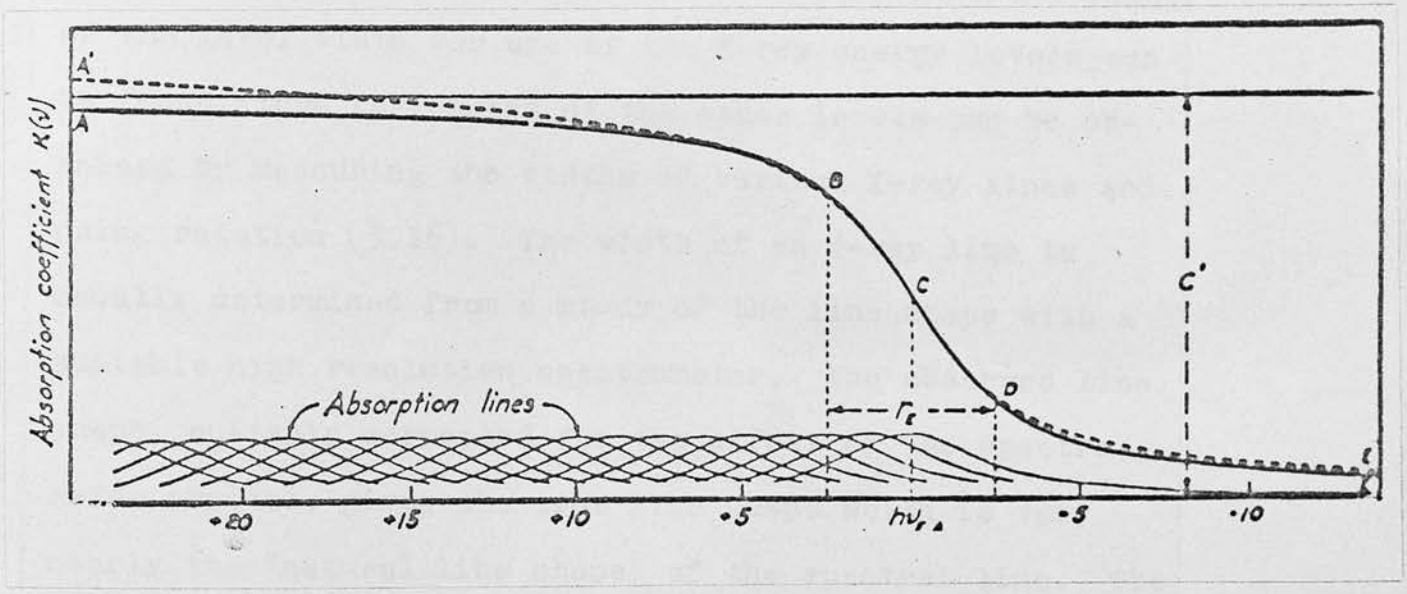

Fig. 13. Plot of Eq. 3.19 (Ref. 85).

The horizontal separation of the two points B and D, where the curve reaches $\frac{1}{4}$ and $\frac{3}{4}$, respectively, of C is defined as the width of the absorption edge.

Though simple in principle, the determination of level width from the shape of an absorption curve is very difficult and unreliable because the shape of the curve is often distorted in the neighbourhood of the edge. Neverthtless, an approximate value of the level width can be obtained by the method outlined above. If a reasonably accurate value of the level width for one of the X-ray energy levels can be found, then the widths of the other levels can be obtained by measuring the widths of various X-ray lines and using relation (3.16). The width of an X-ray line is usually determined from a study of the line shape with a suitable high resolution spectrometer. The observed line shape, suitably corrected for the effect of the spectrometer crystal, gives the true line shape which is very nearly the "natural line shape" of the spectral line. The full width at half maximum of the true line shape gives the width of the line in question.

The widths of X-ray lines and levels in different elements have been mostly studied[85-93] using a double crystal spectrometer. Some of the significant regularities observed by Richtmyer et al.[85] from a study of the level width in W(74) and Au(79) may be summarized as follows:-
(a) In any given series of levels, (e.g. L, M,..., etc.) the width decreases as ℓ increases,
(b) states having the same value of n and ℓ have nearly the same width, and (c) except for the L_I level,

the widths of levels for which $\ell = 0$ increases as n increases.

Some workers [94-95] have determined the widths of the L-series lines in the region Z = 40 to Z = 79, using the photographic method developed by de Langen. This method is claimed to be advantageous particularly for elements only obtainable as compounds.

More recently some measurements of atomic level widths made from an analysis of the conversion electron lines have been reported. Lindström[96] (1951), while studying the β-spectrum of ThB with a semi-circular β-spectrometer, observed that (a) the K-conversion lines in the spectrum were broader than the L_I-conversion lines, and (b) the broadening was the same (~ 80 eV) for all the observed K-conversion lines in the spectrum. Slatis[96], who investigated the problem using a 180° magnetic spectrometer, also arrived at similar conclusions. According to a note in a report by Slatis and Lindstrom[96], K. Siegbahn has suggested that the difference in the width of the conversion lines is due to the difference in the natural width of the levels concerned. Working on Siegbahn's suggestion, Mladjenovic[97] investigated the internal conversion lines of RaB in a double focussing spectrometer and measured the difference in widths of the K- and L-conversion lines. The discrepancy between his value (~ 80-100 eV) and the X-ray value (~ 50 eV) is more likely to be due to the experimental reasons than to the effects accompanying

internal conversion. Latyshev et al.[97] have carried out a very detailed investigation of the K-conversion lines of ThB, and, from a number of independent measurements using different instrumental resolution, obtained a value of 67 ± 5 eV for the natural width of the K-conversion line. This value agrees well with the value 61-63 eV for the width of Bi K-level obtained by extrapolating the K-level width for Z = 79 according to Z^4 law. The authors also conclude that the inherent width of the conversion lines is primarily determined by the widths of the atomic levels and is virtually independent of the effects accompanying internal conversion. Dijkstra and Vries[98] using an iron free double focussing β-spectrometer have found the difference between the K and L atomic level widths to be 49 ± 5 eV for Bi ($K-L_I$) and 54 ± 4 eV for Hg($K - L_{III}$), which are in fair agreement with X-ray data. Geiger et al.[99] have studied the conversion electron lines in Sm^{151} with the Chalk River $\pi\sqrt{2}$ β-spectrometer and from a detailed analysis of the shapes of the conversion lines measured the natural widths of K, M_I M_{II} and M_{III} levels.

Though the internal conversion measurements of level widths are few in number, the results (with the exception of Mladjenovic's) are reasonably consistent, and in fair agreement with the best X-ray values.

The agreement between the experimental and theoretical values for level widths has been discussed by Listengarten[66-70] and Callan[100]. The observed widths seem to be well accounted for by considering the radiative and Auger

processes provided relativistic effects are taken into account for the high Z elements.

3.5 X-ray Satellites

X-ray satellites are those relatively weak lines often observed close to and on the high frequency side of the chief X-ray diagram lines, and because these lines do not fit into the ordinary scheme of X-ray energy levels, they are also referred to as "non-diagram" lines. Siegbahn and Stenstrom (1916) were first to discover the two K-series satellites called $K\alpha_3$ and $K\alpha_4$ while investigating the X-ray spectrum of the elements Na(11) - Zn(30). Since then, intense experimental and theoretical work has been done in this field and many more satellites in the K-series have been observed. That the L-series diagram lines are also accompanied by satellites was first reported by Cöster in 1922. Richtmyer and others, who subsequently investigated the L-series lines in the elements Cu(29) - U(92), found that the satellites were much more numerous in this series than in the K-series. M-series satellites were observed and studied in the elements Yb(70) - U(92) by Hirsh and others. In a review article[101], Hirsh has given a comprehensive summary of the work done on X-ray satellites up to 1942. Further work has been reported by Edamato[102], Deslattes[103] and others. The relevant data on the measurements of all the K- and L-series satellites for the elements in which they have been observed has been compiled by Cauchois and Hulubei[104]. Detailed

references and sources of the data are given by these authors.

A brief summary of the general characteristics of the K- and L-series satellites followed by an attempt to understand them in the light of the currently accepted theories is presented below.

3.5.1 General features of the satellite lines:-

(a) For the K-series satellites, as indeed for the satellites of all other series, the satellite structure changes from one element to another due to the diminishing intensity and subsequent disappearance of some or all of the line components at higher atomic numbers. Thus, the $K\alpha_{3},\alpha_{4}$ satellite was observed by Parratt (1936) only in the narrow atomic number range S(16) - V(23), $K\alpha_{5},\alpha_{6}$ in the range Mg(12) - Cl(17), and so on. Fig. 14 shows how the intensity of the $K\alpha_{3},\alpha_{4}$ group of satellites relative to the parent line $K\alpha_{1}$ decreases as the atomic number increases.

Of the L-series satellites, those that have been widely studied on account of their large intensity at certain atomic number ranges are the satellites of the parent $L\alpha$, $L\beta_{1}$ and $L\beta_{2}$ lines. The quantitative data on satellite intensities by various workers all show that while the $L\alpha$ and $L\beta_{2}$ satellites have a maximum intensity at Rh(45) and Ag(47) respectively, their intensities decrease very rapidly for higher atomic numbers and they become very faint at Sb(51) and I(53) respectively. Similarly the $L\beta_{1}$ satellites have been observed only in the range Zn(30) - Zr(40) with a maximum at Sr(38) above which the

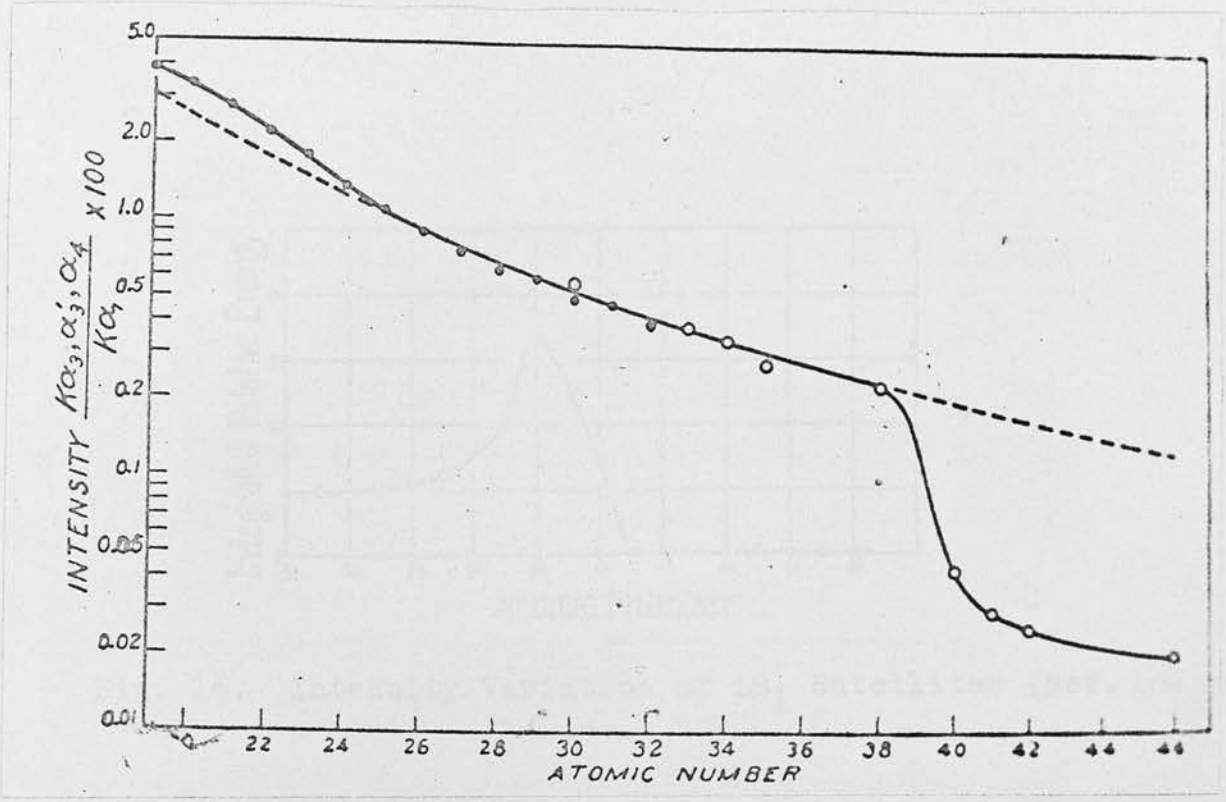

Fig. 14. Intensity Variation of Kα satellites (Ref. 104(a))

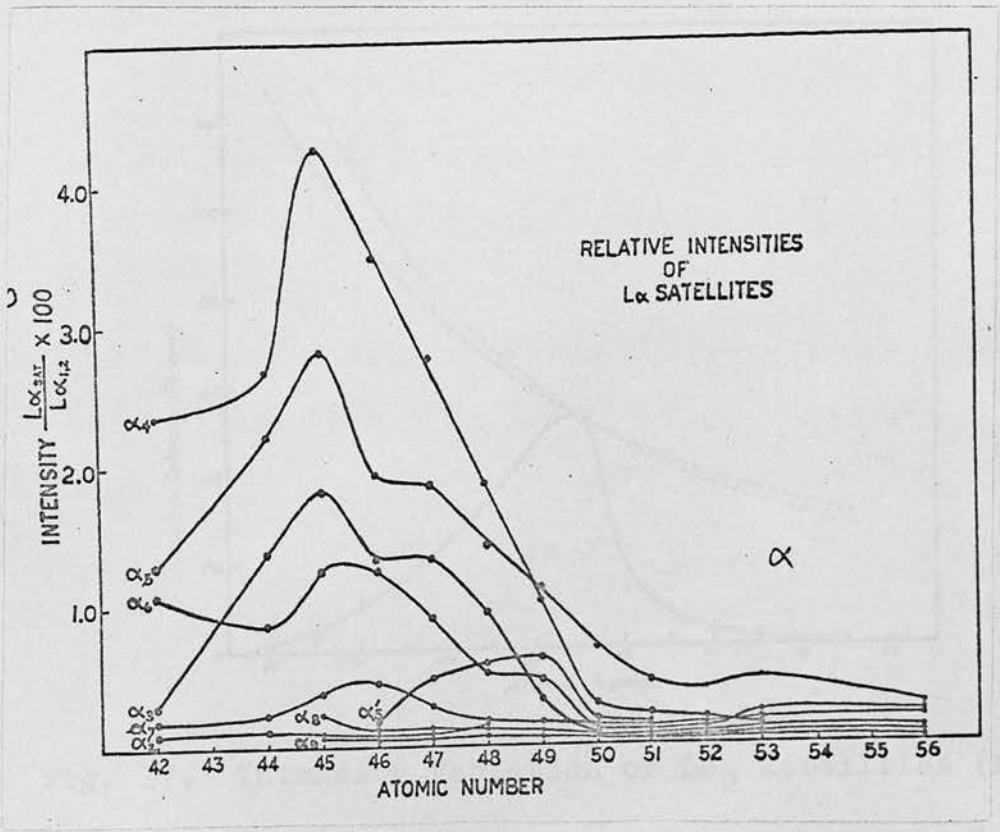

Fig. 15 (taken from Ref. 104(b))

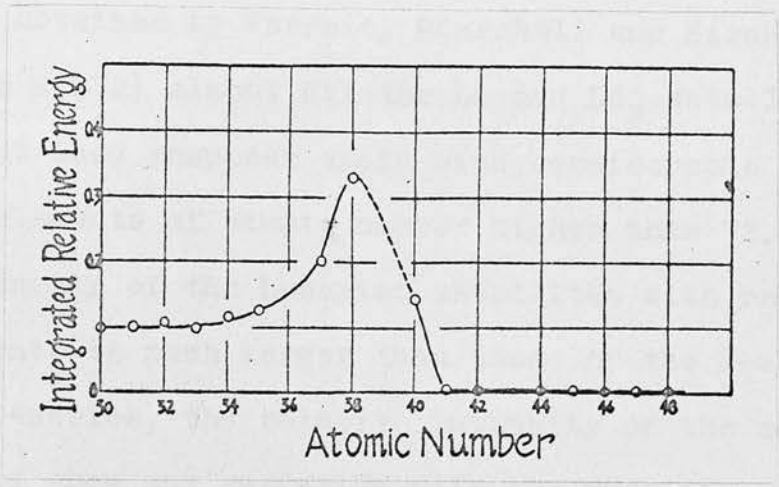

Fig. 16. Intensity Variation of $L\beta_1$ Satellites (Ref. 104(b))

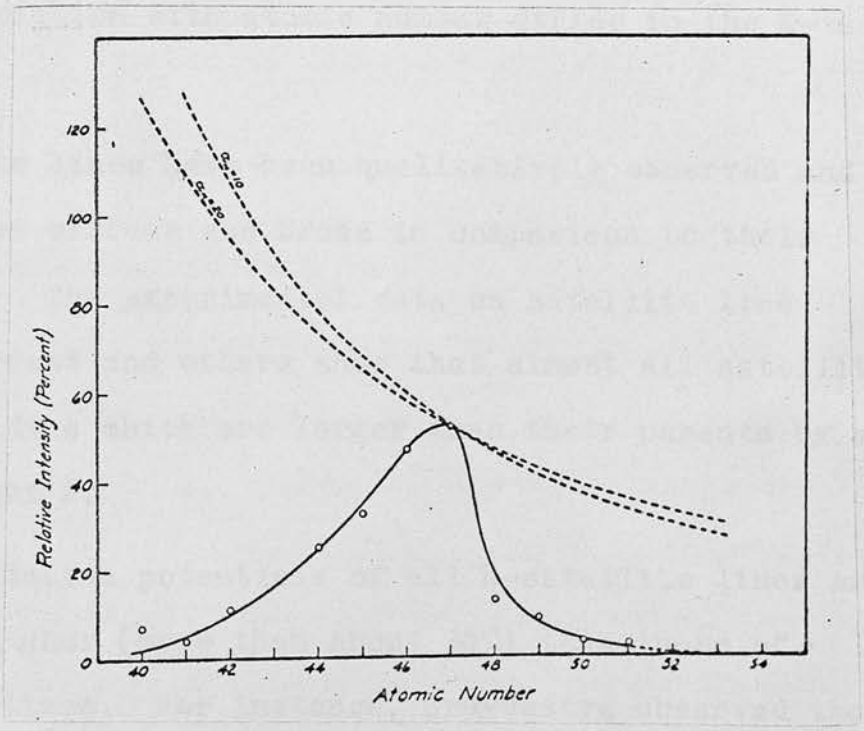

Fig. 17. Intensity Variation of $L\beta_2$ Satellites (Ref. 104(c))

intensity decreases so rapidly that the satellites become too faint to be observed at Mo(42). Figures 15, 16 and 17 show the intensity variation of $L\alpha$, $L\beta_1$ and $L\beta_2$ satellites respectively obtained by Parratt, Pearshall and Hirsh. From I(53) to Hf(72) almost all the $L\alpha$ and $L\beta_2$ satellites disappear, but they reappear again with considerable intensity for elements of atomic number higher than 72. The relative intensity of the L-series satellites with respect to their parents is much larger than those of the K-series. Also in the L-series, the relative intensity of the satellites does not show any variation with the mode of excitation, whereas in the K-series it has been observed to be greater with cathode ray excitation than with fluorescent excitation.

All these facts show that the trends of satellite intensity variation with atomic number differ in the K- and L-series.

(b) Satellite lines have been qualitatively observed and reported to be diffuse and broad in comparison to their parent lines. The experimental data on satellite line widths by Parratt and others show that almost all satellite lines have widths which are larger than their parents by a factor of about 2.

(c) The excitation potentials of all K-satellite lines are known to be higher (more than about 30%) than those of their parent lines. For instance, Druyvestyn observed the $K\alpha_3$, α_4 satellites of V(23) at a tube voltage of

6.45 ± 0.1 KV and not at 5.45 KV for which the parent lines $K\alpha_{1,2}$ are excited in this element. In the L-series satellites, however, the excitation potential does not show any significant variation and in most cases is almost the same as that corresponding to the single ionisation of the L_I level.

(d) A new group of satellites in Ag(47) was observed by Burnbank in 1939. The energy separation of the satellites in this group corresponded to those of the L-series, but the excitation potential was found to be that necessary to cause a K-shell ionisation. These satellites were later assigned to the L-series.

(e) Richtmyer showed that the square root of the frequency separation of a satellite line from its parent line is a linear function of the atomic number, though Idei, using the same set of data, obtained linearity when the frequency separation by itself is plotted against atomic number.

3.5.2 Wentzel-Druyvestyn Theory:-

A theoretical explanation of the origin of satellite lines was first proposed by Wentzel in 1921 and later modified by Druyvestyn. Hence the theory is known as the Wentzel-Druyvestyn theory. According to this theory, the satellite lines arise from single electron transitions in atoms that have been doubly or multiply ionised in their inner shells. The Kβ satellites, for example, arise in the transition KL - LM, the one electron transition being the

same as that in the Kβ line $(K \rightarrow M)$. The $K\alpha_3$, α_4 satellites have been assigned to the transition $KL\text{-}L^2$. The states of double or multiple ionisation in the inner shells of an atom can be produced by cathode ray excitation or fluorescent excitation. In the former process of excitation which is the one most commonly used, an electron of sufficient energy removes in a single collision, two or more electrons from the atom of the target element. The minimum excitation energy for the initial state of double ionisation KL is that which can eject a K electron and simultaneously or subsequently an L electron. Since the ionisation energy of an L electron in an atom from which one K electron has already been removed is approximately that for the corresponding electron in the element with the next higher atomic number, the energy $E_{KL}(Z)$ of an atom with atomic number Z in a state of double ionisation KL is given by

$$E_{KL}(Z) = E_K(Z) + E_L(Z+1) \qquad (3.20)$$

and similarly,

$$E_{LM}(Z) = E_L(Z) + E_M(Z+1) \qquad (3.21)$$

Therefore, the energy difference between the satellites (KL - LM) and the parent line (K - M) becomes

$$\Delta E = \left\{E_{KL}(Z) - E_{LM}(Z)\right\} - \left\{E_K(Z) - E_M(Z)\right\}$$

$$= \left\{E_L(Z+1) - E_L(Z)\right\} - \left\{E_M(Z+1) - E_M(Z)\right\} \qquad (3.22)$$

The L-difference being always greater than the M-difference, the satellites will appear on the higher frequency side of

the parent line. Taking the fine structure of the initial and final states into account, the Kβ satellites will, in fact, be composed of a number of lines. A similar explanation can be given for the other satellites of the K-and L-series. The energy separation of the satellites from their parent lines calculated from relations similar to (3.22) agree very well with the observed values. From eq. (3.20) one can understand why the excitation potentials of the satellites are higher than those of their parent lines.

Theoretical calculations of the Kα satellite energies for $11 \leq Z \leq 42$ have been done by Wolfe[101], Kennard and Ramberg[101], Candlin[105] and Horak[106], all of which, with slight variations, are based on Slater's theory of complex spectra in which the multiplicity of spectroscopic terms arising from the interaction of the double (or more) vacancies in the inner shells of an atom is taken into account. The results of these calculations (see Figs. 18 and 19) are in excellent agreement with the observed values, and provide conclusive evidence in favour of the Wentzel-Druyvestyn theory. No theoretical calculations for the K-satellite energies have been done for $Z > 42$ where the relativistic and spin-orbit contributions may become more important.

Druyvestyn has obtained an expression for the probability of double ionisation of an atom by direct electron impact according to which the ratio of the probability of KL double ionisation to the K ionisation is

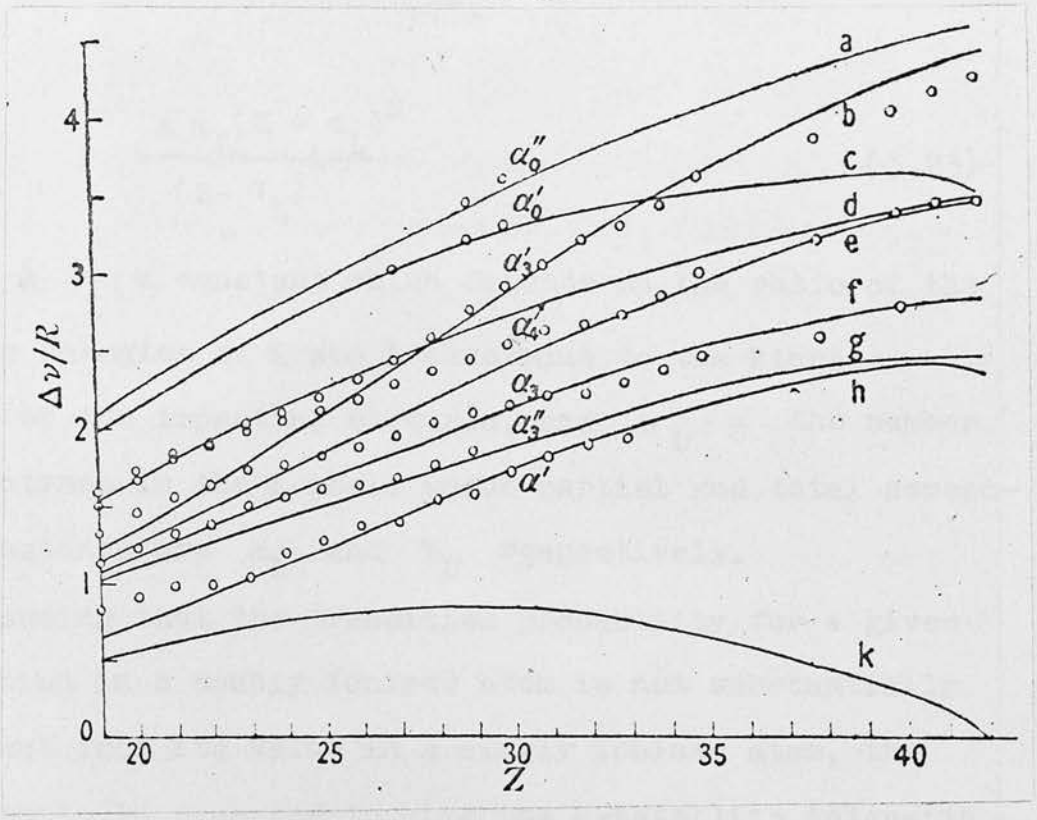

Fig. 18. Predicted $K\alpha_1$ Satellites and Experimental Points (Ref. 105).

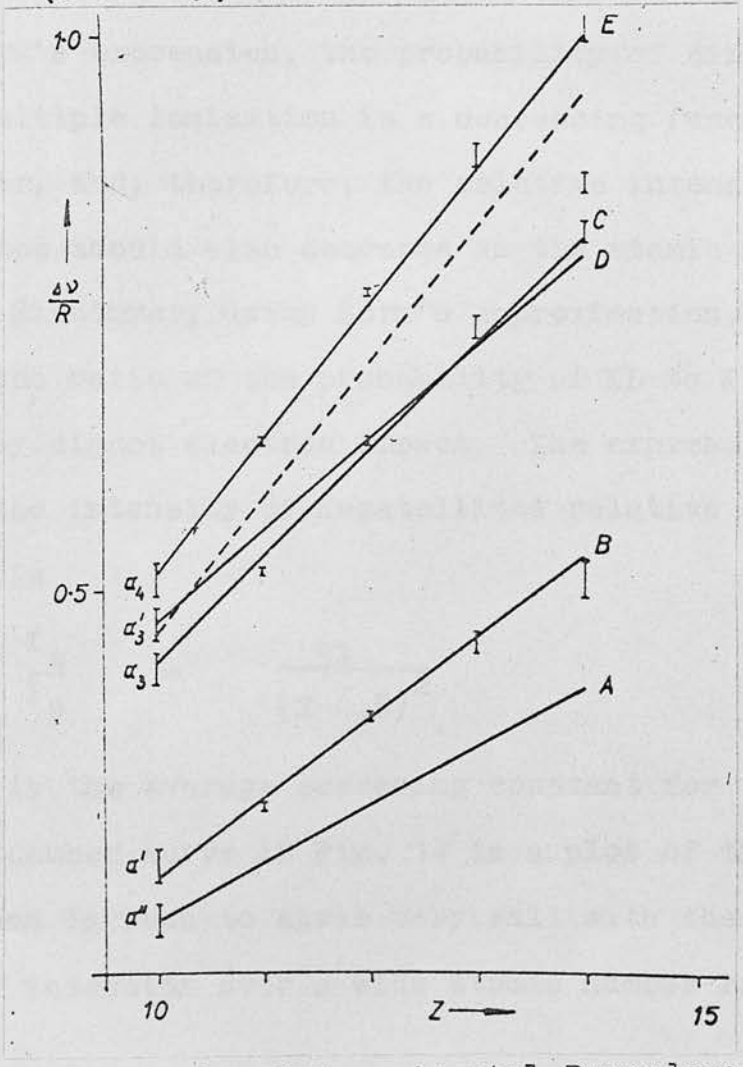

Fig. 19. Predicted and Experimental Dependence of $\Delta\nu/R$ on Z (Ref. 106).

$$\frac{A\, n_L (Z - \alpha_L)^2}{(Z - \gamma_L)^4} \qquad (3.23)$$

where A = a constant which depends on the ratio of the binding energies of K and L electrons to the kinetic energy of the impacting electron, and n_L = the number of electrons in the L shell whose partial and total screening constants are α_L and γ_L respectively.

Assuming that the transition probability for a given transition in a doubly ionised atom is not substantially different from its value in a singly ionised atom, the above ratio is expected to give the K-satellite intensity relative to the intensity of the parent line. According to Druyvestyn's expression, the probability of direct double or multiple ionisation is a decreasing function of atomic number, and, therefore, the relative intensity of the satellites should also decrease as the atomic number increases. Richtmyer, using Born's approximation, has calculated the ratio of the probability of KL to K ionisation by direct electron impact. The expression obtained for the intensity of K-satellites relative to their parent line is

$$\frac{I_s}{I_p} = \frac{91}{(Z-4.5)^2} \qquad (3.24)$$

where 4.5 is the average screening constant for the L shell. The dashed curve in Fig. 14 is a plot of the above expression and is seen to agree very well with the observed variation of intensity over a wide atomic number range.

Recently, Sachenko and Demekhin[107], and Aberg[108] have calculated the relative intensity of some K-satellites on the basis of the sudden approximation making allowance for the effect of Auger transitions on the satellite intensity. The results of their calculations are in good agreement for small Z up to Z = 24. The discrepancy for large Z is attributed to the non-availability of accurate data on the Auger widths for Z > 24.

According to the Weisskopf-Wigner theory, the width of a spectral line is the sum of the widths of the initial and final levels involved in its emission. Hence, for the satellites emitted in the transition, say, $KL_{III} - L^2_{III}$, the line width may, approximately, be taken as the sum of the width of the K level and 3 times the width of the L_{III} level. The width of the parent line of the above satellites will, on the other hand, be given by the sum of the K and L_{III} level widths. This explains why the widths of the satellite lines are larger than those of their parent lines.

Thus, all the main features of the K-series satellites seem to be reasonably accounted for by the Wentzel-Druyvestyn theory of multiple ionisation.

3.5.3 Cöster-Kronig Theory:-

While the Wentzel-Druyvestyn theory accounts very well for the K-series satellites and gives correct energy separation of the satellites from their parent lines in the other series as well, it fails to explain the curious variation of intensities in the satellites of the L and M

series. It also fails to predict correctly the excitation potentials of satellites in these series, which led to the prominence of Richtmyer's double jump theory. This theory, though it seems quite plausible from consideration of the evidence, has very limited applicability and will not be discussed here. The reason for the anomalies in the L- and M-series satellites was given by Cöster and Kronig in 1934. According to the theory advanced by these authors the satellites in the L- and M-series originate from a state of double ionisation which is produced in an Auger transition of a particular kind, now known as a Cöster-Kronig transition. For example, the initial state of double ionisation $L_{III}\,M_{IV,V}$, which gives rise to the Lα and $L\beta_2$ satellites in the transitions $L_{III}\,M_{IV,V} - M^2_{IV,V}$, and $L_{III}\,M_{IV,V} - M_{IV,V}\,N_V$ respectively, is produced from an initial vacancy L_I by the Cöster-Kronig transition $L_I \text{—} L_{III}\,M_{IV,V}$. Similarly the initial state $L_{II}\,M_{IV,V}$ in the $L\beta_1$ satellite $(L_{II}\,M_{IV,V} - M^2_{IV,V})$ results from the transition $L_I \text{—} L_{II}\,M_{IV,V}$. The single vacancy may be produced, as usual, by electron impact or by photon ionisation, and the single electron jump in the transition is the same as envisaged by the Wentzel-Druyvestyn theory. The essential condition, however, for a radiationless transition of the type $L_X \text{—} L_Y\,M_o$ to be energetically possible is

$$E_{L_X}(Z) - E_{L_Y}(Z) \geqslant E_{M_o}(Z+1) .$$

Figure 20 shows that outside the range Z = 50 - 72,

$$E_{L_I}(Z) - E_{L_{III}}(Z) > E_{M_{IV,V}}(Z+1) ,$$

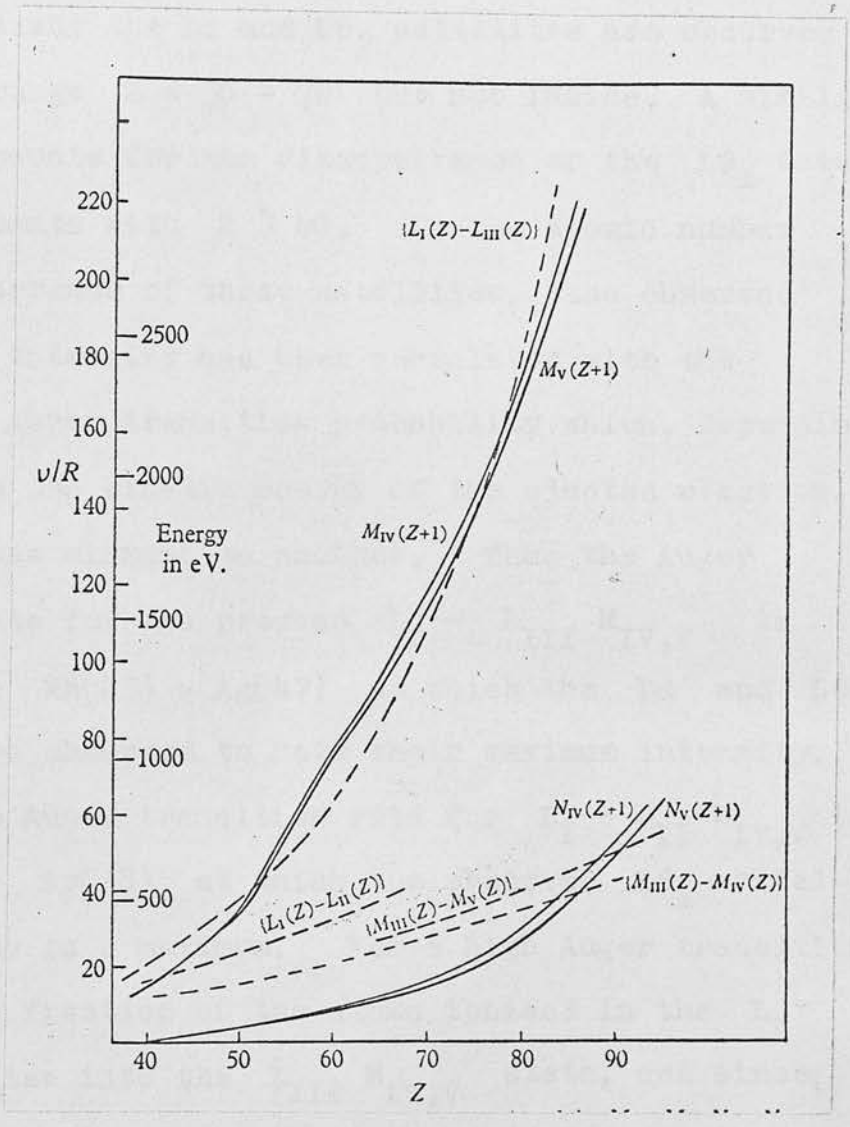

Fig. 20. Illustrating the Range of Atomic Numbers over which Various Cöster-Kronig Transitions can occur (Ref. 64).

and hence it is possible for an atom in an initial state L_I to undergo a transition $L_I — L_{III}\, M_{IV,V}$. But within the range $Z = 50\text{-}72$; because $E_{L_I}(Z) - E_{L_{III}}(Z) < E_{M_{IV,V}}(Z+1)$, this transition is no longer possible. This explains why the $L\alpha$ and $L\beta_2$ satellites are observed outside the range $Z = 50 - 72$ but not inside. A similar argument accounts for the disappearance of the $L\beta_1$ satellites in elements with $Z > 40$. In the atomic number range of occurrence of these satellites, the observed variation of intensity has been correlated with the variation of Auger transition probability which, depending critically on the kinetic energy of the ejected electron, varies from one element to another. Thus the Auger transition rate for the process $L_I — L_{III}\, M_{IV,V}$ is greatest near Rh(45) - Ag(47) at which the $L\alpha$ and $L\beta_2$ satellites are observed to have their maximum intensity. Similarly the Auger transition rate for $L_I — L_{II}\, M_{IV,V}$ is greatest near Sr(38) at which the observed $L\beta_1$ satellite intensity is a maximum. For a high Auger transition rate, a large fraction of the atoms ionised in the L_I shell reorganise into the $L_{III}\, M_{IV,V}$ state, and since, for a given ionising agent the number of atoms ionised in the L_I level is comparable to the number so ionised in the L_{III} shell, the number of atoms with double ionisation $L_{III}\, M_{IV,V}$ is comparable to the number of atoms with single ionisation L_{III}. This explains the large intensity of the L-series satellites relative to their

parents, as observed by various workers. For certain elements, the emission lines arising from L_I level (e.g. $L\beta_3$ and $L\beta_4$) are observed to be much weaker in comparison with L_{II} or L_{III} emission lines. This again is a consequence of the fact that a large number of the atoms in an initial state L_I reorganise without the emission of radiation. Since the Auger width for L_I level in these elements is much larger than that for the L_{II} and L_{III} levels, the L_I emission lines are broader than the lines arising from L_{II} or L_{III} levels. Also because almost all the L-series satellites are accounted for by the doubly ionised state produced by an Auger process from an initial L_I ionisation, it is clear why the excitation potential for L-series satellites is the same as that of the L_I level. Thus, whereas the intensity of the K-series satellites relative to their parent lines is greater with cathode ray excitation than with fluorescent excitation, the relative intensity of L-series satellites should be the same under both conditions of excitation so long as the excitation energy is sufficient to produce the initial L_I vacancy. This again is in agreement with the experimental observations.

The Burbank satellites observed in the L-series of Ag(47) have been shown to be due to the transition LL — LM where the initial state of double ionisation LL arises from the Auger transition K — LL. This explains why this satellite group was observed to be excited only when the tube voltage is sufficient to cause K-shell ionisation.

All the anomalies in the L-series satellites being

thus explained, it may be concluded that the origin of the satellite lines in the K- and L- series of X-rays is reasonably accounted for by the Wentzel-Druyvestyn theory of multiple ionisation and by the Cöster-Kronig theory of radiationless transitions.

3.5.4 X-ray satellites from K-capture:-

The K-series X-ray satellites discussed so far have been mostly studied by cathode ray excitation. But none of these satellites have been observed to arise from an initial state of double K ionisation because the probability of such an ionisation being produced in a single electron impact is very small. Recently, however, Oertzen[109] has observed some K-satellites of intensity $\sim 10^{-4}$ per K-capture in Ge^{71}. These satellites have been ascribed to the transition KK — KL. The initial state of double ionisation, KK is explained as arising from K capture accompanied by ejection or excitation of the other K-electron due to sudden nuclear charge alteration in the process of K capture. A detailed calculation for the probability of double K ionisation in atoms following K capture decay has been carried out by Primakoff and Porter[110].

Apart from the above mode of producing an additional K or L vacancy in K-capture isotopes, such vacancies may also be produced by internal conversion of a very short lived γ-transition. The probability of such a process leading to an initial KK vacancy, and hence to K-series satellites, is examined in the next chapter and applied

to estimate the lifetime of the 1720 keV E1 γ-transition in the K capture isotope Pb^{206}. This, indeed, is the objective of the present experiment.

CHAPTER IV

THE PRESENT EXPERIMENT

4.1 Introduction to the Experiment

It is well known that when an atomic nucleus captures one of its orbital electrons leaving the nucleus in an excited state, the subsequent reorganisation of the daughter atomic system is influenced by the succeeding nuclear transition if the lifetime of the nuclear transition is comparable to the atomic level lifetimes. In medium to high Z elements, the atomic level lifetimes are of the order of 10^{-16} seconds which is comparable to the lifetime of the nuclear E1 transition of $\sim$1 MeV. This implies that in these elements one might expect to observe the effect of such E1 nuclear transitions on the atomic transitions. One such observed effect is the emission of positrons following electron capture decay. When an excited nuclear level decays by pair formation (i.e. creation of electron-positron pair) in the presence of an electron capture vacancy, this vacancy may be filled by the electron of the created pair with resulting emission of a positron. In section 2.7, an expression has been deduced for the intensity of the positrons emitted, and its application to the measurement of the 1863 keV E1 transition in Bi^{205} and 1409 keV E1 transition in Sm^{152} has been discussed.

In the present experiment, an entirely different effect of the nuclear E1 transition on the atomic

transition following electron capture in the high Z elements has been contemplated - the emission of K X-ray satellites. By observations on these K X-ray satellites it is possible to estimate the lifetime of E1 transitions in medium to heavy Z elements. Bokosah[23] has applied this method in a very simple and unsophisticated form to measure the lifetime of the 1409 keV E1 γ-transition in Sm^{152} following K-capture decay of Eu^{152}. In the present experiment the probability of K X-ray satellite emission associated with the 1720 keV E1 γ-transition of Pb^{206} following the electron capture decay of Bi^{206} has been examined more exhaustively and an experimental determination of the lifetime of this nuclear transition has been undertaken.

Bi^{206} decays by electron capture (mainly K and L capture) to Pb^{206} producing a highly complex spectrum shown in Figure 33 . In most cases, the electron capture vacancy, say the K-vacancy, will be filled up before the 1720 keV E1 γ-ray is emitted. The conversion of this γ-ray in the K-shell leaves the atom singly ionised in the K-shell, and this will give rise to the normal K X-rays. But in some cases, the 1720 keV E1 γ-ray may be converted in the K-shell in the presence of the K capture vacancy. When this happens, the atom will be left doubly ionised in the K-shell (i.e. with a KK vacancy) giving rise to the K X-ray satellites in the transition KK → KL which according to the Wentzel-Druyvestyn hypothesis are higher in energy than the normal K X-rays. A further transition,

KL - LM, will produce another type of K X-ray satellites slightly different in energy from the previous ones. In fact any process by which an initial state of double vacancy KK, KL or KM may be produced will give rise to the K X-ray satellites provided the K vacancy is then filled by a radiative process before the other vacancy disappears. The various processes by which different initial conditions of double inner shell ionisation, KK, KL or KM can be produced with subsequent emission of K X-ray satellites have been examined in section (4.2) and an expression for the relative intensity of the K X-ray satellites has been derived. The expression involves the lifetime of the 1720 keV E1 γ-transition, the lifetimes of the various atomic levels and some other coefficients. The latter two being either experimentally known or computable, the problem of the lifetime determination of the E1 γ-ray therefore reduces to the measurement of the intensity of the K X-ray satellites, associated with this E1 transition.

In order to determine the intensity of the K X-ray satellites, a coincidence experiment was set up which will be described in the next chapter. The normal and satellite K X-rays resulting from the internal conversion of the 1720 keV E1 γ-ray could be selected for study by observing coincidences between the K X-rays of Pb^{206} and the internal conversion electrons of this γ-ray. On the other hand, coincidence between the K X-rays of Pb^{206} and the internal conversion electrons of any suitable E2 or M1 transition in Pb^{206} spectrum would select only the normal K X-rays.

E2 or M1 transitions are so long lived in comparison to the atomic inner level lifetimes that an inner atomic vacancy produced by the electron capture would invariably be filled up before the conversion of the γ-ray took place. Hence, there would be practically no K X-ray satellites associated with the E2 or M1 transitions. For reasons of intensity and because it stands out clearly in the Pb^{206} spectrum (see Fig 34, Chapter V), the 184 keV M1 γ-transition was selected for the latter coincidence experiment. With this method of selecting the normal K X-rays and the group of normal and satellite K X-rays, the K X-ray satellite intensity can be estimated by measuring, for two suitable absorbers of different thicknesses, the ratio of coincidence counting rate with and without the absorbers. An expression for the intensity of the K X-ray satellites in terms of these measured intensity reductions has been derived in section (4.3). The discussion of the choice of suitable absorbers is deferred until the next chapter.

4.2 Theoretical Expression for the Relative Intensity of the K X-ray Satellites

It is possible to calculate the ratio of the number of satellite K X-rays to the total number of normal and satellite K X-rays which are in coincidence with the K conversion electrons of an E1 γ-ray emitted after electron capture in a radioactive isotope.

Satellite K X-rays can arise from three different

initial conditions, corresponding to double vacancies of the types (a) KK, (b) KL and (c) KM. Satellite K-X-rays will occur if the K vacancy is filled by a radiative transition before the other vacancy is removed. The probability of this for the three initial conditions may be obtained as follows.

Let F_K, F_{L_I} etc. be the probability of formation (by K electron capture, L_I electron capture, etc.) of the nuclear excited state from which the γ-ray is emitted. Let p be the probability of de-excitation of the state by the emission of the El γ-ray, α_K the internal conversion coefficient of the γ-ray in the K shell, α_L the internal conversion coefficient of the γ-ray in the L shell, and ω_K the fluorescence yield of a vacancy in the K shell. It is assumed that the fluorescence yield is the same whether or not there are additional vacancies in the atom. Let γ be the decay constant of the nuclear excited state and K, L_I etc. be the corresponding decay constants for the vacancies in the K, L_I etc. shells.

4.2.1 Satellite K X-rays arising from the KK vacancy:

The probability of the El γ-ray being emitted in time t secs. $= (1 - e^{-\gamma t})$.

The probability of the K capture vacancy disappearing in the interval t to t + dt $= Ke^{-Kt}\,dt$.

∴ The probability of the El γ-ray being emitted before the K capture vacancy disappears

$$= \int_0^\infty (1 - e^{-\gamma t})Ke^{-Kt}\,dt$$

$$= K \left[-\frac{1}{K} e^{-Kt} \right]_0^\infty - K \left[-\frac{1}{K+\gamma} e^{-(K+\gamma)t} \right]_0^\infty$$

$$= 1 - \frac{K}{K+\gamma}$$

$$= \frac{\gamma}{K+\gamma} \qquad (4.1)$$

Therefore, the probability of formation of a KK vacancy by the K conversion of the E1 γ-ray before the K capture vacancy has been filled

$$= F_K \, p \, \frac{\alpha_K}{2} \left(\frac{\gamma}{K+\gamma} \right) \quad ,$$

the internal conversion coefficient being reduced by half since there is only one electron in the K shell when conversion occurs.

∴ The probability of emission of a K X-ray satellite from the KK vacancy

$$= F_K \, p \, \frac{\alpha_K}{2} \left(\frac{\gamma}{K+\gamma} \right) \times \omega_K \qquad (4.2)$$

4.2.2 Satellite K X-rays arising from KL vacancy:

This can occur in a number of ways:

(a) If the γ-ray is converted in the K shell before an L capture vacancy disappears, then this would give a KL vacancy and hence K X-ray satellites provided the K vacancy is filled before the L vacancy disappears.

Since the probability of the γ-being emitted before the L vacancy formed by L capture disappears is $\left(\frac{\gamma}{L+\gamma} \right)$,

and the probability of the K vacancy being filled by a radiative transition before the L vacancy disappears is $(\frac{K}{K+L}) \times \omega_K$, the probability of emission of K X-ray satellites by KL vacancy formation in the above-mentioned manner

$$= F_L \; p \; \alpha_K \; (\frac{\gamma}{L+\gamma})(\frac{K}{K+L}) \times \omega_K \quad .$$

Considering the various L sub-sbells separately, the probability of emission of K X-ray satellites is,

$$F_{L_I} \; p \; \alpha_K \; (\frac{\gamma}{L_I+\gamma})(\frac{K}{K+L_I}) \times \omega_K \qquad (4.3)$$

+ similar terms for L_{II} and L_{III} subshells.

(b) If the vacancy in the K shell produced by K capture is transferred to the L shell (either by a radiative process or an Auger process) before the gamma ray is converted in the K-shell, then this would also give rise to a KL vacancy and hence K X-ray satellites provided the K vacancy is filled before the L vacancy disappears.

The probability of a K vacancy being filled at time t_1 to $t_1 + dt_1$ and forming a vacancy in the L shell

$$= Ke^{-Kt_1} \, dt_1 . \beta$$

where β is the probability of a K vacancy giving rise to a vacancy in the L shell either by radiative or Auger process.

Probability of L vacancy lasting from time t_1 to $t + dt$

$$= Le^{-L(t_1-t)} \, dt \quad ,$$

and the probability of the γ-ray being emitted in period t_1 to t

$$= \int_{t_1}^{t} \gamma e^{-\gamma t}\, dt \quad = \quad (e^{-\gamma t_1} - e^{-\gamma t}) \quad .$$

Multiplying these and integrating gives the probability of a KL vacancy occurring

$$= -\beta \int_{o}^{\infty} \int_{t_1}^{\infty} K e^{-Kt_1} \cdot L e^{-L(t-t_1)} (e^{-\gamma t} - e^{-\gamma t_1}) dt_1 dt$$

$$= - KL\beta \int_{o}^{\infty} \int_{t_1}^{\infty} \left[e^{-Kt_1+Lt_1} e^{-Lt-\gamma t} - e^{-Kt_1+Lt_1-\gamma t_1} \cdot e^{-Lt} \right] dt_1\, dt.$$

$$= - KL\beta \left\{ \int_{o}^{\infty} e^{-Kt_1+Lt_1} \left[-\frac{1}{(L+\gamma)} e^{-(L+\gamma)t} \right]_{t_1}^{\infty} dt_1 \right.$$

$$\left. - \int e^{-Kt_1+Lt_1-\gamma t_1} \left[-\frac{1}{L} e^{-Lt} \right]_{t_1}^{\infty} dt_1 \right\}$$

$$= - KL\beta \left\{ \int_{o}^{\infty} \left[e^{-Kt_1+Lt_1} \frac{1}{L+\gamma} e^{-(L+\gamma)t_1} - e^{-Kt_1+Lt_1-\gamma t_1} \cdot \frac{1}{L} e^{-Lt_1} \right] dt_1 \right\}$$

$$= - \frac{KL}{L+\gamma} \beta \int_{o}^{\infty} e^{-(K+\gamma)t_1} dt_1 + \beta K \int_{o}^{\infty} e^{-(K+\gamma)t_1} dt_1$$

$$= \left(\frac{KL}{L+\gamma}\right)\beta \int_{\infty}^{o} e^{-(K+\gamma)t_1} dt_1 - K\beta \int_{\infty}^{o} e^{-(K+\gamma)t_1} dt_1$$

$$= \left(\frac{KL}{L+\gamma}\right)\beta \left(-\frac{1}{K+\gamma}\right) + \frac{K\beta}{K+\gamma}$$

$$= \left(\frac{K}{K+\gamma}\right)\left[\,1 - \frac{L}{L+\gamma}\,\right]\beta$$

$$= \left(\frac{K}{K+\gamma}\right)\left(\frac{\gamma}{L+\gamma}\right)\beta$$

and since the probability of the K vacancy being filled before the L vacancy disappears (by radiative transition)

$$= \left(\frac{K}{K+L}\right)\omega_K \quad ,$$

the probability of emission of KL satellites in this way

$$= F_K\, p\, \alpha_K \left(\frac{K}{K+\gamma}\right)\left(\frac{\gamma}{L+\gamma}\right)\left(\frac{K}{K+L}\right)\beta \times \omega_K \quad .$$

Taking the L subshells separately gives probability for K_{L_I} satellites

$$= F_K\, p\, \alpha_K \left(\frac{K}{K+\gamma}\right)\left(\frac{\gamma}{L_I+\gamma}\right)\left(\frac{K}{K+L_I}\right) A_{L_I} \times \omega_K \qquad (4.4)$$

probability of $K_{L_{II}}$ satellites

$$= F_K\, p\, \alpha_K \left(\frac{K}{K+\gamma}\right)\left(\frac{\gamma}{L_{II}+\gamma}\right)\left(\frac{K}{K+L_{II}}\right) A_{L_{II}} \times \omega_K \qquad (4.5)$$

probability of $K_{L_{III}}$ satellites

$$= F_K\, p\, \alpha_K \left(\frac{K}{K+\gamma}\right)\left(\frac{\gamma}{L_{III}+\gamma}\right)\left(\frac{K}{K+L_{III}}\right) A_{L_{III}} \times \omega_K \qquad (4.6)$$

where β has been replaced by A_{L_I}, $A_{L_{II}}$, $A_{L_{III}}$, and these are the probabilities of a K vacancy being shifted to L_I, L_{II}, L_{III} subshells respectively, either by radiative or Auger process.

(c) After the emission of a satellite K X-ray arising from a double K vacancy, or by an Auger process from the same initial state, the atom may be left with vacancies in the

K and L shells which will give rise to additional KL satellites provided the K vacancy is filled by a radiative transition before the L vacancy disappears.

The probability of KL satellites by this process

$$= F_K \, p \, \frac{\alpha_K}{2} \left(\frac{\gamma}{K+\gamma}\right)\left(\frac{K}{K+L_I}\right) A_{L_I} \times \omega_K \qquad (4.7)$$

+ similar terms for the L_{II} and L_{III} shells.

(d) Finally, a KL vacancy can also occur if the γ-ray is converted in the L shell while there is still a vacancy in K shell.

Since the probability of a γ-ray being emitted in the presence of the K capture vacancy is $\left(\frac{\gamma}{K+\gamma}\right)$, the probability of a KL vacancy occurring due to the γ-ray being converted in the L shell

$$= \left(\frac{\gamma}{K+\gamma}\right) \times \alpha_L$$

and this will give rise to additional KL satellites provided the K vacancy is filled by a radiative transition before the L vacancy disappears.

The probability of KL satellites by this process

$$= F_K \, p \, \alpha_{L_I} \left(\frac{\gamma}{K+\gamma}\right)\left(\frac{K}{K+L_I}\right) \times \omega_K \qquad (4.8)$$

+ similar terms for the L_{II} and L_{III} subshells.

4.2.3 Satellite K X-rays arising from KM vacancy:

This also can occur in a great number of ways:-

(a) The γ-ray may be converted in the K shell while there is an M vacancy produced by M capture. This will give rise to a KM vacancy which will give KM satellites provided the K vacancy is filled by a radiative transition before the M vacancy disappears.

The probability of KM satellites by this process

$$= F_{M_I}\, p\, \alpha_K \left(\frac{\gamma}{M_I+\gamma}\right)\left(\frac{K}{K+M_I}\right) \times \omega_K \qquad (4.9)$$

+ similar terms for the other M subshells.

(b) The vacancy in the K shell produced by K capture may be transferred directly to the M shell either by a radiative or an Auger process before the γ-ray is converted in the K shell. The KM vacancy thus produced will again give rise to K X-ray satellites provided the K vacancy is filled by radiative process before the M vacancy disappears. As in 3.2.2(b) the probability of KM satellites by this process

$$= F_K\, p\, \alpha_K \left(\frac{K}{K+\gamma}\right)\left(\frac{\gamma}{M_I+\gamma}\right)\left(\frac{K}{K+M_I}\right) \times B_{M_I} \times \omega_K \qquad (4.10)$$

+ similar terms for the other M subshells.

Here B_{M_I}, $B_{M_{II}}$ etc. are the probabilities of a K vacancy giving rise to a vacancy in M_I, M_{II} etc. shells respectively, either by an Auger process or, where permissible, by a radiative process.

(c) After the emission of a satellite K X-ray arising from a double K vacancy, or by an Auger process from the same initial state, the atom may be left with vacancies in the K and M shells which will give rise to additional satellites provided the K vacancy is filled by a radiative process before the M vacancy disappears. As in 3.2.2 (c), the probability of KM satellites in this case

$$= F_K \, p \, \frac{\alpha_K}{2} \left(\frac{\gamma}{K+\gamma}\right)\left(\frac{K}{M_I+K}\right) \times B_{M_I} \times \omega_K \qquad (4.11)$$

+ similar terms for the other M subshells.

(d) The vacancy in the L shell produced by L capture may be transferred to the M shell before the γ-ray is converted in the K shell. The KM vacancy thus produced will give rise to satellite K X-rays provided the K vacancy is filled by a radiative process before the M vacancy disappears. Probability of the L vacancy disappearing before γ-emission and shifting to M shell

$$= \sum_i \left(\frac{L_i}{L_i+\gamma}\right) \times C_M \quad ,$$

where C_M is the probability of an L vacancy giving rise to a vacancy in the M shell. The summation extends over the three L-subshells.

Probability of a γ-ray being emitted and converted in the K shell before the M vacancy disappears

$$= \left(\frac{\gamma}{M_I+\gamma}\right) \alpha_K$$

and the probability of a K vacancy being filled by a radiative process before the M vacancy disappears

$$= \left(\frac{K}{K+M_I}\right) \times \omega_K \ .$$

$\therefore$ the probability of KM satellites by this process

$$= \left\{\sum_i F_{L_i}\ p\ \alpha_K \left(\frac{L_i}{L_i+\gamma}\right)\right\}\left(\frac{\gamma}{M_I+\gamma}\right)\left(\frac{K}{K+M_I}\right) C_{M_I} \times \omega_K$$

+ similar terms for the other M subshells (4.12)

(e) The vacancy in the K shell produced by K-capture may be transferred via the L shell to the M shell before the γ-ray is converted in the K shell, the K vacancy then being filled by radiative process before the M vacancy disappears.

The probability of KM satellites in this case

$$= F_K\ p\ \alpha_K \left(\frac{K}{K+\gamma}\right)\left(\sum_i \left(\frac{L_i}{L_i+\gamma}\right) A_{L_i}\right)\left(\frac{\gamma}{M_I+\gamma}\right)\left(\frac{K}{K+M_I}\right) \times C_{M_I} \times \omega_K$$

+ similar terms for the other M subshells (4.13)

(f) Finally a KM vacancy can also occur if the γ-ray is converted in the L shell in the presence of the K-capture vacancy, the L vacancy then being transferred to the M shell. This will again give rise to satallite K X-rays provided the K vacancy is filled by a radiative process before the M vacancy disappears.

The probability of KM satellites by this process

$$= F_K\ p \left(\frac{\gamma}{K+\gamma}\right)\left\{\sum_i \alpha_{L_i} \left(\frac{L_i}{K+L_i}\right)\right\}\left(\frac{K}{K+M_I}\right) \times C_{M_I} \times \omega_K$$

+ similar expressions for the other M subshells

(4.14)

Adding the expressions (4.2) - (4.14) and re-arranging gives the total probability of satellite K X-rays

$$= F_K \alpha_K p \omega_K \left(\frac{\gamma}{K+\gamma}\right) \left[\tfrac{1}{2} + \frac{K}{2} P + K^2 Q + K(K+\gamma)R\right] \quad (4.15)$$

where

$$P = \sum_i \frac{A_{L_i}}{(L_i+\gamma)} + \sum_j \frac{B_{M_j}}{(K+M_j)} + \sum_i \frac{\alpha_{L_i}}{\alpha_K} \left(\frac{2}{K+L_i}\right) \quad (4.16)$$

$$Q = \sum_i \frac{A_{L_i}}{(L_i+\gamma)(K+L_i)} + \sum_j \frac{B_{M_j}}{(M_j+\gamma)(K+M_j)}$$

$$+ \sum_i \sum_j \frac{L_i \, A_{L_i} \, C_{M_j}}{(L_i+\gamma)(M_j+\gamma)(K+M_j)} + \sum_i \sum_j \frac{1}{K} \frac{\alpha_{L_i}}{\alpha_K}$$

$$\cdot \frac{L_i \, C_{M_j}}{(K+L_i)(K+M_j)} \quad (4.17)$$

$$R = \sum_i \frac{F_{L_i}}{F_K(L_i+\gamma)(K+L_i)} + \sum_j \frac{F_{M_j}}{F_K(M_j+\gamma)(K+M_j)}$$

$$+ \sum_i \sum_j \frac{F_{L_i} \, L_i \, C_{M_j}}{F_K(L_i+\gamma)(M_j+\gamma)(K+M_j)} \quad (4.18)$$

4.2.4 Probability of total radiative transitions (satellites + normal K X-rays):-

The total probability of emission of normal or satellite K X-rays, which are coincident in time with the K conversion electrons of the El γ-ray, is composed of three parts:

(a) Normal or satellite K X-rays arising from the K capture vacancy followed by K conversion.

The probability of radiative transition in this case

$$= 2 \left[F_K \, p \, \alpha_K \left(\frac{K}{K+\gamma}\right) \times \omega_K + F_K \, p \, \frac{\alpha_K}{2} \left(\frac{\gamma}{K+\gamma}\right) \times \omega_K \right] \quad (4.19)$$

Since, $\frac{\gamma}{K+\gamma}$ = probability of the γ being emitted before the K vacancy disappears,

$\therefore$ $1 - \left(\frac{\gamma}{K+\gamma}\right) = \frac{K}{K+\gamma}$ = probability of the γ not appearing before the K vacancy disappears.

Thus, the first part of the expression within the bracket refers to the probability of a radiative transition after the K-capture vacancy has disappeared, and the second part refers to the probability of radiative transition when conversion takes place in the presence of the K-capture vacancy. The factor 2 before the bracket comes in because the K X-rays can arise due to K conversion as well as due to K-capture.

(b) Normal or satellite K X-rays arising from the L or M capture vacancy followed by K-conversion.

The probability of a radiative transition in this case

$$= \left(F_{L_I} + F_{L_{II}} + F_{L_{III}} + F_M\right) p \, \alpha_K \, \omega_K$$

$$= (1 - F_K) \, p \, \alpha_K \, \omega_K \quad (4.20)$$

(c) Normal or satellite K X-rays arising from the K-capture vacancy followed by L-conversion.

The probability of a radiative transition in this case

$$= F_K \, p \, \alpha_L \, \omega_K \qquad (4.21)$$

The fact that the L-conversion electrons may also be counted along with the K-conversion electrons justifies the inclusion of this term.

Adding expressions (4.19), (4.20) and (4.21) gives the total probability of normal and satellite K X-rays

$$= F_K \, p \, \alpha_K \, \frac{2K+\gamma}{K+\gamma} \omega_K + (1 - F_K) \, p \, \alpha_K \, \omega_K + F_K \, p \, \alpha_L \, \omega_K$$

$$= p \, \alpha_K \, \omega_K \, \frac{F_K \, K+(K+\gamma)}{K+\gamma} + F_K \, p \, \alpha_L \, \omega_K$$

$$= F_K \, \alpha_K \, p \, \omega_K \left[\frac{K + \frac{1}{F_K} (K+\gamma)}{K+\gamma} + \frac{\alpha_L}{\alpha_K} \right] \qquad (4.22)$$

Dividing (4.15) by (4.22) gives the ratio (S) of the total number of satellite K X-rays to the total number of K X-rays (normal + satellites). After cancellation of the common factors $F_K \, p \, \alpha_K \, \omega_K$,

$$S = \frac{\left(\frac{\gamma}{K+\gamma}\right) \left[\tfrac{1}{2} + \frac{K}{2} P + K^2 Q + K(K+\gamma) R \right]}{\left[\frac{K + \frac{1}{F_K} (K+\gamma)}{K+\gamma} + \frac{\alpha_L}{\alpha_K} \right]}$$

or

$$S = \frac{\gamma\left[\frac{1}{2} + \frac{K}{2}P + K^2Q + K(K+\gamma)R\right]}{K + \frac{1}{F_K}(K+\gamma) + \frac{\alpha_L}{\alpha_K}(K+\gamma)} \qquad (4.23)$$

where P, Q and R are given by expressions (4.16), (4.17) and (4.18) respectively.

Eq. (4.23) is then the desired theoretical expression for the relative intensity of the satellite K X-rays.

4.3 Satellite Intensity (S) in Terms of the Measured Intensity Reductions

It has been pointed out earlier in this chapter that the intensity of the K X-ray satellites can be deduced by measuring the intensity reduction with two absorbers of different thicknesses for (a) coincidence counting rate between the K X-rays and the K-conversion electrons of the 184 keV M1 transition of Pb^{206}, and (b) coincidence counting rate between the K X-rays and the K-conversion electrons of the 1720 keV E1 transition of Pb^{206}. According to the discussions of section (4.1), the K X-rays in coincidence with the conversion electrons of 184 keV M1 transition are the normal K X-rays, while the K X-rays in coincidence with the conversion electrons of the 1720 keV E1 transition are both the normal and the satellite K X-rays. Let the two absorbers be designated as thin and thick absorbers, and let,

R_1 = measured intensity reduction for the normal K X-rays with the thin absorber.

R_2 = measured intensity reduction for the normal K X-rays with the thick absorber.

R_1' = measured intensity reduction for the group of normal and satellite K X-rays with the thin absorber.

R_2' = measured intensity reduction for the group of normal and satellite K X-rays with the thick absorber.

K_1 = mass absorption coefficient (μ/ρ) of the absorbers for the normal $K\alpha_1$ X-rays.

K_2 = mass absorption coefficient of the absorbers for the normal $K\alpha_2$ X-rays.

K_3 = mass absorption coefficient of the absorbers for the normal $K\beta_1'$ X-rays.

K_4 = mass absorption coefficient of the absorbers for the normal $K\beta_2'$ X-rays.

K_s = mean mass absorption coefficient of the absorbers for all the K-satellites, the satellites being supposed to form a group with a mean wavelength, λ_s.

Also let,

x_1 = thickness (in gms/cm^2) of the thin absorber, and

x_2 = thickness (in gms/cm^2) of the thick absorber.

The intensities of the components $K\alpha_1$, $K\alpha_2$, $K\beta_1'$ and $K\beta_2'$, of the normal K X-rays for lead, as given by Wapstra[75], are in the ratio 100 :55.3: 35.5 : 10.2 Normalising the intensities to unity gives for R_1 and R_2 the following expressions:-

$$R_1 = .4975e^{-K_1x_1} + .2751e^{-K_2x_1} + .1766e^{-K_3x_1} + .0508e^{-K_4x_1} \quad (4.24)$$

$$R_2 = .4975e^{-K_1x_2} + .2751e^{-K_2x_2} + .1766e^{-K_3x_2} + .0508e^{-K_4x_2} \quad (4.25)$$

The mass absorption coefficients for the various components of the K X-rays being known, equations (4.24) and (4.25) can be solved numerically for x_1 and x_2 with the measured values of R_1 and R_2.

Now,

$$S = \frac{\text{Number of satellite K X-rays}}{\text{Total number of normal and satallite K X-rays}}$$

$$\therefore \quad 1 - S = \frac{\text{Number of normal K X-rays}}{\text{Number of normal and satellite K- X-rays}}$$

This means that for transitions, where K-satellites are emitted,

$$R_1' = (1 - S)R_1 + Se^{-K_s x_1} \quad (4.26)$$

$$R_2' = (1 - S)R_2 + Se^{-K_s x_2} \quad (4.27)$$

On rearrangement, the above two equations give,

$$S = \frac{R_1 - R_1'}{R_1 - e^{-K_s x_1}} = \frac{R_2 - R_2'}{R_2 - e^{-K_s x_2}} \quad (4.28)$$

Equation (4.28) is the expression for the satellite

intensity in terms of the measured intensity reductions. Using the experimentally measured values of R_1, R_2, R_1' and R_2', x_1 and x_2, the above equation can be solved numerically for K_s which can then be used to deduce S. The value of S thus estimated from the experimental observations can be fed into equation (4.23) which can be solved numerically for Υ, the transition probability of the 3404 keV level in Pb^{206}, assuming that the various probabilities occurring in this equation are known. The details of the procedure adopted for obtaining the values of the quantities involved in equations (4.23) and (4.28) will be discussed in Chapter VI.

CHAPTER V

THE EXPERIMENTAL PROCEDURE

5.1 The Detecting System

The collimated detecting system shown in Figs. 21 and 22 was made up of three parts: (a) the β-detector, (b) the γ-detector, and (c) the collimator.

(a) The β-detector:-

The β-detector was a cylindrical piece of NE 102A plastic scintillator 2 cm. long and 3 cm. in diameter with a well shaped hole machined into it as shown in Fig. 23. The diameters of the top and bottom ends of the trough were 2 cm.. and 1 cm. respectively, and the thickness of the plastic from the bottom of the trough to the other end was 1 cm. - sufficient to stop electrons up to 2 Mev in energy. Two such crystals were machined - one was used to hold the Bi^{206} source, and the other was used with a Bi^{207} source required for the preliminary experiments. The source in each case was put at the bottom of the trough. A thin coating of light reflecting paint was given to the sides of the crystals and optical contact with the photomultiplier was obtained using silicon vacuum grease. The EMI photomultiplier type 6097B and a dynode resistor chain were mounted inside a brass tube 21 cm.. in length and 8.8 cm.. in diameter, having a flange at each end. The bottom end of the tube was screwed on to a

The Detecting System (General View).

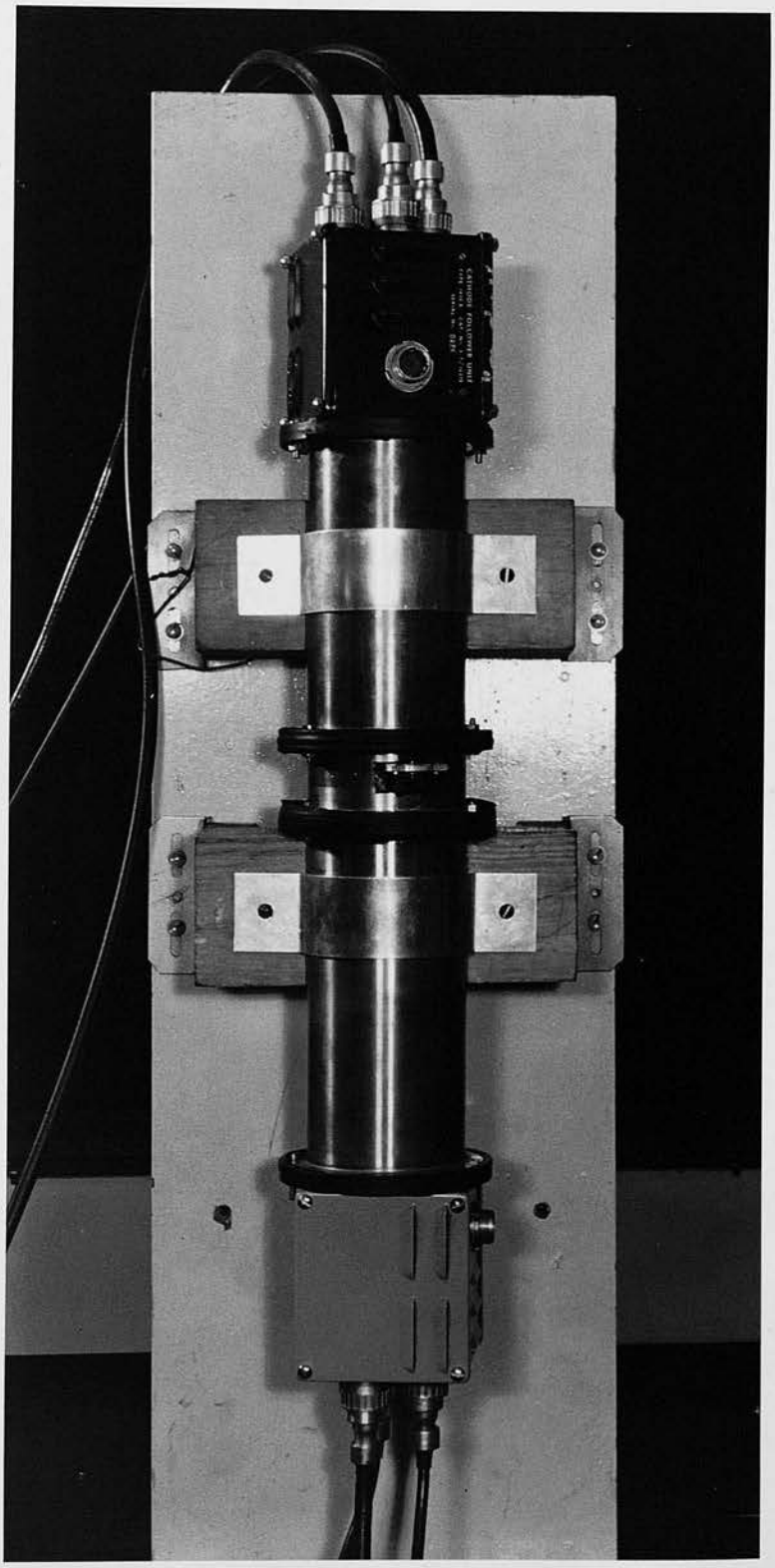

Fig. 21

FIG.22 THE DETECTING SYSTEM

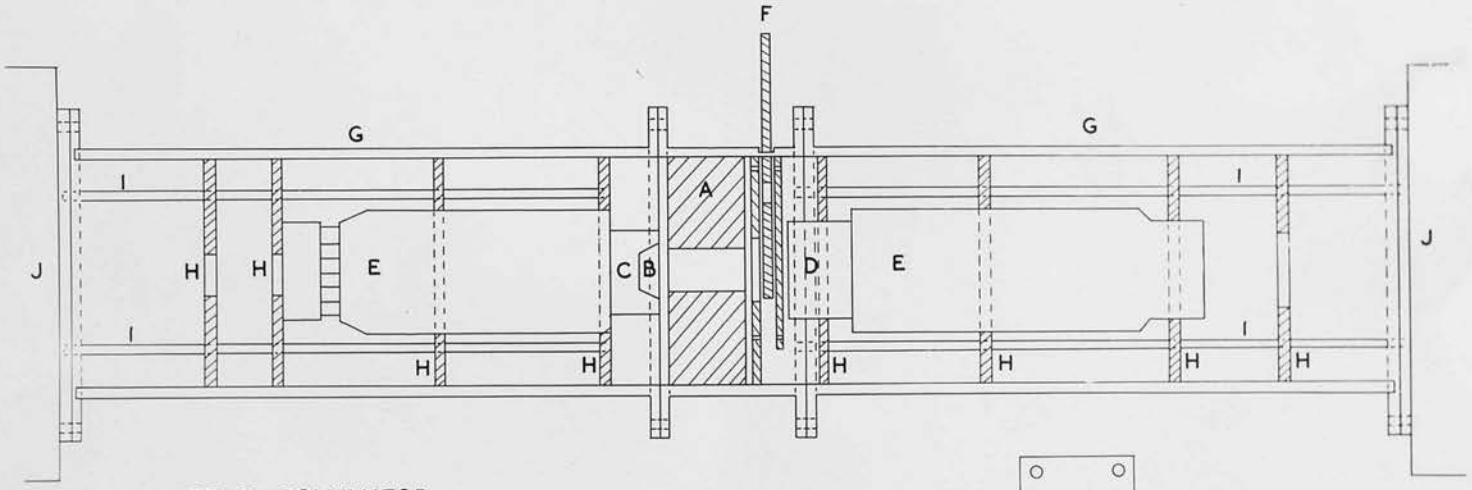

A BRASS COLLIMATOR
B SOURCE
C PLASTIC SCINTILLATOR
D NAI SCINTILLATOR WITH ALUMINIUM CAP
E PHOTOMULTIPLIERS
F MOVABLE ABSORBER
G BRASS TUBES LIGHT TIGHT
H PERSPEX & EBONITE RINGS TO HOLD PHOTOMULTIPLIERS HORIZONTAL
I SCREWED ROD
J CATHODE FOLLOWER

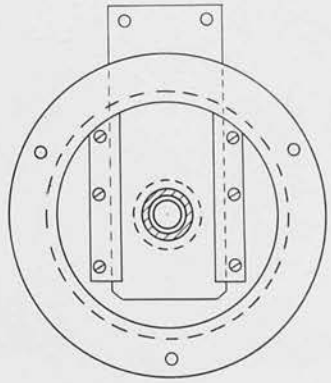

END VIEW SHOWING COLLIMATING PLATE IN POSITION

The Plastic Scintillator

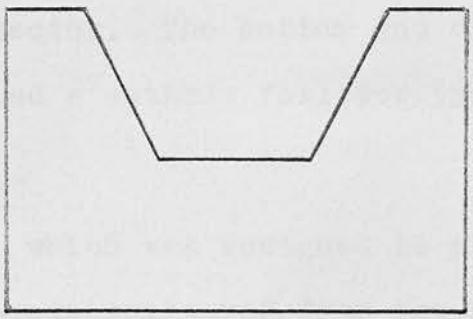

1cm
scale

FIG. 23

cathode follower type 1430A.

(b) The Υ-detector:-

The Υ-detector was a ½" x 1" NaI (Tl) crystal coupled by Dow Corning optical coupling compound to an EMI photomultiplier type 6097B. The crystal was fitted with an aluminium cap of thickness 400 mgm/cm.^{2} An extra aluminium plate of thickness 500 mgm/cm.^{2} was provided in front of the cap to make the total thickness of aluminium window equal to 900 mgm/cm.^{2} - sufficient to stop all electrons of up to 2 Mev. in energy. The crystal, the photomultiplier and a dynode resistor chain were mounted inside a 18 cm. long brass tube similar to the one used to enclose the β-detector. The bottom end of the tube in this case also carried a cathode follower type 1430A.

(c) The collimator:-

The collimator, which was designed to prevent the electrons and the Υ-rays scattered from the source and the sides of the brass tube from reaching the X-ray detector, was a 2 cm. thick brass disc with a trough shaped hole at its centre. The diameters of the two ends of the trough were 1.25 and 1.65 cm. respectively, the narrower end facing the β-detector. The brass disc was fixed inside a 4.7 cm. high brass tube 8.8 cm. in diameter, the same as that of the tubes used with the β- and Υ-detectors, and flanged at both ends. On the wider end of the collimator a slot was cut on the top face of the brass tube through

which the absorber plate (described in Section 5.3) could slide down along a supporting rail made of a pair of thin brass plates and screwed on to the collimator disc inside the tube. As shown in Fig. 22, when the absorber slide is in position, the absorber comes in front of the collimator hole.

The three parts of the detecting system were put together with the collimator in between and screwed to the flanges of the tubes containing the detectors. Black neoprene was used between the flanges to ensure that the collimator-detecting system was light tight. A piece of black camera-cloth was placed around the projecting portion of the absorber plate to prevent light entering through the slot. Keeping the β-detector downwards, the whole system was mounted vertically on a bracket fixed to the bench (see Fig. 21).

The vertical arrangement of the whole system enabled the absorber slide to go in horizontally, which minimised the chance of the absorber slipping in the recess and thereby altering the effective thickness presented to the X-ray beam. Making the collimator detachable from the detecting system facilitated the handling of the radioactive source in the plastic scintillator without disturbing the photomultiplier tube and thus ensuring the stability of the optical contact between the photomultiplier tube and the β-plastic. The optical contact of the crystals with the photomultiplier tubes in both channels was further secured by means of three screws sunk into holes bored on

the periphery of a perspex ring surrounding each crystal. The source positioning inside the plastic well provided nearly 4π geometry for the β-detector, and besides, it also ensured no appreciable loss of the high energy electrons. The β-plastic was arranged to be flush against the collimator which reduced the source to NaI(Tl) crystal distance to 4.2 cm. This gave maximum possible geometry for the X-ray detector necessary for high efficiency of the detecting system required in a coincidence experiment. The air path absorption of the K X-rays used in the experiment being negligible, no vacuum was needed in the detecting system.

5.2 Choice of Absorbers

It was pointed out in the last chapter that the relative intensity of the satellites associated with the 1720 keV E1 γ-ray of Pb^{206} can be estimated by measuring the intensity reduction of normal K X-rays and of the group of normal and satellite K X-rays for suitably chosen absorbers. The expression (4.28) for the intensity of the satellites guides the choice of suitable absorbers. From this expression it is obvious that in order to emphasise the presence of the satellites, it is desirable to choose an absorber which would give a higher intensity reduction for the group of normal and satellite K X-rays than for the normal K X-rays alone. This implies that the absorber chosen should be such that the more important components $K\alpha_1$ and $K\alpha_2$ of the K X-rays lie very close to, and at

least one of them on the lower energy side of the K-edge of the absorbers. When this is so, the satellites associated with at least one of these important component K X-rays could fall somewhere on the K-absorption edge, in which case a much higher mass absorption coefficient would be expected for the satellites than for the group of normal K X-rays giving the desired effect. The principal lines $K\alpha_1$ ($\lambda = 0.165$ Å) and $K\alpha_2$ ($\lambda = 0.170$ Å) of Pb^{206} (intensities in the ratio 100 : 55.3) are very close to the K-edges of osmium (K-edge = 0.167 Å) and iridium (K-edge = 0.162 Å) and at least one of these lines is on the low energy side of the K-edges. Also a calculation using Slater's method[111] shows that the mean wavelength of the KK and KL group of K X-ray satellites of lead should lie very close to the K-absorption edge of these absorbers. Thus, both osmium and iridium seemed to be suitable for the purpose of the present experiment.

5.3 Preparation of Absorbers

Two iridium sheets each 1 inch square and weighing 0.788 gm. and 1.018 gm. respectively were obtained from Johnson and Matthey Ltd. The first sheet was used as the thin iridium absorber and the two together as the thick iridium absorber, the geometrical thickness of the thin and thick absorbers from the above specifications being 0.122 gm./cm.^{2} and 0.28 gm./cm.^{2} respectively.

In the case of osmium, the metal being available in the form of thick granules which was not found to dissolve

or give a suspension in any volatile organic liquid, it was not possible to have an absorber of osmium metal alone. It was, however, found that a compound, ammonium chlorosmanate, $(NH_4)_2\ Os\ Cl_6$ available in the form of powder could be held in suspension in methyl alcohol and hence could be used satisfactorily. This compound obtained from Johnson and Matthey was stated to have a purity of not less than 99%.

The arrangement used for making a deposit of the osmium compound is shown in Fig. 24. Three pairs of aluminium plates were made with the upper plate 0.32 cm. thick and the lower plate .085 cm. thick, and each pair having coincident circular holes of diameter 1.95 cm. bored through them. Two of these were used to hold the absorbers and the third was used as a "no absorber" plate. The thickness of each pair was such that it could smoothly slide down along the supporting rail (F in Fig. 22) inside the brass tube to a position in which the hole was coaxial with the scintillators and the collimator. For the two absorber plates circular recesses of diameter 2.54 cms. and depth 1.5 and 2.95 mm, respectively, were made around the circular holes in the bottom plate of each pair. Thin mica discs of thickness .0038 gm./cm.^{2} were pressed down to the bottom of the recesses with a fine layer of seccotine. The bottom plate of one set was then placed over an aluminium base plate 10 x 5 x .65 cm. A stainless steel tube 3.2 cm. high, 2.7 cm. internal diameter and .35 mm wall thickness was placed over the recess with a

FIG 24. Arrangement for making Absorbers.

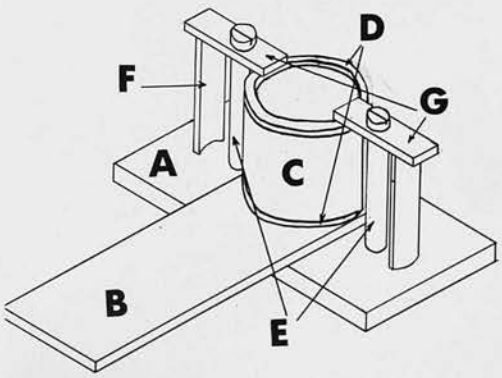

A - Base plate
B - Slide
C - Stainless Steel Tube
D - Rubber rings
E - Screw rods
F - Clamp Supports
G - Brass clamps

rubber ring beneath and another at the top of the tube, both 2.7 cm. in internal diameter. The tube was firmly clamped by two bars (GG) carrying screw rods (EE) and supported at one end on brass strips (FF) as shown in Fig. 24.

A suspension was then made of a weighed amount of ammonium chlorosmanate powder in methyl alcohol to which was added a few drops of collodion and this, after thorough stirring, was poured into the stainless steel tube. The whole arrangement was left undisturbed for about two days until the alcohol evaporated away and the deposit dried. No heating was applied since the deposit was found to crack under such treatment. The rubber ring between the plate and the tube was meant to stop any possible leakage of the liquid holding the powder in suspension, which might tend to give a thicker deposit around the edges of the recess than anywhere else. The few drops of collodion added to the suspension helped the absorber stick together and to the recess. A deposit on the bottom plate of the other set was made in a similar way using a different amount of the substance. The weights of the deposit on the two plates were 1.2777 gm. and 0.7330 gm. respectively, which corresponded to the thicknesses estimated to reduce the incident K X-ray beam intensity to about 0.45 and 0.65 of its original value respectively. The absorbers thus made were covered by similar mica discs (thickness = .0033 gm./cm.^{2}) to avoid any possible slipping, and then the thin aluminium plates were screwed on

to each of them. The third set of plates which was to be used as "no absorber" plate simply carried two mica discs to compensate for the mica discs used for holding the absorber deposits on the other two plates.

5.4 Uniformity Testing of the Absorbers

After having made the absorbers, their uniformity was tested. The system designed for this purpose is shown in Figs. 25 and 26. A flanged brass tube (MM) 5.5 cm. in height, 8.8 cm. in diameter and 3 mm wall thickness was fitted near the flanged end with a $\frac{1}{4}$" thick lead collimator H having a 1 mm hole at its centre. A brass bracket P fixed vertically to the flange carried a screw rod L. The lower end of the screw rod was designed to hold the absorber plate which hung loosely inside the brass tube through a slot S_1, made at the top, and was almost flush against the collimator. A small strip of brass cut into the shape of a segment and soldered to the screw rod T was screwed on to the lower end of the absorber plate. The screw rod T projected below the tube through another slot S_2 on it and carried a rubber pad and a brass tightening nut J. By turning the nut J it could be made to press the rubber pad against the brass tube and thus clamp the absorber plate in any desired position. The plate could be moved in a vertical plane to any position between the extremities of the lower slot S_2 by moving the screw rod T, and up or down by means of the screw rod L.

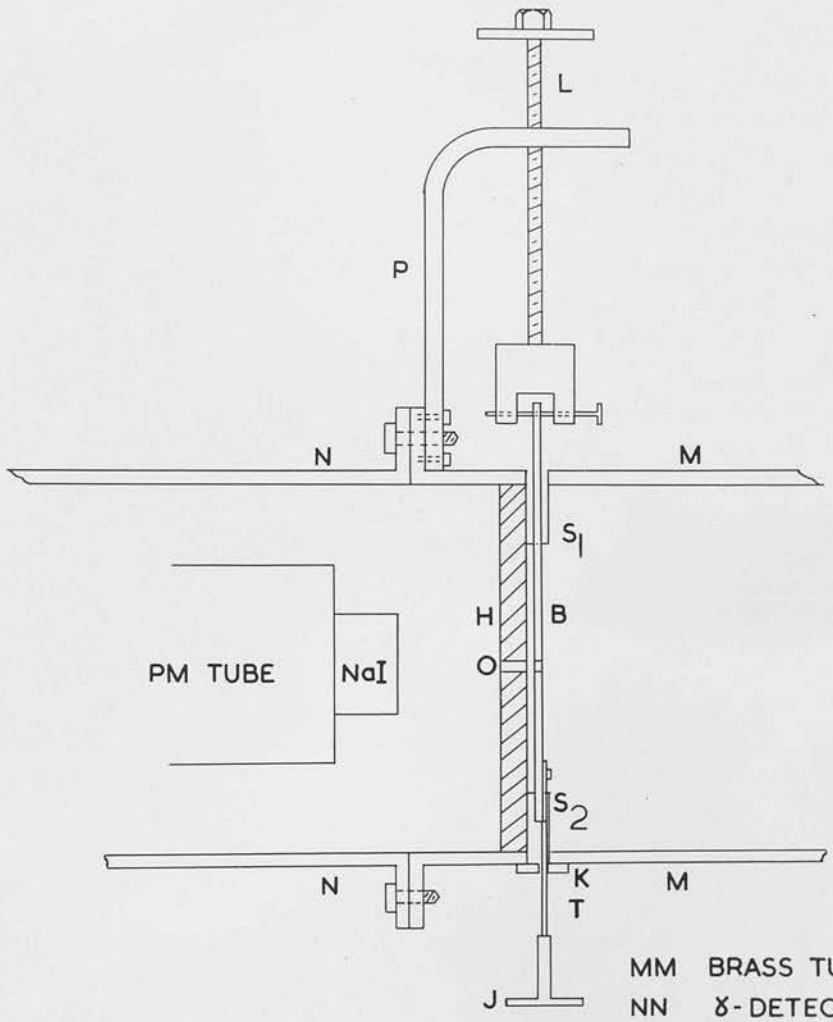

FIG. 25 UNIFORMITY TESTING SYSTEM (SIDE VIEW)

MM	BRASS TUBE
NN	δ-DETECTOR
H	LEAD COLLIMATOR
O	1mm HOLE
B	ABSORBER SLIDE
LT	SCREW RODS
K	RUBBER PAD
P	BRASS STAND
S_1 S_2	SLOTS FOR HOLDING ABSORBER PLATES
J	BRASS TIGHTENING NUT

FIG 26. Showing the END VIEW of the Uniformity Testing Device

B - Slide with absorbers

H - Lead Collinator with a 1mm hole

J - Brass tightening nut

L - Screw rod

K - Rubber pad

T - Screw rod

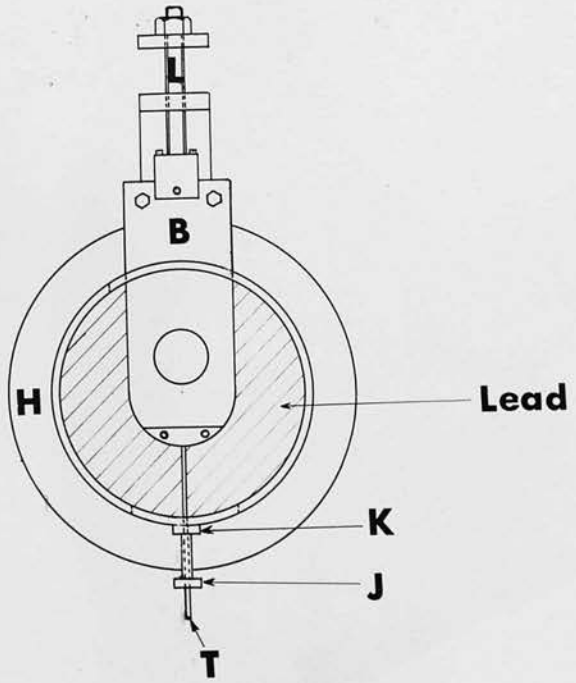

An Am^{241} source ($\sim$ 1 μC) mounted on a perspex disc 3.1 cm. in diameter and 0.5 cm. in thickness was held at a distance of 2 mm from the absorber plate, the disc being held vertically by three screws fixed to the periphery of the brass tube. The system was then screwed on to the brass tube enclosing the γ-detector which was kept horizontal for the present purpose. The γ-channel consisting of the detector, cathode follower, amplifier, pulse height analyser and scaler described in Section 5.5 was set on the 60 keV Am^{241} γ-ray peak with 5 volt channel width. With the geometry described above, it was possible to pick up the γ-rays transmitted through a region of about 1 mm. diameter on the absorber, and the controlling arrangements enabled traversals to be made along different arcs from top to bottom, thus selecting a host of such regions. Counts per minute were recorded for the various positions of the absorber plate and the results showed, within the statistical error (about 3%), that the deposits were uniform.

5.5 The Electronics

The block diagram of the electronics used in the experiment is shown in Fig. 27. In each channel, negative pulses were taken from the anode of the photomultiplier and fed through a cathode follower to an amplifier, a single channel pulse height analyser, a coincidence unit and scalers. For recording singles counts two scalers in series were used in each channel. The photomultipliers in the β- and γ-channels were run at 1400 and 1440 volts

BLOCK DIAGRAM OF THE ELECTRONICS

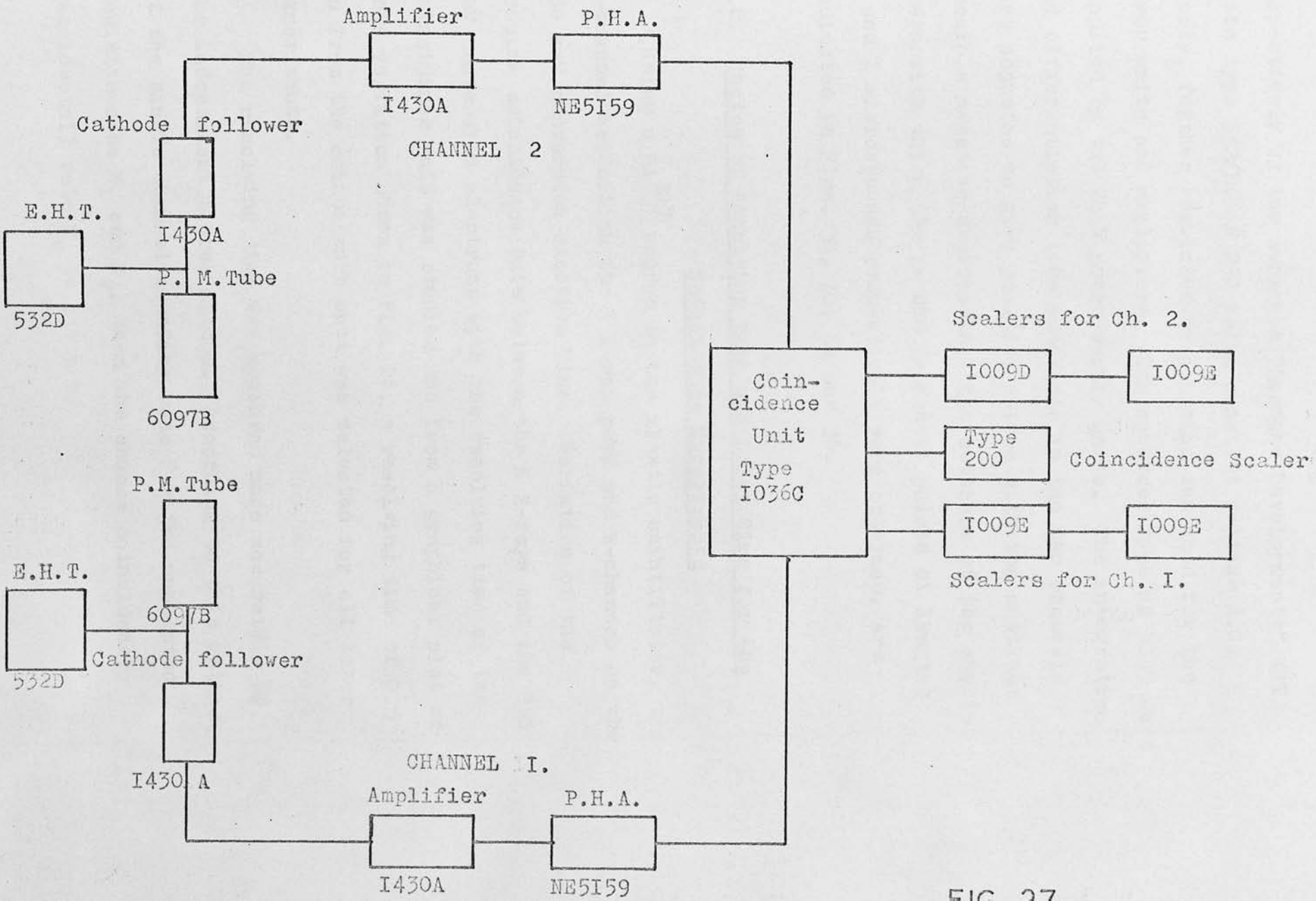

FIG. 27

respectively by two separate "Isotope Developments" EHT units type 532/D. A 230 volts constant voltage A.C. supply, further regulated by a variac, was used for the power units and amplifiers. The analyser type NE 5159 were supplied by two 24 V power supply units. The integration and differentiation time constants in the two channels were adjusted to give positive pulses with the smallest possible negative overshoots. The settings of the amplifiers, with which the γ- and β-channel pulses of lengths 5 and 1 microseconds respectively were obtained, are indicated in Figs. 30, 31, 34 and 38.

5.6. Choice of Resolving Time and Delay Time for the Coincidence Experiments

Using a Bi^{207} source in the plastic scintillator, the γ-channel was set on the K X-ray peak and β-channel on the 980 keV conversion electron line. Variation of the genuine coincidence rate between the K X-rays and the 980 keV conversion electrons with the resolving time of the coincidence unit was studied and from a graphical plot of this variation shown in Fig. 28, a resolving time of 0.5 μs from the coincidence unit was selected for all later experiments.

The resolving time was measured more accurately by the independent source method. According to this method, if the single channel counting rate for two unrelated radiations be N_1 and N_2, then the chance coincidence (accidental) rate N_c is given by

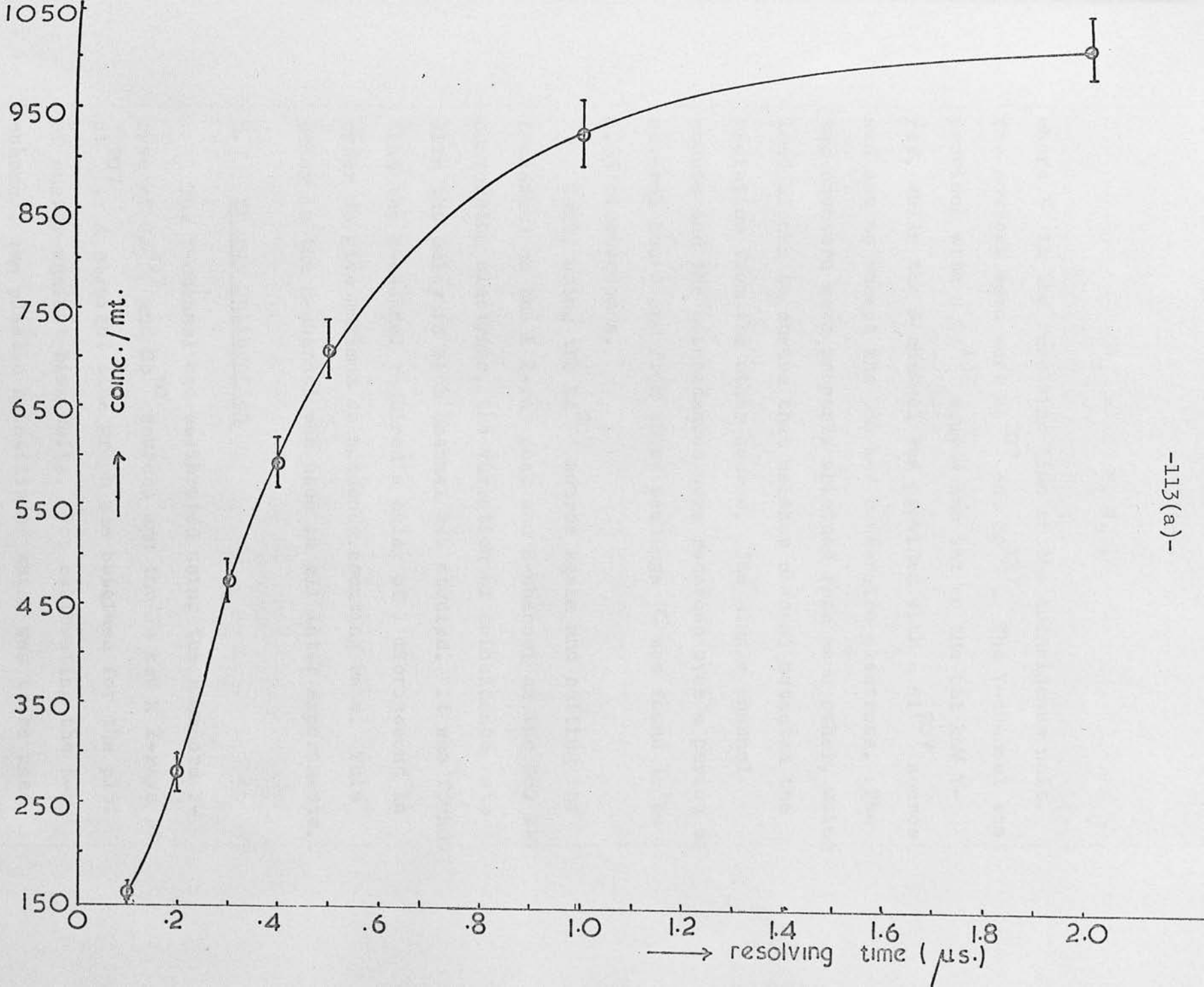
1050
950
850
750
650
550
450
350
250
150
coinc. / mt.
0
·2
·4
·6
·8
1·0
1·2
1·4
1·6
1·8
2·0
resolving time (μs.)

$$N_c = 2\tau N_1 N_2 ,$$

where τ is the resolving time of the coincidence unit. The sources used were Bi^{207} and Cs^{137}. The γ-channel was provided with a Cs^{137} source and set on the 661 keV γ-ray, while the β-channel was provided with a Bi^{207} source and set to accept the 980 keV conversion electrons. The two counters were properly shielded from each other, using lead blocks to ensure that neither channel detected the radiation from the other source. The single channel counts and the coincidences were recorded over a period of several hours and from these readings τ was found to be 0.53 microseconds.

Next, using the Bi^{207} source again and setting the γ-channel on the K X-ray peak and β-channel on the 980 keV conversion electrons, the variation of coincidence rate with the delay in each channel was studied. It was found that the β-channel required a delay of 1 microsecond in order to give maximum coincidence counting rate. This delay in the β-channel was used in all later experiments.

5.7 Energy Calibration

The γ-channel was calibrated using the standard γ-rays of Cs^{137} and Co^{60} sources and the 74 keV K X-rays of Bi^{207}. A straight line graph was obtained for the plot of energy against bias volts. For calibrating the β-channel, the plastic scintillator which was to be used later with the Bi^{206} source was coupled to the photomultiplier tube in the β-channel. The Bi^{207} source was transferred on to a slide which was introduced through the

slot on the collimator tube into the position intended to hold the absorber plate. From the Bi^{207} spectrum obtained with a narrow channel width, the peak positions (in volts) of the 480 and 980 keV conversion electrons were found. The plot of the peak positions against energy shown in Fig. 29 was later used to identify the various lines in the spectrum of Pb^{206} resulting from the decay of Bi^{206}.

5.8 Preparation and Mounting of Source

The radioactive source Bi^{206} obtained from the Radiochemical Centre, Amersham, was in the form of a liquid, Bismuth Chloride. The source was prepared, for use in the experiment, by putting a small drop of the Bismuth Chloride solution on to a disc of gold foil (5 mm. in diameter and 1.73 mgm./cm.^{2} thick) and evaporating to dryness. The foil was stuck centrally to the bottom of the trough in the plastic scintillator, using a thin layer of silicon vacuum grease. In order that the low energy conversion electrons were not suppressed by the gold foil, the active side of the foil was kept facing the crystal. The source strength at the beginning of the experiment, as estimated from the ratio of true to chance coincidence rates, was approximately 2.7 μC.

5.9 The γ- and β-Spectra

(a) The γ-spectra. Figs. 30 and 31 show the γ-spectra obtained with amplifier and discriminator settings shown. Apart from the K X-rays, the prominent γ-lines at

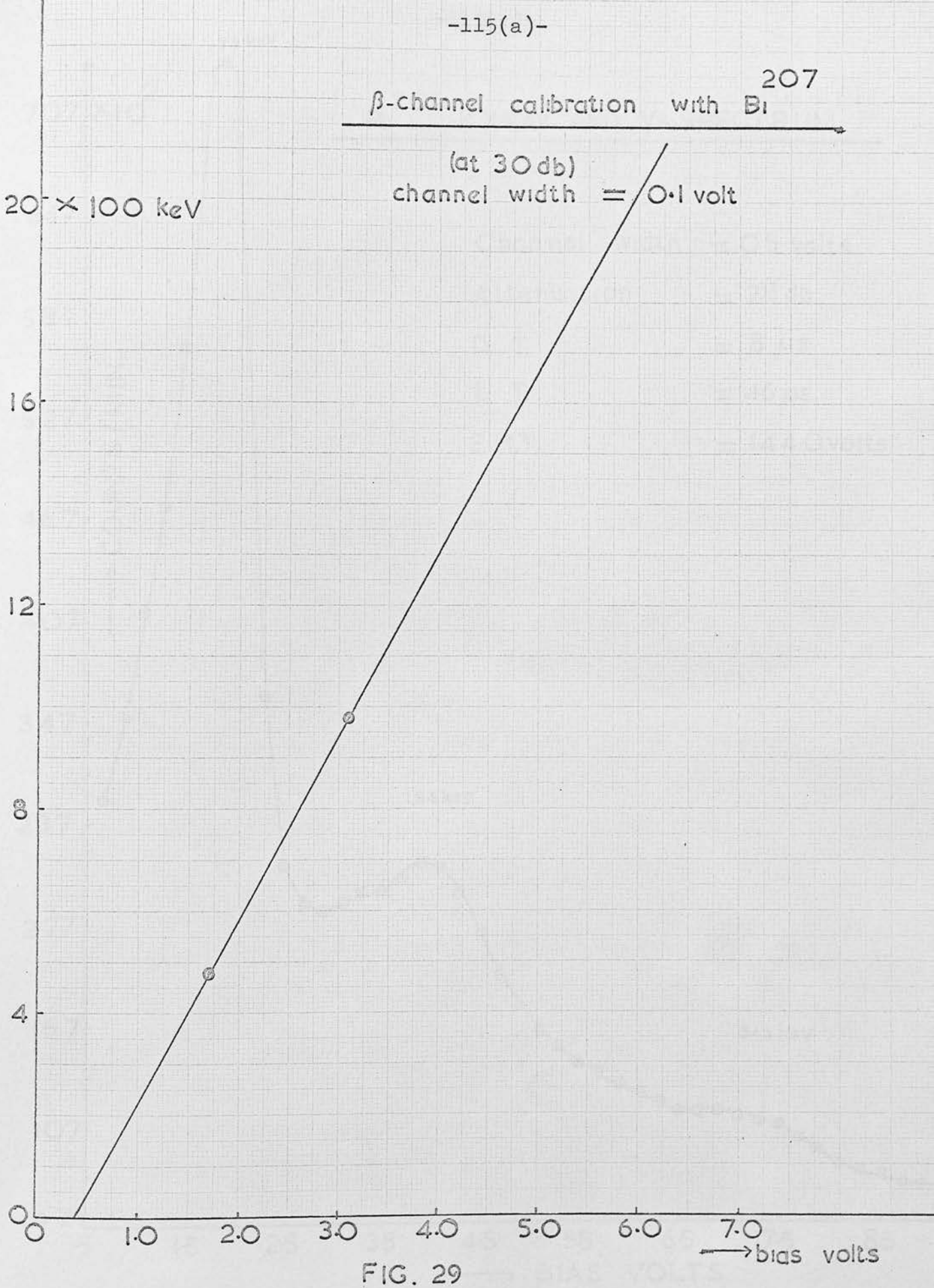
β-channel calibration with Bi^{207}
(at 30 db)
channel width = 0·1 volt
20 × 100 keV
16
12
8
4
0
0
1·0
2·0
3·0
4·0
5·0
6·0
7·0
bias volts

FIG. 29

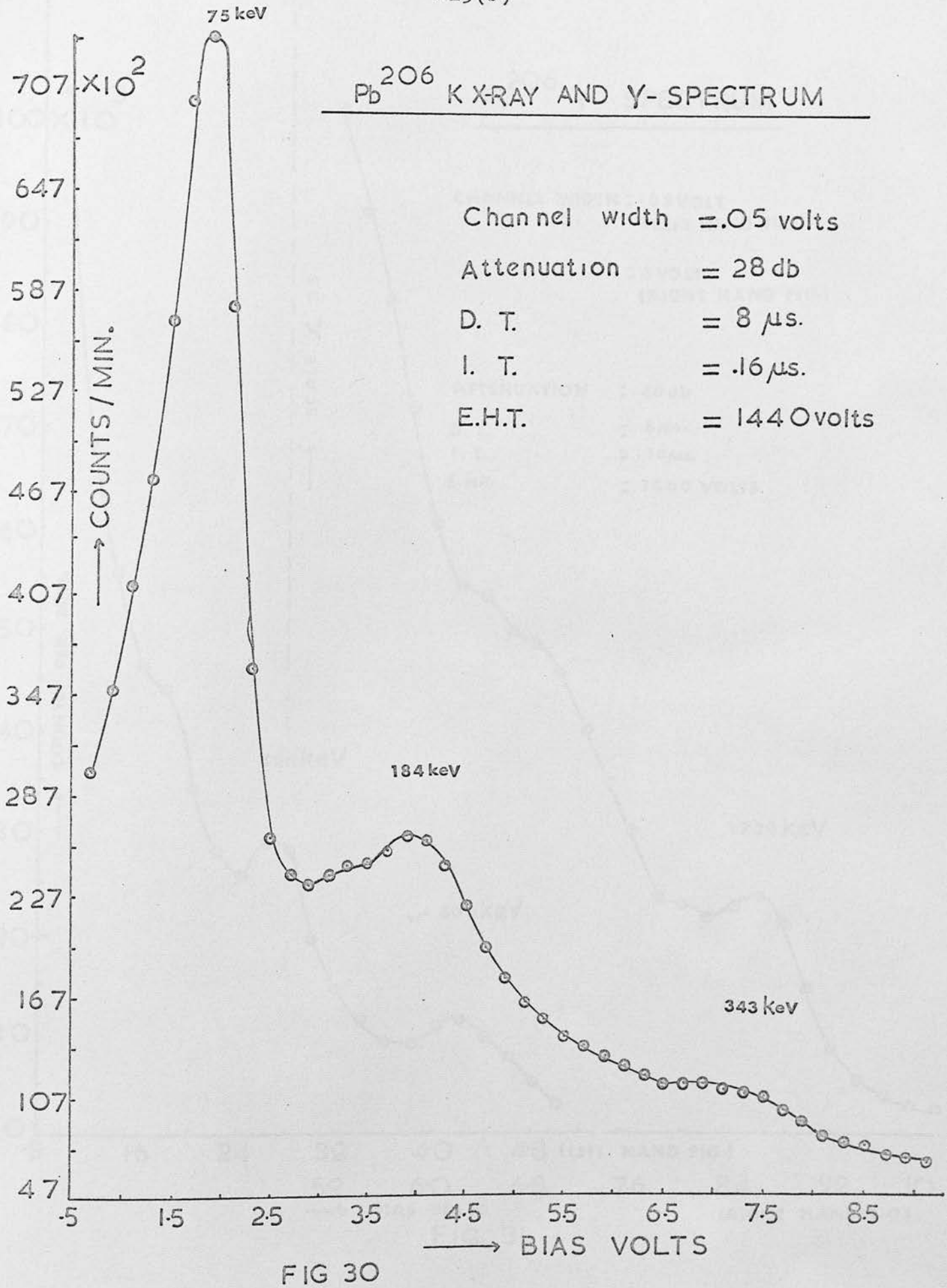

Pb^{206} K X-RAY AND γ- SPECTRUM

Channel width = .05 volts
Attenuation = 28 db
D. T. = 8 μs.
I. T. = .16 μs.
E.H.T. = 1440 volts

FIG 30

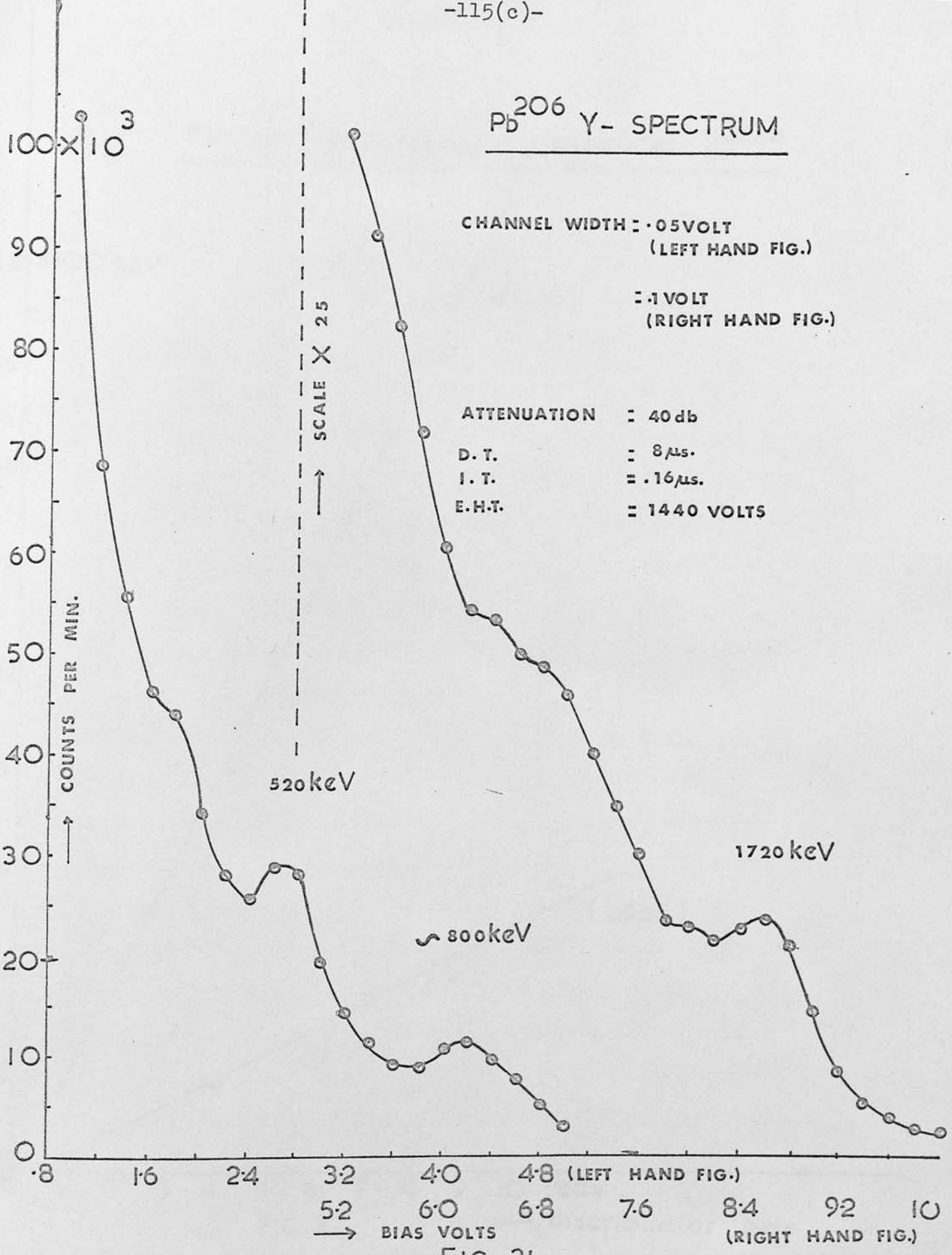
Pb206 γ- SPECTRUM
CHANNEL WIDTH : ·05VOLT
(LEFT HAND FIG.)
: ·1 VOLT
(RIGHT HAND FIG.)
ATTENUATION : 40 db
D. T. : 8 μs.
I. T. : .16 μs.
E.H.T. : 1440 VOLTS
SCALE X 25
100 X 10³
90
80
70
60
50
40
30
20
10
0
COUNTS PER MIN.
520keV
800keV
1720keV
·8
1·6
2·4
3·2
4·0
4·8
(LEFT HAND FIG.)
5·2
6·0
6·8
7·6
8·4
9·2
10
BIAS VOLTS
(RIGHT HAND FIG.)

FIG. 31

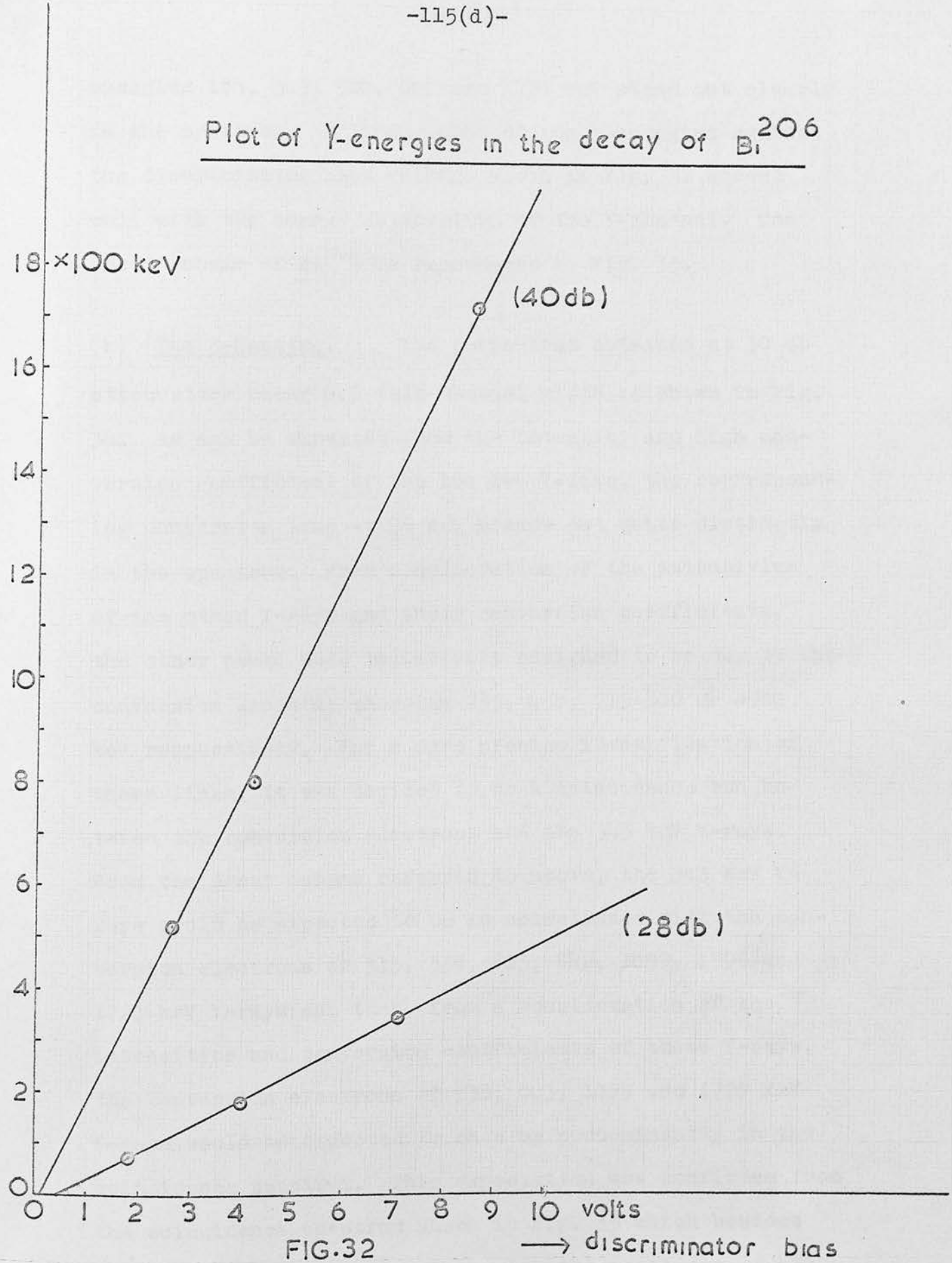
Plot of γ-energies in the decay of Bi^{206}
18 ×100 keV
16
14
12
10
8
6
4
2
0
(40db)
(28db)
0 1 2 3 4 5 6 7 8 9 10 volts
⟶ discriminator bias

FIG.32

energies 184, 343, 520, 800 and 1720 keV stand out clearly in the spectrum. A linear plot of the γ-energies against the discriminator bias voltage shown in Fig. 32 agreed well with the energy calibration of the γ-channel. The decay scheme of Bi^{206} is reproduced in Fig. 33.

(b) The β-Spectra. The β-spectrum obtained at 30 db attenuation using 0.1 volt channel width is shown in Fig. 34. As may be expected from the intensity and high conversion coefficient of the 184 keV γ-line, the corresponding conversion line at 96 keV stands out quite distinctly in the spectrum. From consideration of the intensities of the other γ-rays and their conversion coefficients, the other peaks were tentatively assigned to be due to the conversion lines at energies 255, 430, 715-800 & ~900 keV respectively. For a more precise identification of these lines, it was decided to do a coincidence run between the conversion electrons and the 343 keV γ-rays. From the decay scheme referred to above, the 343 keV γ-rays could be expected to be in coincidence with the conversion electrons of 313, 538, 803, 842, 1099, 1596 and 1720 keV γ-rays and then, from a consideration of the intensities and conversion coefficients of these γ-rays, the conversion electrons of 538, 803, 1099 and 1720 keV γ-rays would be expected to show up predominantly in the coincidence spectrum. This expectation was confirmed from the coincidence spectrum shown in Fig. 35 which besides showing a reasonable agreement with the positions of 430,

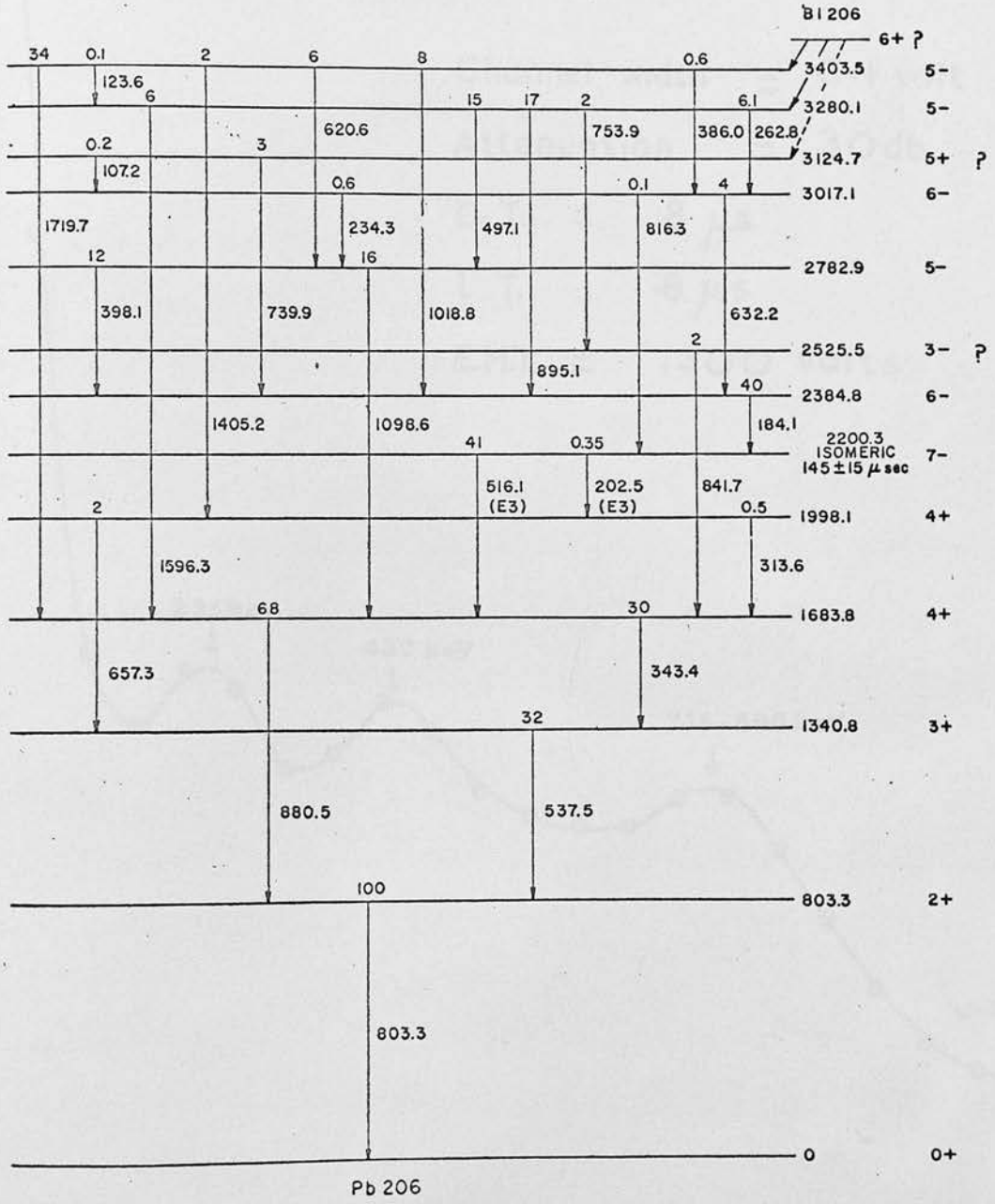

Fig. 33

Decay Scheme of Bi^{206} (Ref. 118).

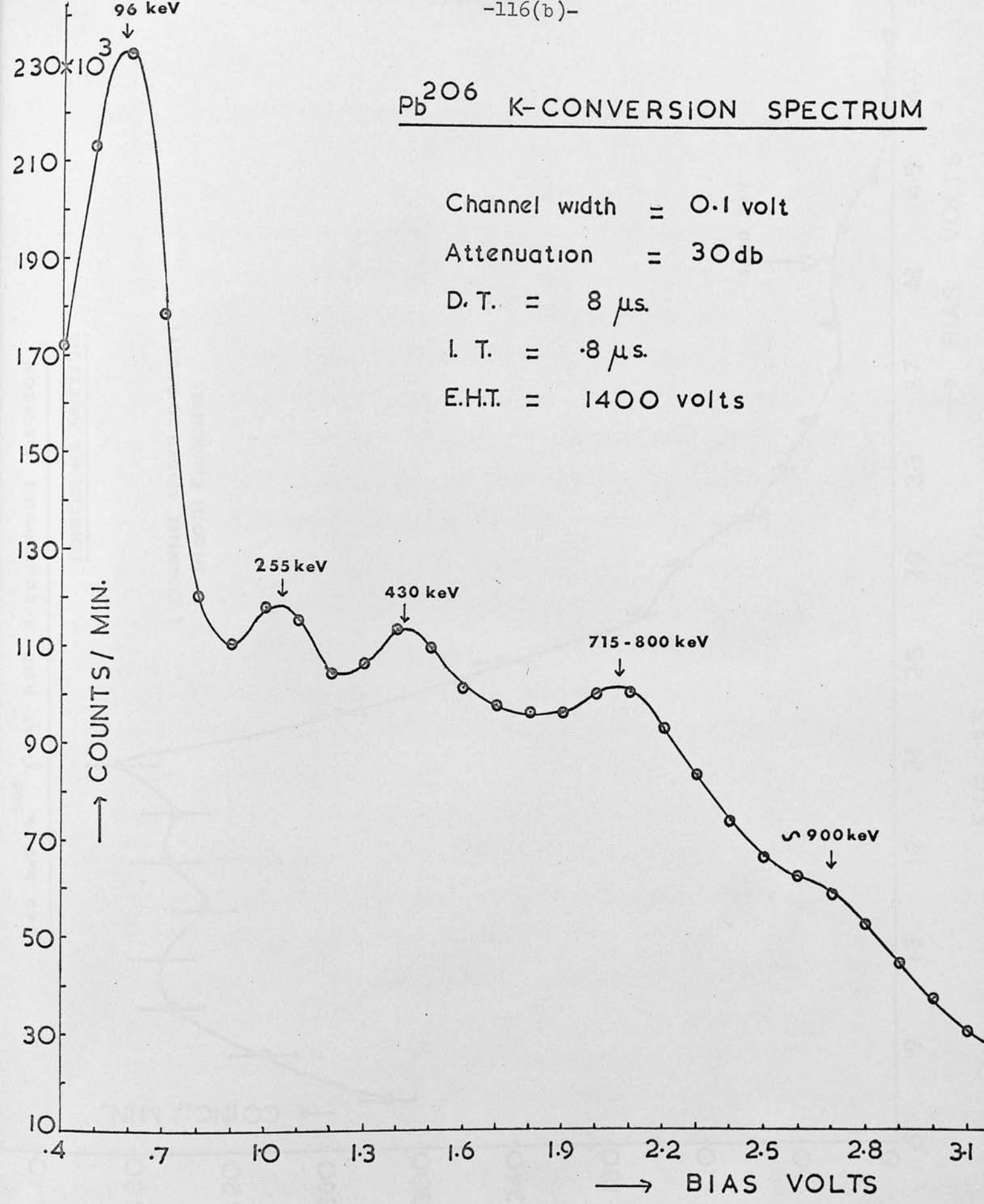
Pb206 K-CONVERSION SPECTRUM
Channel width = 0.1 volt
Attenuation = 30db
D. T. = 8 μs.
I. T. = ·8 μs.
E.H.T. = 1400 volts
96 keV
255 keV
430 keV
715 - 800 keV
~900 keV
230×10³
210
190
170
150
130
110
90
70
50
30
10
→ COUNTS / MIN.
·4
·7
1·0
1·3
1·6
1·9
2·2
2·5
2·8
3·1
→ BIAS VOLTS

FIG. 34

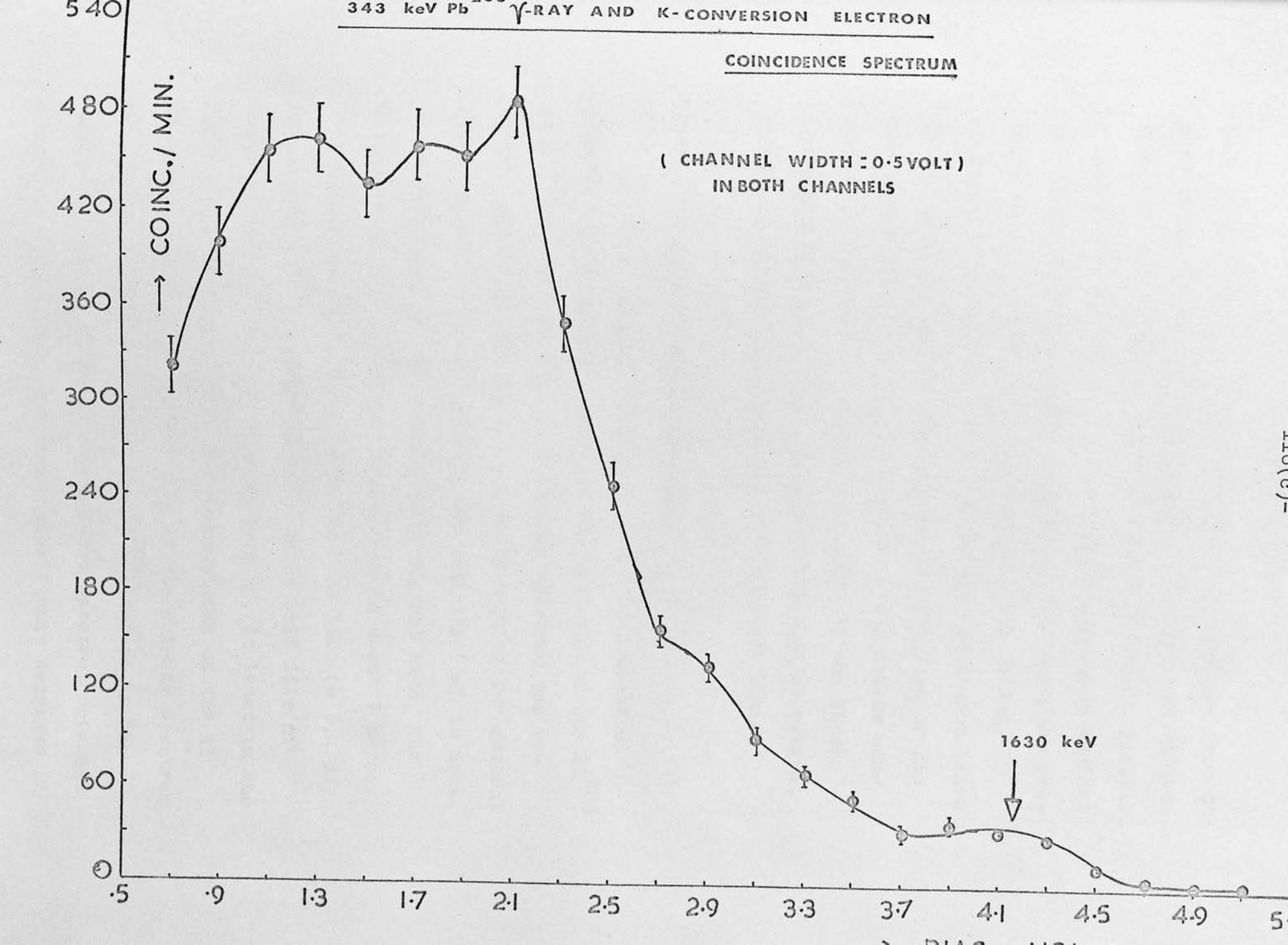
343 keV Pb γ-RAY AND K-CONVERSION ELECTRON
COINCIDENCE SPECTRUM
(CHANNEL WIDTH : 0·5 VOLT)
IN BOTH CHANNELS
→ COINC./ MIN.
540
480
420
360
300
240
180
120
60
0
·5
·9
1·3
1·7
2·1
2·5
2·9
3·3
3·7
4·1
4·5
4·9
1630 keV

715, and ~ 900 keV conversion electrons, obtained from the β-spectrum of Fig. 34, also predicts the position of the 1630 keV conversion line of the 1720 keV γ-rays. Finally, a linear plot of the conversion electron energies against the discriminator voltage which agreed well with the predictions of the β-channel calibration graph of Fig. 29 confirmed that the identification of the conversion lines in the spectrum was reasonably correct. Because of the poor resolution of the plastic phosphor the weaker conversion lines were not resolved and most of the lines identified might, in fact, be a superposition of several weaker lines along with the assigned stronger lines.

5.10 Purity of the Bi^{206} Source

The Bi^{206} source obtained from the Radiochemical Centre, Amersham, was tested for the presence of any Bi^{205} or Bi^{207} as an impurity. The K X-ray spectrum was recorded under the same conditions every morning for several days. From a graphical plot of the activity ($\propto$ to area under the peak) on logarithmic scale against time, the half life of the source was obtained to be about 7 days. This agrees reasonably well with the half life (= 6.4 days) for a pure Bi^{206} source. As Bi^{205} has a half life of about 15 days, it did not seem to show up, at least in the first few days during which the observations on the E1 line were recorded. The recording of the K X-ray spectrum was, however, continued until the Bi^{206} isotope in the source had almost decayed. The K X-ray spectrum obtained after 9-10 weeks did not show any significant decrease in

the total counts under the peak. A comparison of the γ-spectrum with the Bi^{207} spectrum taken during the preliminary runs suggested the presence of some Bi^{207} in the source. By comparing the area under the X-ray peak due to the residual source with that due to the fresh source, it was found that the original source contained about 0.7% Bi^{207} as impurity. This being very small, no correction was considered necessary on this account.

5.11 The Method of Observation

The single channel spectrum of Pb^{206} K X-rays shown in Fig. 36 was obtained, using a large channel width (0.5 volt) which was required for a high coincidence rate, apart from ensuring that all the component K X-rays were present in the X-ray photopeak. From this spectrum the resolution of the NaI detector for the Pb^{206} K X-rays was estimated to be about 30%. Due to the large Compton background and very small conversion coefficient of the high energy ($\sim$ 1 Mev) Pb^{206} γ-rays, it was very difficult to obtain a single channel spectrum of the conversion electrons in the range 1000-1700 keV. Consequently the spectrum of the 1630 keV conversion electron line corresponding to the 1720 keV E1 γ-ray was obtained by observations on β-K X-ray coincidences which are shown in Fig. 37.

The γ-channel was then set on the K_{α} X-ray peak and the β-channel on the 1630 keV conversion line using a large channel width (0.5 volt) in the β-channel to ensure that all the 1630 keV K-conversion electrons in the peak

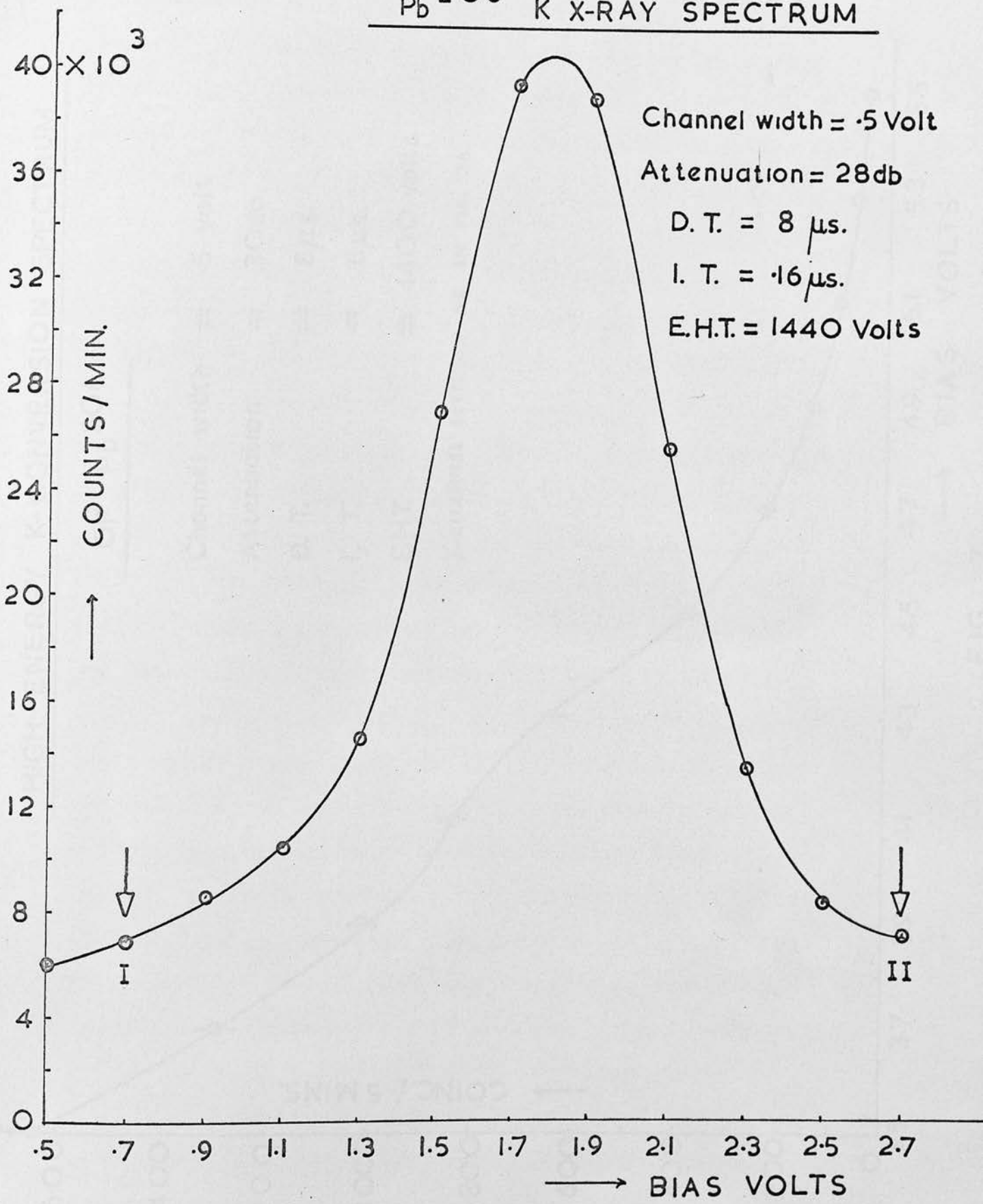
Pb 206 K X-RAY SPECTRUM
40 X 10 3
36
32
28
24
20
16
12
8
4
0
COUNTS / MIN.
Channel width = ·5 Volt
Attenuation = 28db
D. T. = 8 µs.
I. T. = ·16 µs.
E.H.T. = 1440 Volts
I
II
·5
·7
·9
1.1
1.3
1.5
1.7
1.9
2·1
2·3
2·5
2·7
BIAS VOLTS

FIG. 36

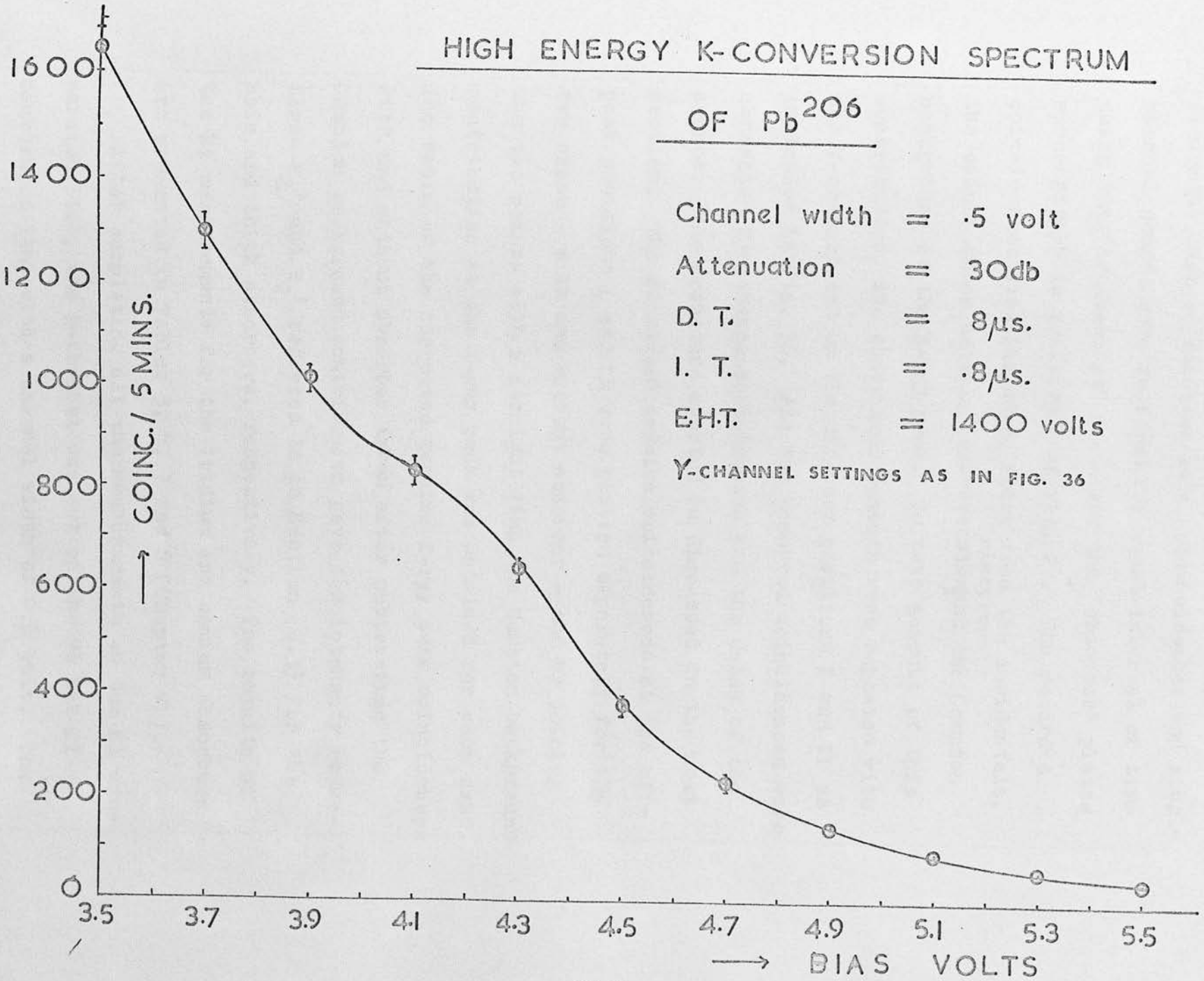
HIGH ENERGY K-CONVERSION SPECTRUM
OF Pb^{206}
Channel width = .5 volt
Attenuation = 30db
D. T. = 8μs.
I. T. = .8μs.
E.H.T. = 1400 volts
Y-CHANNEL SETTINGS AS IN FIG. 36
→ COINC./ 5MINS.
0
200
400
600
800
1000
1200
1400
1600
3.5
3.7
3.9
4.1
4.3
4.5
4.7
4.9
5.1
5.3
5.5
→ BIAS VOLTS

FIG. 37

were being counted. This was necessary to give a sufficiently high coincidence rate. Coincidences and single channel counts were recorded for equal interval of time using the "no absorber" plate and the "absorber" plates successively in position F of Fig. 22. The recorded coincidences also included, apart from the accidentals, the coincidences between the conversion electrons and the Compton background at the X-ray peak. To take account of this contribution, the above measurements were repeated with the γ-channel set on the off-peak positions I and II as indicated in Fig. 36. All the observed coincidences were corrected for chance coincidences and the decay of the source. The procedure adopted is discussed in the next section. The corrected genuine coincidences at the off-peak positions I and II were plotted separately for the two cases - with and without absorber - and by joining the two points with a straight line the Compton background contribution at the X-ray peak was obtained for each case. The ratio of the corrected genuine X-ray peak coincidences with and without absorber taken after subtracting the Compton background contribution gave the intensity reductions R_1' and R_2' referred to in Section (4.3) for the thin and thick absorbers, respectively. The results of the E1 measurements for the iridium and osmium absorbers are presented in Tables 3, 4, 7 and 8 (Chapter VI).

After completing all the measurements on the E1 conversion line, the β-channel was set on the 96 keV M1 conversion line with a channel width of 0.4 volt. The

single channel β-spectrum at 18 db amplifier setting at which this line was obtained is shown in Fig. 38. All measurements made on the E1 line were repeated with this M1 line and the values of R_1 and R_2 obtained. The results of M1 measurements for the absorbers are shown in Tables 5, 6, 9 and 10 (Chapter VI).

The counting times used in the various runs of E1 measurements varied from 30 minutes to 2 hours, but for M1 measurements, the coincidence rate being quite high, counts were recorded for 10-15 minute intervals only. Longer counting times were avoided to minimise the effect of gain drifts. Temperature variation seemed to be the main cause of gain drift in both channels and hence every effort was made to keep the laboratory temperature constant during a set of observations. Besides, a gradual decrease of pulse height was observed in both channels - mainly in the γ-channel - over a longer period of time which, perhaps, was due to the slow deterioration of the optical contact of the crystals, in spite of the precautions already described in Section (5.1). The peak positions in the two channels were, therefore, checked each time before starting a new set of observations and the discriminator-bias reset accordingly, if necessary.

5.12 Correction for the Chance Coincidences and Decay of the Source

The number of chance coincidences from a decaying source in a given time can be calculated as follows:-

Let N_o = number of atoms present in the source at time $t = 0$,

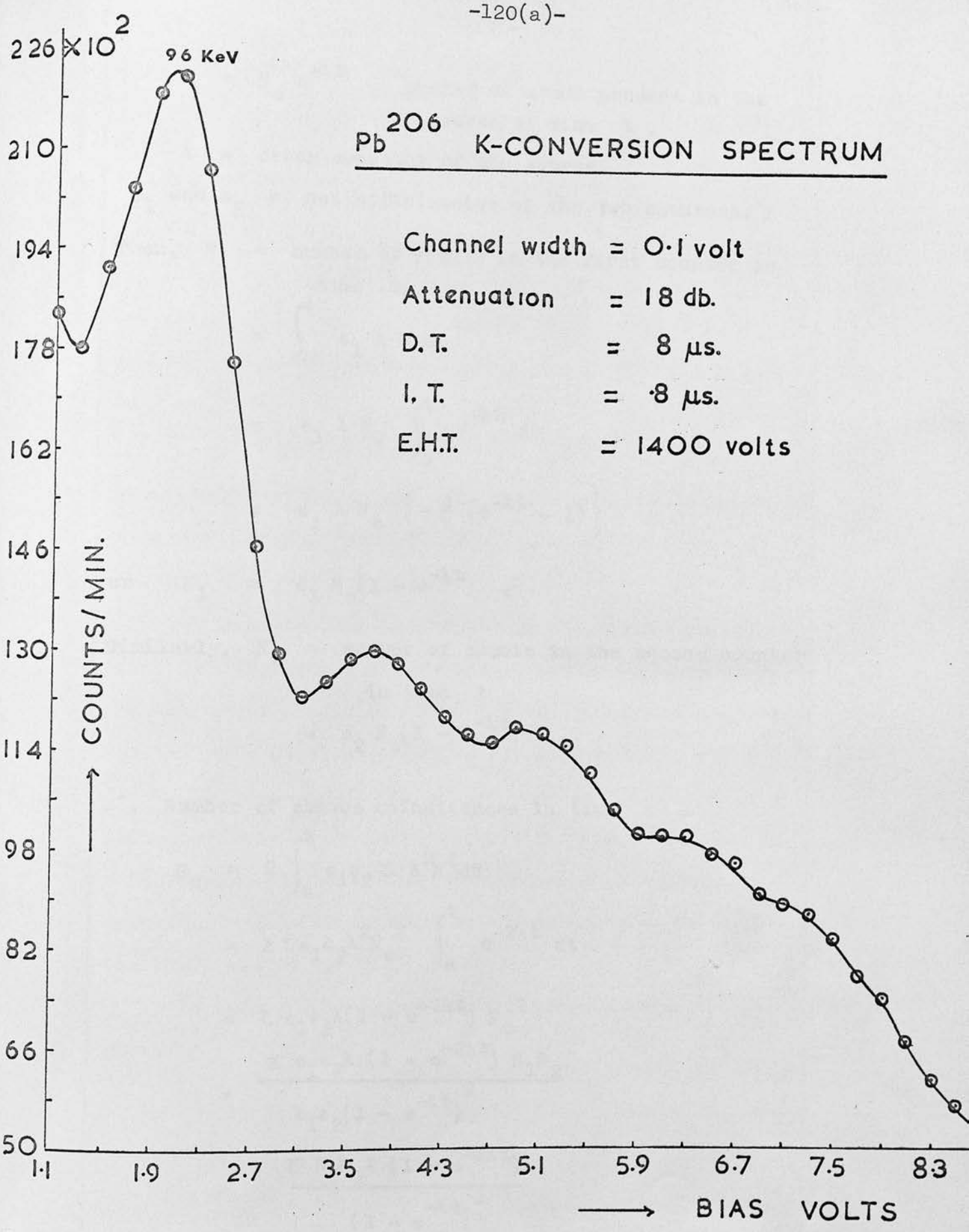

Pb^{206} K-CONVERSION SPECTRUM

Channel width = 0·1 volt
Attenuation = 18 db.
D. T. = 8 μs.
I. T. = ·8 μs.
E.H.T. = 1400 volts

FIG. 38

$N = N_o e^{-\lambda t}$ = number of atoms present in the source at time t.

λ = decay constant of the source.

ε_1 and ε_2 = net efficiencies of the two counters.

Then, N_1 = number of counts in the first counter in time t,

$$= \int_o^t \varepsilon_1 \lambda N \, dt$$

$$= \varepsilon_1 \lambda N_o \int_o^t e^{-\lambda t} \, dt$$

$$= \varepsilon_1 \lambda N_o \left\{ -\frac{1}{\lambda} (e^{-\lambda t} - 1) \right\}$$

or $N_1 = \varepsilon_1 N_o (1 - e^{-\lambda t})$.

Similarly, N_2 = number of counts in the second counter in time t

$$= \varepsilon_2 N_o (1 - e^{-\lambda t})$$

∴ Number of chance coincidences in time t =

$$N_c = 2 \int_o^t \varepsilon_1 \varepsilon_2 \tau \lambda^2 N^2 dt$$

$$= 2 \tau \varepsilon_1 \varepsilon_2 \lambda^2 N_o^2 \int_o^t e^{-2\lambda t} \, dt$$

$$= \tau \varepsilon_1 \varepsilon_2 \lambda (1 - e^{-2\lambda t}) N_o^2$$

$$= \frac{\tau \varepsilon_1 \varepsilon_2 \lambda (1 - e^{-2\lambda t}) N_1 N_2}{\varepsilon_1 \varepsilon_2 (1 - e^{-\lambda t})^2}$$

$$= \frac{\tau N_1 N_2 \lambda (1 - e^{-2\lambda t})}{(1 - e^{-\lambda t})^2}$$

$$= \frac{\tau N_1 N_2 \lambda (1 + e^{-\lambda t})}{(1 - e^{-\lambda t})} \qquad (5.1)$$

If λt be very small, this approximates to

$$N_c = \frac{\tau N_1 N_2 2\lambda^2 t}{\lambda^2 t^2}$$

$$\text{or} \quad N_c = 2N_1 N_2 (\frac{\tau}{t}) \qquad (5.2)$$

(τ is expressed as a fraction of the counting time t).

In calculating the accidentals, expression (5.2) was used when the counting time was short, and expression (5.1) was used for longer counting times.

After correction had been made for chance coincidences, the resulting number of genuine coincidences were corrected for the decay of the source. Obviously, such a correction must be made after subtracting the accidentals, and not before, because the total coincidence rate is made up of two parts which vary differently with time. The chance coincidence rate varies as $e^{-2\lambda t}$, whereas the genuine coincidence rate is a function of source strength only and therefore varies as $e^{-\lambda t}$.

The number of genuine coincidences in time t is given by

$$N_G = \int_o^t \varepsilon_1 \varepsilon_2 N \lambda \, dt$$

$$= \varepsilon_1 \varepsilon_2 N_o (1 - e^{-\lambda t})$$

$$= \varepsilon_1 \varepsilon_2 N_o \lambda \frac{(1 - e^{-\lambda t})}{\lambda}$$

$$= N_i \frac{(1 - e^{-\lambda t})}{\lambda}$$

where $N_i = \varepsilon_1 \varepsilon_2 N_o \lambda$

= initial rate of coincidences.

$$\therefore N_G = \frac{N_i(\lambda t - \frac{\lambda^2 t^2}{2!} + \frac{\lambda^3 t^3}{3!} - ....)}{\lambda}$$

$$= N_i\, t(1 - \frac{\lambda t}{2} + \frac{\lambda^2 t^2}{6} - .....)$$

$$= N_G{}^o(1 - \frac{\lambda t}{2} + \frac{\lambda^2 t^2}{6} - .....)$$

where $N_G{}^o$ = number of genuine coincidences observed in time t.

If λt be very small, then

$$N_G = N_G{}^o(1 - \frac{\lambda t}{2}) \quad ..... \qquad (5.3)$$

Expression (5.3) can be used to calculate the number of genuine coincidences for a decaying source. But since, under the conditions of the present experiment, either of the single channel counting rates varies as $e^{-\lambda t}$, the decay correction can be made by normalising the genuine coincidences using the ratios of the singles counts. For the purpose of normalisation the β-counts were used because this channel was not affected by the change of "absorber" and "no absorber" plates. The method adopted for applying normalisation was to multiply the number of genuine coincidences in any particular run of a set of observations by the ratio of the corresponding β-singles count to the first β-singles count of that set. This procedure of normalisation, besides correcting the coincidences for the

decay of the source, also served to correct for any incidental changes in the β-counting rate. No correction for the background in the absence of the radioactive source was considered necessary because it was very small and negligible in comparison with the observed counting rates in presence of the source.

Table 3

Coincidence Measurement for El Transition

(Thin iridium)

Time Interval	X-ray peak + background coincidences (Corrected)		Average background coincidences (Corrected)		Corrected K X-ray conversion electron coincidences		Intensity Reduction $R_1' = N/N_o$
	with abs.	without abs.	with abs.	without abs.	with abs. (N)	without abs. (N_o)	
1 hr.	4375	5942	635	700	3740	5242	0.713
40 mins.	2803	3869	420	460	2383	3409	0.699
"	2647	3619	395	425	2252	3194	0.705
"	2620	3561	390	420	2230	3141	0.710
30 mins.	2426	3344	430	492	1996	2852	0.700
"	2353	3275	430	475	1923	2800	0.687
1 hr.	4685	6435	813	903	3872	5532	0.700
"	4284	5976	760	854	3524	5122	0.688
30 mins.	2042	2935	355	439	1687	2496	0.676

mean $R_1' = 0.698 \pm .004$.

TABLE 4

Coincidence Measurement for E1 Transition
(Thick iridium)

Time Interval	X-ray peak + background coincidences (Corrected)		Average background coincidences (Corrected)		Corrected K X-ray conversion electron coincidences		Intensity Reduction $R_2' = N/N_o$
	with abs.	without abs.	with abs.	without abs.	with abs. (N)	without abs. (N_o)	
40 mins.	2068	4166	350	510	1718	3656	0.470
"	2003	4054	370	505	1633	3549	0.460
30 mins.	1741	3412	380	440	1361	2972	0.458
"	1719	3315	340	385	1379	2930	0.471
"	1648	3332	330	410	1318	2922	0.451
"	1590	2966	353	422	1237	2544	0.486
"	1550	2964	355	438	1195	2526	0.473
1 hr.	2901	5363	673	769	2228	4594	0.485
"	2701	5137	635	722	2066	4415	0.468

mean $R_2' = 0.469 \pm .004$.

Table 5

Coincidence Measurement for M1 Transition
(Thin iridium)

Time Interval	X-ray peak + background coincidences (Corrected)		Average background coincidences (Corrected)		Corrected K X-ray conversion electron coincidences		Intensity Reduction $R_1 = N/N_o$
	with abs.	without abs.	with abs.	without abs.	with abs. (N)	without abs. (N_o)	
10 mins.	3868	5339	475	525	3393	4814	0.705
"	3919	5287	435	540	3484	4747	0.734
"	2440	3236	392	465	2048	2771	0.739
"	2349	3163	369	444	1980	2719	0.728
"	2166	2977	350	428	1816	2549	0.712
"	2205	2936	362	424	1843	2512	0.734
"	2158	2933	346	418	1812	2515	0.720

mean $R_1 = 0.724 \pm .005$.

Table 6

Coincidence Measurement for M1 Transition

(Thick iridium)

Time Interval	X-ray peak + background coincidences (Corrected)		Average background coincidences (Corrected)		Corrected K X-ray conversion electron coincidences		Intensity Reduction $R_2 = N/N_o$
	with abs.	without abs.	with abs.	without abs.	with abs. (N)	without abs. (N_o)	
10 mins.	3628	6945	485	720	3143	6225	0.505
"	3539	6968	465	702	3064	6266	0.489
"	3484	6747	501	714	2983	6033	0.494
"	3356	6371	466	725	2890	5646	0.512
"	3333	6339	458	684	2875	5655	0.508
"	3115	5969	470	657	2645	5312	0.498
"	3017	5540	470	634	2547	4906	0.519

mean $R_2 = 0.503 \pm .004$.

Table 7

Coincidence Measurement for E1 Transition
(Thin osmium)

Time Interval	X-ray peak + background coincidences (Corrected)		Average background coincidences (Corrected)		Corrected K X-ray conversion electron coincidences		Intensity Reduction $R_1' = N/N_o$
	with abs.	without abs.	with abs.	without abs.	with abs. (N)	without abs. (N_o)	
1 hr.	2226	3100	345	365	1881	2735	0.688
"	1930	2710	335	360	1595	2350	0.679
"	1833	2626	280	315	1553	2311	0.672
2 hrs.	3033	4342	570	640	2463	3702	0.665
"	2218	3114	400	425	1818	2689	0.676
"	1832	2524	335	350	1497	2174	0.688
30 mins.	5762	7956	1110	1185	4652	6771	0.687
"	4832	6858	900	950	3932	5908	0.665
1 hr.	9279	13013	1700	1780	7579	11233	0.675
"	8370	11693	1470	1620	6900	10073	0.685

mean $R_1' = 0.678 \pm .003$

Table 8

Coincidence Measurement for E1 Transition

(Thick osmium)

Time Interval	X-ray peak + background coincidences (Corrected)		Average background coincidences (Corrected)		Corrected K X-ray conversion electron coincidences		Intensity Reduction $R_2' = N/N_o$
	with abs.	without abs.	with abs.	without abs.	with abs. (N)	without abs. (N_o)	
40 mins.	1717	3171	335	350	1382	2821	0.490
"	1418	2691	333	395	1085	2296	0.483
50 mins.	1731	3092	350	365	1381	2727	0.506
1 hr.	2040	3718	415	445	1625	3273	0.496
"	2012	3676	412	440	1600	3236	0.494
"	6301	11311	1460	1550	4841	9761	0.504
30 mins.	3116	5500	681	743	2435	4757	0.512
"	2728	4904	620	710	2108	4194	0.503
"	2676	4749	540	594	2136	4155	0.514
1 hr.	4831	8661	1020	1100	3811	7561	0.504

mean $R_2' = 0.501 \pm 0.004$.

Table 9

Coincidence Measurement for M1 Transition
(Thin osmium)

Time Interval	X-ray peak + background coincidences (Corrected)		Average background coincidences (Corrected)		Corrected K X-ray conversion electron coincidences		Intensity Reduction $R_1 = N/N_o$
	with abs.	without abs.	with abs.	without abs.	with abs. (N)	without abs. (N_o)	
15 mins.	1432	1990	208	245	1224	1745	0.701
"	1302	1855	207	234	1095	1621	0.676
"	1258	1718	199	221	1059	1497	0.707
10 mins.	3320	4691	566	649	2754	4042	0.681
"	3283	4582	556	635	2727	3947	0.691
"	3211	4447	552	630	2659	3817	0.697
"	3030	4163	530	602	2500	3561	0.702
"	2853	3977	490	549	2363	3428	0.689

mean $R_1 = 0.693 \pm .004$.

Table 10

Coincidence Measurements for M1 Transition
(Thick osmium)

Time Interval	X-ray peak + background coincidences (Corrected)		Average background coincidences (Corrected)		Corrected K X-ray conversion electron coincidences		Intensity Reduction $R_2 = N/N_o$
	with abs.	without abs.	with abs.	without abs.	with abs. (N)	without abs. (N_o)	
10 mins.	867	1530	167	230	700	1300	0.538
15 mins.	1205	2152	210	250	995	1902	0.523
10 mins.	3325	5865	710	890	2615	4975	0.525
"	3170	5810	665	835	2505	4975	0.504
"	3066	5379	670	880	2396	4499	0.532
"	2932	5128	605	730	2327	4398	0.529
"	2894	5144	592	720	2302	4424	0.520
"	2817	5086	562	705	2255	4381	0.515

mean $R_2 = 0.523 \pm .004$.

Table 11

Mass Absorption Coefficients of Osmium. (K edge = .167 Å)

$\lambda \times 10^9$ (cms.)	log λ	μ/ρ (gm/cm^2)	log μ/ρ
1.0	.0	2.65	.4232
1.5	.1761	7.45	.8722
2.0	.3010	3.65	.5623
2.5	.3980	6.50	.8129
3.0	.4771	10.0	1.0
K_{α_1} = 1.654		9.55	(extrapolated)
K_{α_2} = 1.703		2.427	(extrapolated)
K_{β_1}' = 1.463		6.998	(extrapolated)
K_{β_2}' = 1.420		6.486	(extrapolated)

Table 12

Mass Absorption Coefficients of Iridium. (K edge = .163Å)

$\lambda \times 10^9$ (cms.)	log λ	μ/ρ (gm/cm^2)	log μ/ρ
1.0	0	2.70	.4314
1.5	.1761	7.65	.8837
2.0	.3010	3.75	.5740
2.5	.3980	6.70	.8261
3.0	.4771	10.50	1.0212
K_{α_1}		2.307	(extrapolated)
K_{α_2}		2.466	(extrapolated)
K_{β_1}'		7.129	(extrapolated)
K_{β_2}'		6.607	(extrapolated)

Table 13

Mass Absorption Coefficients for Hydrogen

$\lambda \times 10^9$ (cms.)	log λ	$\mu/\rho \times 10$ (gm/cm^2)	log μ/ρ
1.0	0	2.8	.4472
1.5	.1761	3.0	.4771
2.0	.3010	3.3	.5185
2.5	.3980	3.4	.5315
3.0	.4771	3.5	.5441
K_{α_1}		3.069	(extrapolated)
K_{α_2},		3.090	"
K_{β_1},		2.985	"
K_{β_2}		2.965	"

Table 14

Mass Absorption Coefficients for Nitrogen

$\lambda \times 10^9$ (cms.)	log λ	$\mu/\rho \times 10$ (gm/cm^2)	log μ/ρ
1.0	0	1.4	.1461
1.5	.1761	1.6	.2041
2.0	.3010	1.8	.2553
2.5	.3980	2.0	.3010
3.0	.4771	2.3	.3617
K_{α_1}		1.667	(extrapolated)
K_{α_2},		1.679	"
K_{β_1},		1.585	"
K_{β_2}		1.567	"

Table 15

Mass Absorption Coefficients of Chlorine

$\lambda \times 10^9$ (cms.)	log λ	$\mu/\rho \times 10$ (gm/cms^2)	log μ/ρ
1.0	0	1.7	.2304
1.5	.1761	2.6	.4150
2.0	.3010	4.2	.6232
2.5	.3980	6.8	.8325
3.0	.4771	10.5	1.0212
K_{α_1}		2.999	(extrapolated)
K_{α_2},		3.126	"
K_{β_1},		2.512	"
K_{β_2}		2.415	"

Table 16

Mass Absorption Coefficients of Aluminium

$\lambda \times 10^9$ (cms.)	log λ	$\mu/\rho \times 10$ (gm/cm^2)	log μ/ρ
1.0	0	1.5	.1761
1.5	.1761	2.0	.3010
2.0	.3010	2.7	.4314
2.5	.3980	3.9	.5911
3.0	.4771	5.6	.7482
3.5	.5441	7.8	.8921
K_{α_1}		2.19	(extrapolated)
K_{α_2},		2.25	"
K_{β_1},		1.94	"
K_{β_2}		1.89	"

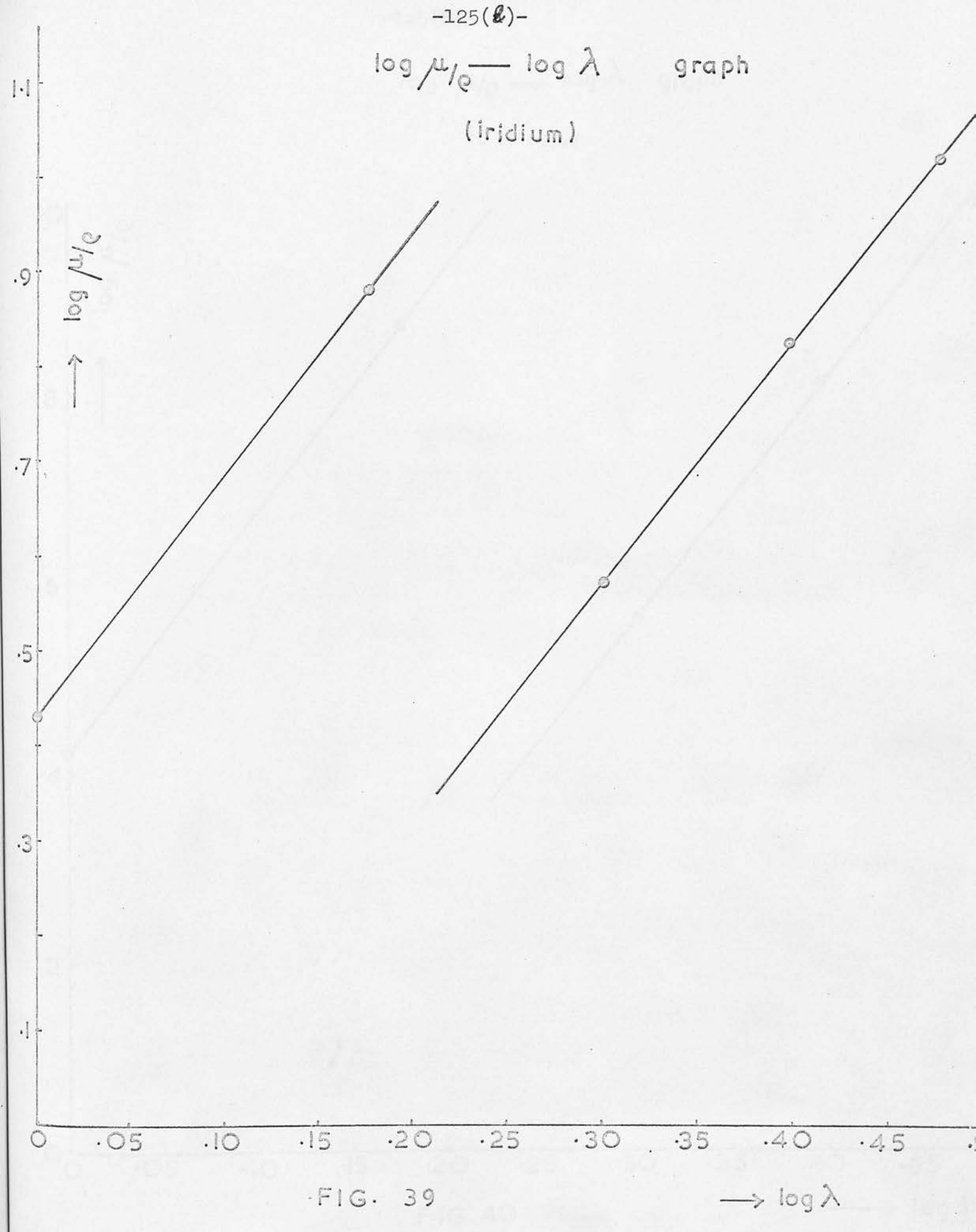
log μ/ρ — log λ graph
(iridium)
log μ/ρ ⟶
1.1
.9
.7
.5
.3
.1
0
.05
.10
.15
.20
.25
.30
.35
.40
.45
⟶ log λ

FIG. 39

log μ/ρ — log λ graph

(osmium)

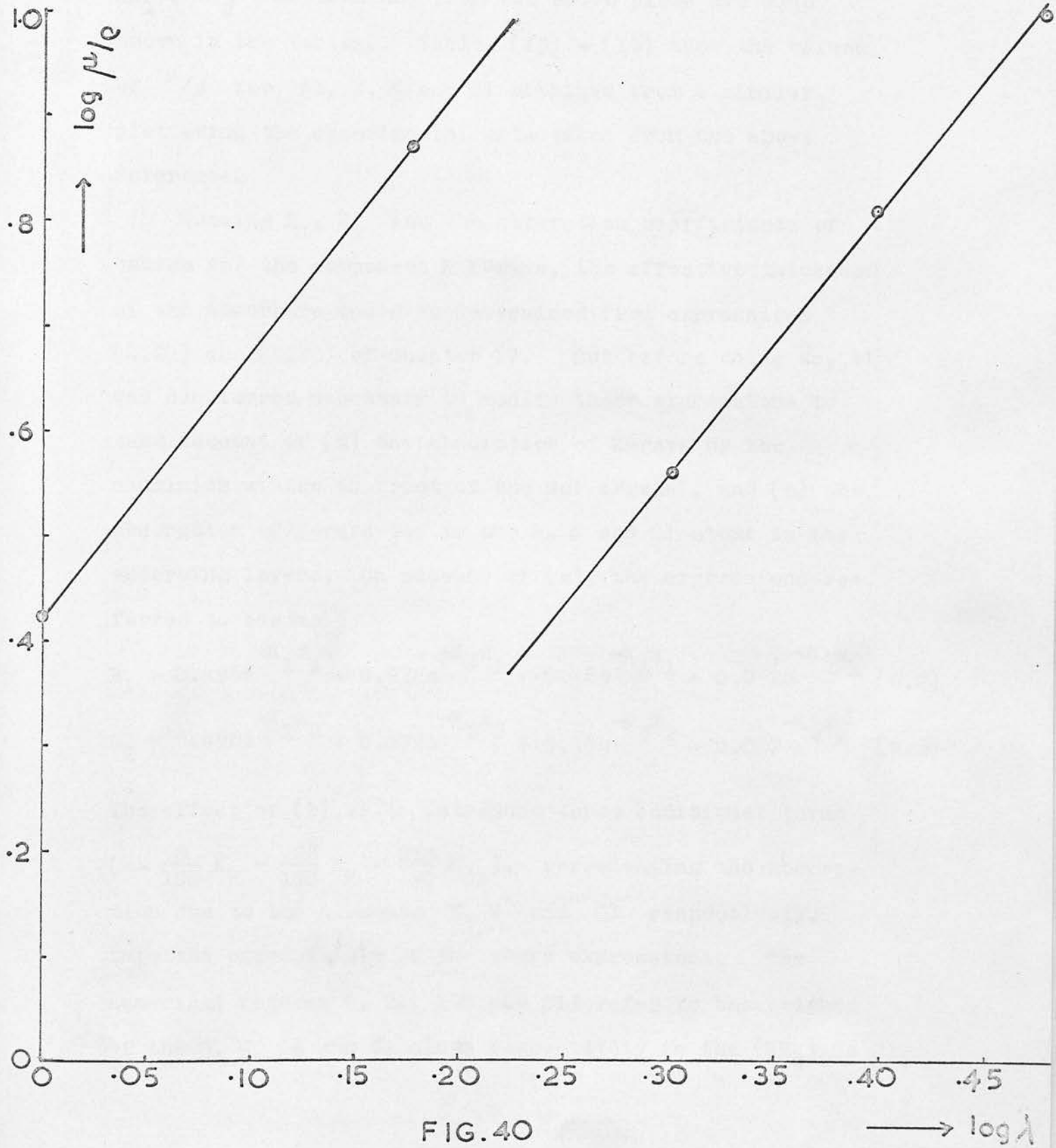

FIG. 40

respectively. The experimental values of μ/ρ were taken from Cauchois'[112] table, part of which is reproduced in Tables (11) and (12). The values of μ/ρ for $K\alpha_1$, $K\alpha_2$, $K\beta_1'$, $K\beta_2'$ as obtained from the above plots are also shown in the tables. Tables (13) - (16) show the values of μ/ρ for Al, H, N and Cl obtained from a similar plot using the experimental data taken from the above reference.

Knowing R_1, R_2 and the absorption coefficients of osmium for the component K X-rays, the effective thickness of the absorbers could be determined from expressions (4.24) and (4.25) of Chapter IV. But before doing so, it was considered necessary to modify these expressions to take account of (a) the absorption of X-rays by the aluminium window in front of the NaI crystal, and (b) the absorption of X-rays due to the H, N and Cl atoms in the absorbing layers. On account of (a), the expressions referred to become

$$R_1 = 0.496e^{-K_1x_1} + 0.272e^{-K_2x_1} + 0.18e^{-K_3x_1} + 0.052e^{-K_4x_1} \quad (6.2)$$

$$R_2 = 0.496e^{-K_1x_2} + 0.272e^{-K_2x_2} + 0.18e^{-K_3x_2} + 0.052e^{-K_4x_2} \quad (6.3)$$

The effect of (b) is to introduce three additional terms $\left(-\frac{8}{190}K_H - \frac{28}{190}K_N - \frac{213}{190}K_{Cl} \right)$, representing the absorption due to the elements H, N and Cl respectively, into the exponentials of the above expressions. The numerical figures 8, 28, 190 and 213 refer to the weights of the H, N, Os and Cl atoms respectively in the $(NH_4)_2OsCl_6$

molecule. Introducing the additional terms into expressions (6.2) and (6.3) and substituting the mass absorption coefficients of the elements involved, gives

$$R_1 = 0.496e^{-9.9234x_1} + 0.272e^{-2.8149x_1} + 0.18e^{-7.3153x_1} + 0.052e^{-6.7922x_1} \quad (6.4)$$

$$R_2 = 0.496e^{-9.9234x_2} + 0.272e^{-2.8149x_2} + 0.18e^{-7.3153x_2} + 0.052e^{-6.7922x_2} \quad (6.5)$$

From a graphical plot of the above equations the thickness of the osmium absorbers corresponding to the observed values of R_1 and R_2 was found to be

$$x_1 = 0.052 \text{ gm./cm.}^2$$

$$x_2 = 0.095 \text{ gm./cm.}^2$$

6.2 Estimation of the Satellite Intensity

After having determined the thickness of the absorbers, the satellite intensity (S) was estimated from equation (4.28) of Chapter IV, which is

$$S = \frac{R_1 - R_1'}{R_1 - e^{-K_s x_1}} = \frac{R_2 - R_2'}{R_2 - e^{-K_s x_2}} \quad .$$

For the iridium measurements, a numerical solution of the above equation gave

$$S = 0.108, \text{ and } K_s = 5.97 \text{ gm./cm.}^2 \quad .$$

But before applying this equation to the osmium measurements, the small absorption of the satellites due to the

other elements in the absorbing layer was considered. This can be taken account of by multiplying the exponentials in the above equation by a factor

$$e^{-\frac{8}{190}K_H x - \frac{28}{190}K_N x - \frac{213}{190}K_{Cl} x} .$$

Thus

$$S = \frac{R_1 - R_1'}{R_1 - e^{-\frac{8}{190}K_H + \frac{28}{190}K_N + \frac{213}{190}K_{Cl}\ x_1}\ e^{-K_s x_1}}$$

$$= \frac{R_2 - R_2'}{R_2 - e^{-\frac{8}{190}K_H + \frac{28}{190}K_N + \frac{213}{190}K_{Cl}\ x_2}\ e^{-K_s x_2}} \qquad (6.6)$$

where K_H, K_N and K_{Cl} refer to the mass absorption coefficients of H, N and Cl respectively for the group of satellites. The satellite energy being not known exactly the absorption coefficients taken in the above expression were those corresponding to the weighted average of the $K\alpha_1$ and $K\alpha_2$ energies. Substituting the extrapolated values of the absorption coefficients and the thickness of the absorbers, equation (6.6) simplifies to

$$S = \frac{R_1 - R_1'}{R_1 - 0.98e^{-.052K_s}} = \frac{R_2 - R_2'}{R_2 - 0.965e^{-.095K_s}}, \qquad (6.7)$$

which on numerical solution with the results of the osmium measurements gave

$$S = 0.234, \quad \text{and} \quad K_s = 8.53 \text{ gm./cm.}^2$$

No account was taken, in the above calculations, of the absorption of satellites by the aluminium window in front of the NaI crystal. This does not, however, involve any significant error as is obvious from the following considerations:-

Let I = Intensity of the normal + satellite K X-rays

S = Fraction of satellites in the incident beam.

A = Fraction of the normal K X-rays transmitted by aluminium.

A_s = Fraction of satellites transmitted by the aluminium.

μ = Absorption coefficient of the absorber for the normal K X-rays.

K = Absorption coefficient of the absorber for the satellites.

x = thickness of the absorber.

Then, for a beam of normal X-rays alone, the intensity reduction,

$$R = \frac{I\, e^{-\mu x} A}{IA} = e^{-\mu x},$$

and for the group of normal and satellite X-rays,

$$R' = \frac{SIe^{-Kx}\, As + (1-S)Ie^{-\mu x}\, A}{SI\, As + (1 - S)IA}$$

or

$$R' = \frac{Se^{-Kx}\, A_s + (1 - S)e^{-\mu x}\, A}{S\, A_s + (1 - S)\, A}$$

$$= \frac{Se^{-Kx}\, A_s + (1 - S)RA}{S\, A_s + (1 - S)A}$$

or $R'S\, A_s + R'A - R'S\, A = Se^{-kx}\, A_s + (1 - S)RA$

$$\text{or } S\left[R'(A_s - A) - e^{-kx} A_s + RA\right] = RA - R'A$$

$$\text{or } S = \frac{(R-R')A}{RA + R'(A_s - A) - A_s e^{-kx}}$$

$$\text{or } S = \frac{R - R'}{R + R'\left(\frac{A_s}{A} - 1\right) - \frac{A_s}{A} e^{-kx}} \quad .$$

Taking $A_s \sim A$,

$$S = \frac{R-R'}{R - e^{-kx}}$$

which is the same as equation (4.28).

6.3 Evaluation of the Constants in the Theoretical Expression for satellite intensity

6.3.1 Electron capture probabilities (F_K, F_{L_I}, etc.):-

The probabilities of a Bi^{206} nucleus decaying to the 3404 keV level of Pb^{206} by K, L_I, L_{II}...etc. capture denoted by F_K, F_{I_I}, $F_{L_{II}}$, ... respectively, were calculated by the formulae given in Wapstra's table[75]. The value of $Q_{E.C.}$, the energy released in the electron capture process was taken to be 3700 keV from Seaborg's table,[113] and the binding energies of the various shells and subshells in Pb were taken from reference (114). Taking the sum of F_K, F_L and F_M to be unity, the following values were obtained:

$$F_K = 0.719$$

$$F_{L_I} = 0.203, \quad F_{L_{II}} = 0.017, \quad F_{L_{III}} = 0$$

$$F_M = 0.061 \quad .$$

The probabilities of capture from the M shells have been taken together and those from shells beyond M ignored.

6.3.2 Probability of a K vacancy producing a vacancy in the L_i shell:-

As defined in Section 4.2, A_{Li} is the probability of a K vacancy producing a vacancy in the Li shell (i = I, II, III) either by Auger process or by radiative process, and hence will be given by the sum of the absolute probabilities for the two processes. The absolute intensities of the lead K X-rays calculated from a knowledge of their relative intensities[75] and K-shell fluorescence yield[75] are shown in the table below:-

Table 17

K X-rays	Relative Intensity	Absolute Intensity	Fluorescence Yield
$K_{\alpha_1} = K\text{-}L_{III}$	1.0	0.476	$\omega_K = 0.956$
$K_{\alpha_2} = K\text{-}L_{II}$	0.553	0.263	
$K_{\beta_1}' = (K\text{-}M_{III}, K\text{-}M_{II})$	0.355	0.169	
$K_{\beta_2}' = (K\text{-}N_{III}, K\text{-}N_{II})$	0.102	0.048	

Neglecting the probabilities of Auger transitions to shells higher than M, it follows from the definition of ω_K that

$$KLL + KLM + KMM = 1 - \omega_K \quad .$$

Taking $\frac{KLX}{KLL} \simeq \frac{KLM}{KLL} = 0.56$ for $Z = 82$ as experimentally observed by Herrlander et al.[115], and

$\frac{KMM}{KLL} = 0.06$ estimated from a graph reproduced in Wapstra's table[75], gives for lead the absolute probabilities

$$KLL = 0.027$$

$$KLM = 0.015$$

and $$KMM = 0.002 .$$

In the approximation considered, both of the Auger processes, KLL and KLM, can shift a K vacancy to any of the L subshells. Since no experimental data on the KLL Auger line intensities were available for lead, those for bismuth reported by Mladjenovic and Slätis[67] (see Table 18) were used to give the following values of the relative probability of a K vacancy shifting to L_I, L_{II} and L_{III} shells by an Auger process:-

$$K \rightarrow L_I = 1 + 1 + 1.8 + 1.1 = 4.9$$

$$K \rightarrow L_{II} = 1.8 + .2 + .2 + 1.6 = 3.8$$

$$K \rightarrow L_{III} = 1.1 + 1.6 + .8 + .8 = 4.3 .$$

With the calculated value of the KLL group probability, the absolute probability for the above vacancy shifts become

$$K \rightarrow L_I = 0.0203$$

$$K \rightarrow L_{II} = 0.0158$$

$$K \rightarrow L_{III} = 0.0178$$

Table 18

Observed Relative Intensities of the KLL Auger lines: Z=83

Line	Relative Intensity
KL_1L_1	1.0
KL_1L_2	1.8
KL_1L_3	1.1
KL_2L_2	0.2
KL_2L_3	1.6
KL_3L_3	0.8

Table 19

Calculated Intensities of KLM Auger Lines : Z = 83

Line	Relative Intensity	Absolute Intensity Calculated from KLM=.015	Absolute Intensity Calculated from KLM+KMM =.017
KL_1M_1	.31	.0010	.0011
KL_1M_2	.19	.0006	.0007
KL_1M_3	.37	.0011	.0013
KL_1M_4, KL_1M_5	.05	.0002	.0002
KL_2M_1	.16	.0005	.0006
KL_2M_2	.07	.0002	.0002
KL_2M_3	.93	.0029	.0032
KL_2M_4, KL_2M_5	.32	.0010	.0011
KL_3M_1	.32	.0010	.0011
KL_3M_2	.80	.0025	.0028
KL_3M_3	.85	.0026	.0030
KL_3M_4, KL_3M_5	.52	.0016	.0018

The situation is still more difficult in the KLM group where no experimental data has been reported on line intensities for an element close to lead. However, Asaad and Burhop[67] have done some theoretical calculations for bismuth which are shown in Table (19). Also shown in this table are the absolute intensities of the lines calculated on taking the total intensity of the KLM group to be 0.015. The line intensities gave the following values for the absolute probability of a K-vacancy shifting to the L_I, L_{II} and L_{III} shells in the KLM Auger process:-

$K \rightarrow L_I$ = .0010 + .0006 + .0011 + .0002 = .0029

$K \rightarrow L_{II}$ = .0005 + .0002 + .0029 + .0010 = .0046

$K \rightarrow L_{III}$ = .0010 + .0025 + .0026 + .0016 = .0077

The total absolute probability of a K vacancy giving rise to a vacancy in the L shells either by X-ray emission or an Auger transition (KLL and KLM) is shown below:-

Table 20

	X-ray Contribution	KLL Auger contribution	KLM Auger contribution	Total
$A_{L_I} = K \rightarrow L_I$ =	0 +	.0203 +	.0029 =	0.0232
$A_{L_{II}} = K \rightarrow L_{II}$ =	0.263+	.0158 +	.0046 =	0.2884
$A_{L_{III}} = K \rightarrow L_{III}$ =	0.476+	.0178 +	.0077 =	0.5015

6.3.3 Probability of a K vacancy shifting to M_j shells:

From the intensity of the KLM Auger lines and $K_{\beta_1'}$ X-rays given in the last section, the following values for the total probability of a K vacancy giving rise to a vacancy in the M shells were obtained:-

Table 21

	X-ray Contribution	KLM & KMM Auger Contribution	Total
$B_{M_I} = K \rightarrow M_I$	= 0 +	0.0028	= 0.0028
$B_{M_{II}} = K \rightarrow M_{II}$	= 0.057+	0.0037	= 0.0607
$B_{M_{III}} = K \rightarrow M_{III}$	= 0.112+	0.0075	= 0.1195
$B_{M_{IV,V}} = K \rightarrow M_{IV,V}$	= 0 +	0.0031	= 0.0031

6.3.4 Probability of an L vacancy giving rise to a vacancy in an M_j shell:-

Table (22) shows the relative intensities of L X-rays taken from measurements made on tungsten (Z = 74) quoted by Compton and Allison[116]. The absolute intensities shown in this table have been calculated on taking, for lead, the mean L shell fluorescence yield, $\omega_L = 0.39$ measured by Parratt[93]. As already pointed out in Section 3.2, no theoretical calculations for the intensities of the L Auger lines have yet been done. Experimental data is also scanty. Only two experimental measurements are

Table 22

Observed Intensities of the L X-rays: Z = 74

Line	Relative Intensity	Absolute Intensity
$L_{III} - M_V$	.74	.097
$L_{III} - M_{IV}$	.08	.010
$L_{II} - M_{IV}$	.82	.107
$L_{III} - N_V$	.15	.019
$L_I - M_{III}$	.43	.056
$L_I - M_{II}$	.27	.035
$L_I - M_{IV}$	.04	.005
$L_I - M_V$	.04	.005
$L_I - N_{II}$	.08	.010
$L_I - N_{III}$	.11	.014
$L_{II} - M_I$	.02	.002
$L_{II} - N_I$	.01	.001
$L_{II} - N_{IV}$	.15	.019
$L_{III} - M_I$	.02	.002
$L_{III} - N_1$	.01	.001

known to the author, (1) by Haynes et al.[72] for bismuth, and (2) by Toburen et al.[71] for platinum. The line assignments in the bismuth measurements are very ambiguous, and also the results quoted have large errors on them. On the other hand, the platinum measurements seem to be more reliable, and hence these results were used in the calculations of C_{M_j}. The relative intensities of the L Auger lines for platinum taken from the measurements of Toburen et al. are reproduced in Table (23). Following a procedure similar to the one described in Section 6.3.2, the absolute probabilities (C_{M_j}) of an L vacancy giving rise to a vacancy in the M_j shells either by radiative process or by Auger transitions (LMM, LMN or LMO) were calculated.

The values of C_{M_j} are shown in the table below:-

Table 24

	X-ray Contribution		Auger Contribution		Total
C_{M_I} = L→M_I	= .004	+	.160	=	.164
$C_{M_{II}}$ = L→M_{II}	= .035	+	.131	=	.166
$C_{M_{III}}$ = L→M_{III}	= .056	+	.293	=	.349
$C_{M_{IV}}$ = L→M_{IV}	= .122	+	.165	=	.287
C_{M_V} = L→M_V	= .102	+	.214	=	.316

Energies and relative intensities of the L-Auger transitions of platinum

Assignment	Relative intensities	Assignment	Relative intensities	Assignment	Relative intensities
$L_3M_1M_1$	0	$L_3M_1O_{4,5}$	2.0 ±0.7	$L_3M_2O_{2,3}$	1.3 ±0.4
$L_3M_1M_2$	1.5 ±0.8	$L_3M_3N_2$		$L_1M_4M_4$	
$L_3M_2M_2$	1.0 ±0.8	$L_1M_1M_4$	4.9 ±0.5	$L_1M_1N_3$	
$L_3M_1M_3$	4.10±0.35	$L_2M_3M_4$	7.7 ±0.5	$L_1M_4M_5$	6.9 ±0.6
$L_3M_2M_3$	12.0 ±0.3	$L_3M_3N_3$	1.6 ±0.4	$L_1M_5M_5$	1.4 ±0.3
$L_3M_1M_4$	2.3 ±1.5	$L_1M_1M_5$		$L_2M_1N_{4,5}$	1.01±0.15
$L_3M_1M_5$		$L_2M_3M_5$		$L_2M_2N_3$	
$L_3M_3M_3$	17.1 ±1.5	$L_3M_4O_1$		$L_2M_3N_1$	
$L_3M_2M_4$	0.7 ±0.7	$L_3M_2N_6$	2.0 ±0.4	$L_2M_1N_{6,7}$	1.61±0.30
$L_3M_2M_5$	3.7 ±1.0	$L_3M_2N_7$		$L_2M_2N_{4,5}$	
$L_2M_1M_1$	1.0 ±0.8	$L_3M_2O_{2,3}$		$L_2M_3N_{2,3}$	0.61±0.30
$L_3M_3M_4$	14.9 ±1.0	$L_1M_3M_3$	5.1 ±1.0	$L_2M_2N_{6,7}$	
$L_3M_3M_5$	18.9 ±0.9	$L_3M_2O_{4,5}$		$L_1M_1N_{4,5}$	1.56±0.30
$L_2M_1M_2$	2.2 ±1.6	$L_3M_3N_4$		$L_2M_3N_{4,5}$	
$L_3M_4M_4$	(1.4)	$L_1M_2M_4$	0.7 ±0.2	$L_3N_1N_3$	
	13.0 ±3.0	$L_3M_3N_5$		$L_2M_3N_{1,2}$	
$L_2M_2M_2$	(11.6)	$L_3M_4N_1$		$L_3N_{2,3}N_3$	2.97±0.39
$L_3M_4M_5$	34.6 ±4.0	$L_1M_2M_5$	1.0 ±0.3	$L_2M_1N_{2,3}$	
$L_1M_1M_1$		$L_3M_5N_1$		$L_3N_1N_{4,5}$	
$L_2M_1M_3$	18.4 ±2.2	$L_3M_4N_2$	0.3 ±0.2	$L_3N_3N_{4,5}$	5.8 ±0.75
$L_3M_5M_5$		$L_2M_4M_4$	5.9 ±0.8	$L_3M_{4,5}N_{4,5}$	
$L_1M_1M_2$	1.0 ±0.7	$L_3M_5N_2$		$L_3N_4N_{4,5}$	
$L_2M_2M_3$	7.8 ±0.6	$L_3M_3O_1$		$L_3N_{2,3}N_{6,7}$	1.98±0.29
$L_3M_1N_1$		$L_3M_4N_3$		$L_3N_5N_5$	
$L_3M_1N_2$		$L_3M_3N_6$	15.2 ±0.7	$L_2M_1N_{6,7}$	
$L_2M_1M_4$		$L_3M_3N_7$		$L_2M_5N_{6,7}$	
$L_1M_2M_2$	2.8 ±0.8	$L_3M_3O_{2,3}$		$L_3N_4N_{6,7}$	0.66±0.08
$L_3M_1N_3$		$L_2M_4M_5$		$L_1M_3N_{6,7}$	
$L_2M_1M_5$		$L_3M_5N_3$	0.2 ±0.15	$L_1M_{4,5}N_{4,5}$	1.18±0.12
$L_3M_2N_1$		$L_3M_3O_{4,5}$		$L_3N_{6,7}N_{6,7}$	
$L_1M_1M_3$	1.9 ±0.3	$L_2M_5M_5$	1.7 ±0.4	$L_1M_4N_{6,7}$	0.41±0.10
$L_2M_3M_3$	2.7 ±0.3	$L_1M_3M_4$			
$L_3M_2N_2$		$L_3M_4N_4$			
$L_3M_1N_4$	4.0 ±0.7	$L_3M_4N_5$	6.4 ±0.5		
$L_3M_1N_5$		$L_1M_3M_5$			
$L_2M_2M_4$		$L_3M_5N_4$	11.3 ±0.4		
$L_3M_2N_3$	1.0 ±0.4	$L_3M_5N_5$			
$L_2M_2M_5$	6.0 ±0.6	$L_2M_1N_1$			
$L_1M_2M_3$	2.0 ±0.7	$L_3M_4O_1$	0.65±0.60		
$L_3M_1O_1$		$L_3M_4N_6$			
$L_3M_3N_1$		$L_3M_4N_7$			
$L_3M_1N_6$		$L_3M_4O_{2,3}$			
$L_3M_1N_7$	1.1 ±0.6	$L_2M_1N_2$			
$L_3M_2N_4$		$L_3M_5O_1$	2.1 ±1.0		
$L_3M_1O_{2,3}$		$L_3M_5N_6$			
$L_3M_2N_5$		$L_3M_4O_{4,5}$			
		$L_3M_5N_7$			

Table 23.

6.3.5 Level widths and disintegration constants of the atomic levels in lead:-

From the brief review presented in Section 3.6 it is evident that there is a great paucity of experimental data on the atomic level widths - particularly for the L and M levels. The only complete measurement of L and M level widths for lead reported in an abstract form is by Shrader[88]. Geiger et al.[99] have criticised his values as being inconsistent with their measurements for Sm and those of Parratt[89] and Richtmyer et al.[90] for Ag and Au respectively. The general trends of M-widths in other elements do indicate that Shrader's values for M_I, M_{II} and M_{III} level widths are rather low. That the value of the K level width in lead ($\sim$50 eV) suggested by the early measurements is also very low, is shown by more recent measurements of Latyshev et al.[97] for Bi ($\Gamma_K = 67 \pm 5$eV) and the theoretical predictions of Listengarten for Z = 81 ($\Gamma_K = 65.7$ eV). For comparison the experimental data on level widths for some elements is presented in Table (25).

The widths of the various atomic levels in lead for the purpose of the present experiment were evaluated as described below:-

Of all the level width measurements using the method of X-ray spectroscopy, those for Ag and Au by Parratt and Richtmyer et al. seem to be most reliable. The recent measurements of K and M level widths in Sm by Geiger et al., and of K level width in Bi by Latyshev et al. using β-spectrometers are also fairly precise. Hence, the K

Table 25

Some Observed and Calculated Level Widths (eV)

Level	Experimental					Calculated		
	Shrader Z = 82	Parratt Z = 47	Richtmyer Z = 79	Geiger et al. Z = 62	Latyshev et al. Z = 83	Listengarten Z = 65	Z = 81	Z = 92
K		8.0	54.0	17	67.0	27.1	65.7	112.8
L_I	11.0	5.3	8.7	-	-	-	-	-
L_{II}	4.6	2.2	3.7	-	-	-	-	-
L_{III}	5.1	2.0	4.4	-	-	-	-	-
M_I	10.5	8.6	15.5	14	-	-	-	-
M_{II}	10.8	0.6	10.7	4.7	-	-	-	-
M_{III}	7.3	1.3	12.1	7.7	-	-	-	-
M_{IV}	4.7	0.2	4.2	-	-	-	-	-
M_V	3.8	0.34	3.5	-	-	-	-	-

level width in lead was obtained from a graphical plot (see Fig. 41) of the K widths for Ag, Sm, Au and Bi. The width so obtained in 64.0 eV, which is in quite good agreement with the theoretical predictions of Listengarten, and consistent with the experimental value of ω_K mentioned earlier. The widths of M_I, M_{II} and M_{III} levels were obtained from an extrapolation of the corresponding plots for Ag, Sm and Au shown in Fig. 42. The L_I level width was calculated from line width measurements shown in Fig. 43, which is reproduced from an article by A. Bril[95]. The Lβ line widths for Z = 82 as read from the curves of this Figure were

$L\beta_1$ $(L_{II} - M_{IV})$ = 9.25 eV

$L\beta_{II}$ $(L_{III} - N_V)$ = 12.15 eV

$L\beta_{III}$ $(L_I - M_{III})$ = 21.5 eV

$L\beta_{IV}$ $(L_I - M_{II})$ = 23.0 eV

Using the values of M_{II} and M_{III} widths obtained from Fig. 42 in the mean of $L\beta_{III}$ and $L\beta_{IV}$ widths, gave the width of the L_I level as 10 eV. This is in good agreement with the value of 9.3 eV predicted from Fig. 44 reproduced from Kinsey's article[117]. The widths of L_{II}, L_{III}, M_{IV} and M_V levels in lead measured by Shrader agree reasonably well with the widths of the $L\beta_1$ and $L\beta_{II}$ lines mentioned above and hence were accepted for the present purpose. The widths of the various atomic levels and their disintegration probabilities calculated from equation

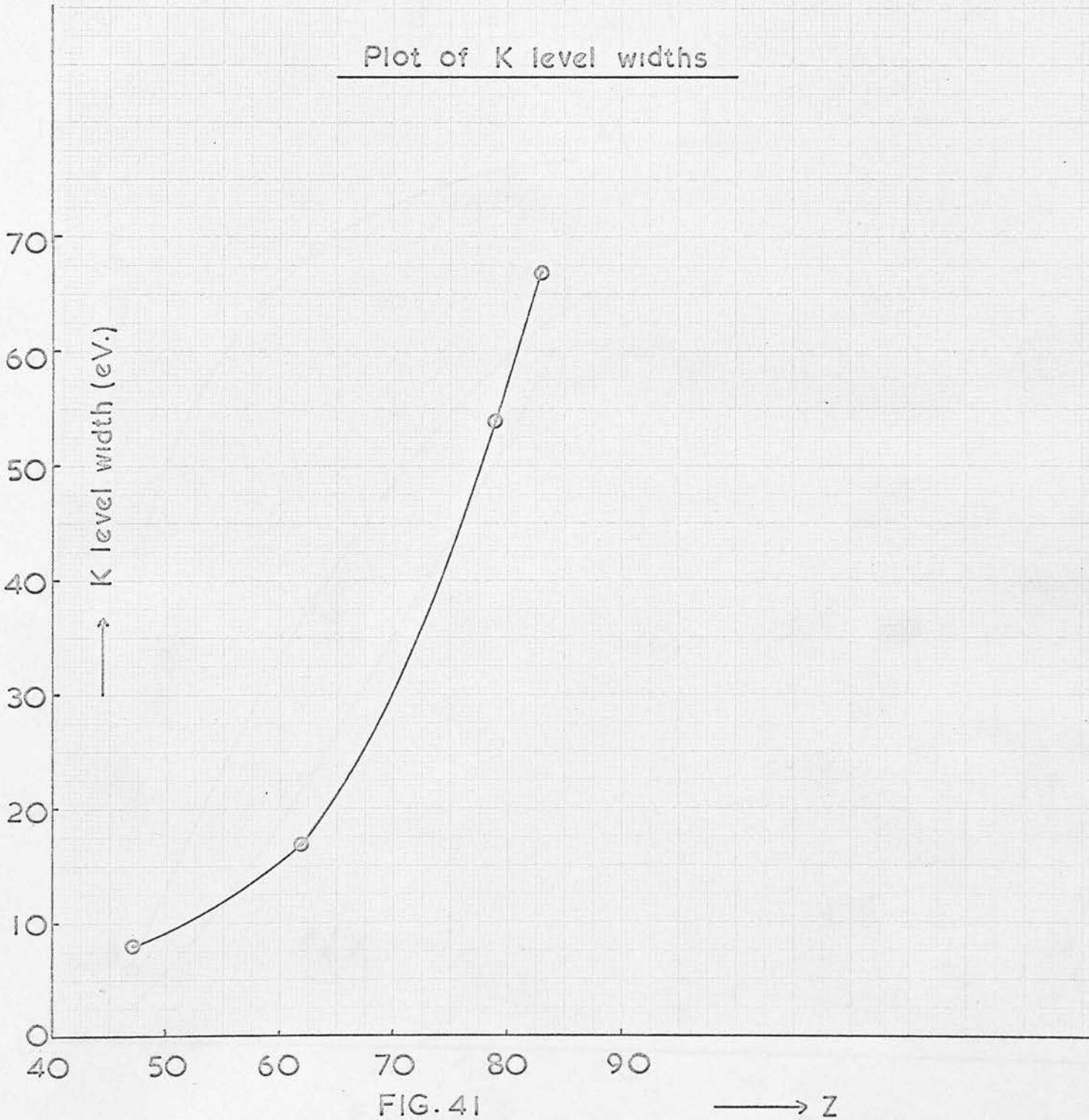
Plot of K level widths
70
60
50
40
30
20
10
0
K level width (eV.)
40
50
60
70
80
90
Z

FIG. 41

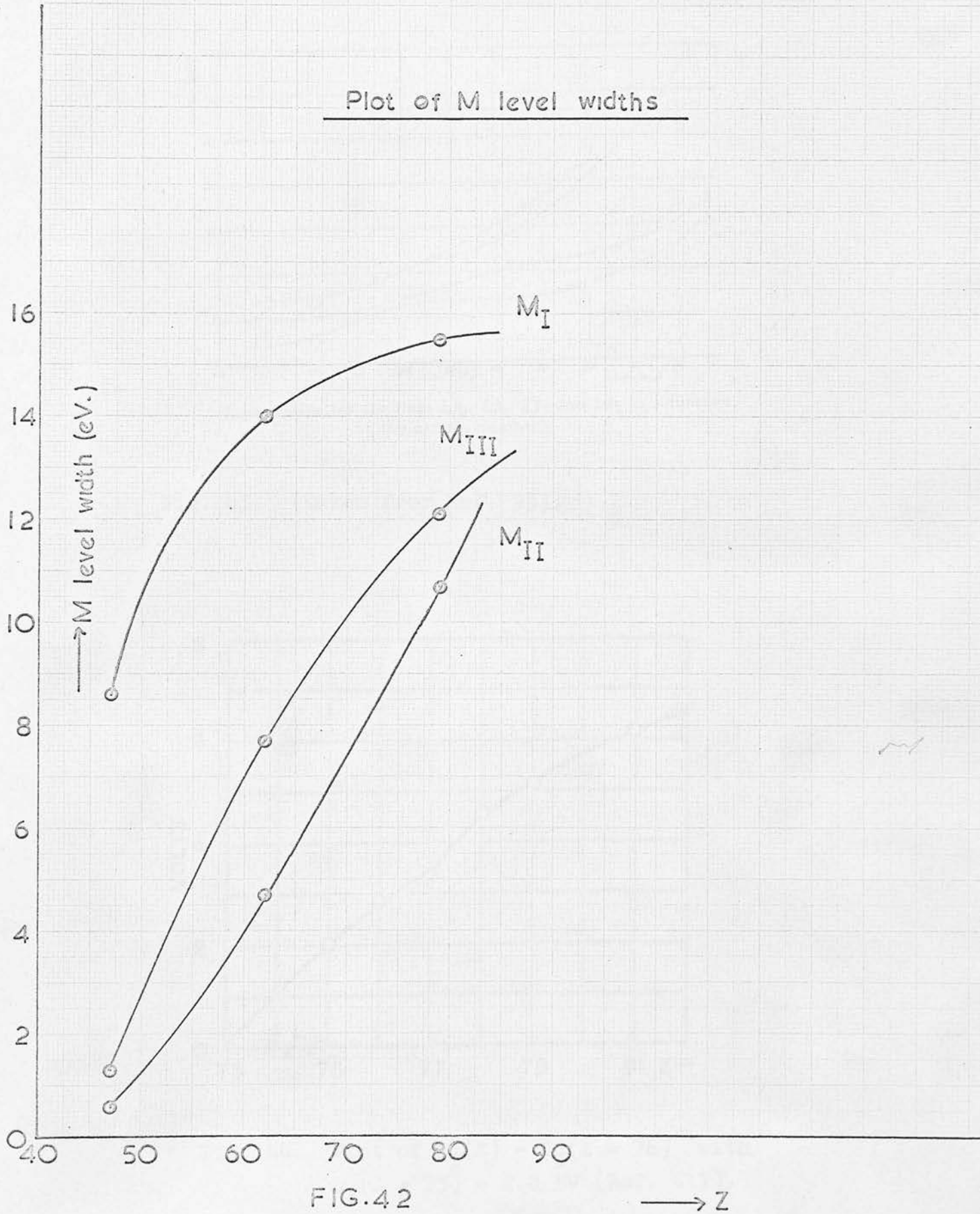
Plot of M level widths
16
14
12
10
8
6
4
2
0
M level width (eV.)
M_I
M_{III}
M_{II}
40
50
60
70
80
90
Z

FIG. 42

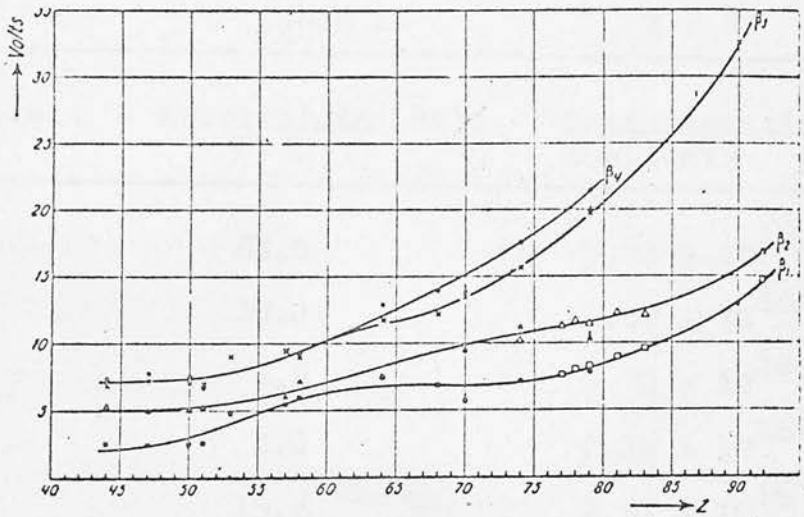

Line widths for the lines $L\beta_3$, $L\beta_4$, $L\beta_1$ and $L\beta_2$ as a function of the atomic number.

Fig. 43. (Taken from Ref. 95).

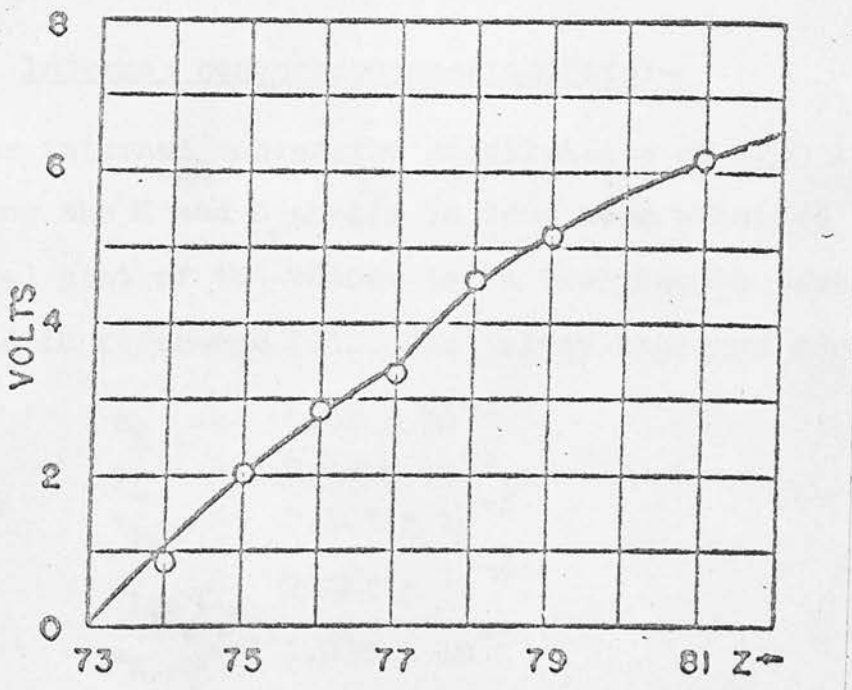

Fig. 44. Plot of $L_I(Z) - L_I(Z = 76)$ with $L_I(Z = 73) = 2.8$ eV (Ref. 117).

(1.1) of Chapter 1 are summarised below:-

Table 26 Z = 82

Atomic Level	Level width (eV)	Disintegration Constants ($sec.^{-1}$)
K	64.0	9.73×10^{16}
L_I	10.0	1.52×10^{16}
L_{II}	4.6	0.70×10^{16}
L_{III}	5.0	0.76×10^{16}
M_I	15.6	2.37×10^{16}
M_{II}	11.9	1.81×10^{16}
M_{III}	12.7	1.93×10^{16}
M_{IV}	4.7	0.71×10^{16}
M_V	3.8	0.58×10^{16}

6.3.6 Internal conversion coefficients:-

The internal conversion coefficients of 1720 keV E1 γ-ray for the K and L shells in lead were obtained from a graphical plot of the values taken from Rose's table reproduced in reference (1). The values obtained were

$$\alpha_K = 0.86 \times 10^{-3}$$
$$\alpha_L = 0.16 \times 10^{-3}$$
$$\alpha_{L_I} = 0.123 \times 10^{-3}$$
$$\alpha_{L_{II}} = 0.012 \times 10^{-3}$$
$$\alpha_{L_{III}} = 0.028 \times 10^{-3}$$

6.4 Lifetime of the 1720 keV E1 Transition

Using the experimental value of the satellite intensity (S) and the calculated values of the various probabilities, equation (4.23) was solved numerically for Υ, the transition probability of the 3404 keV level of Pb^{206}. The results obtained for the two sets of measurements were as follows:-

For iridium measurements: $\Upsilon = 0.102 \times 10^{16}$ sec.$^{-1}$

For osmium measurements : $\Upsilon = 0.28 \times 10^{16}$ sec.$^{-1}$

The transition probability (Υ) thus obtained is the sum of the probabilities of all the Υ-transitions originating from the 3404 keV level. The transition probability (λ) for the 1720 keV E1 Υ-ray can be calculated from the relation

$$\lambda = \frac{\Upsilon \times I}{I_T} ,$$

where I = intensity of the 1720 keV Υ-ray,

and I_T = sum of the intensities of all the Υ-rays from the 3404 keV level.

With the relative intensities indicated in the decay scheme of Bi^{206} (see Fig. 33, Chapter V), the above expression gives the following results for the 1720 keV E1 transition:-

For iridium measurements: $\lambda = 0.068 \times 10^{16}$ sec.$^{-1}$

mean life, $\tau = 15 \times 10^{-16}$ sec.

For osmium measurements : $\lambda = 0.19 \times 10^{16}$ sec.$^{-1}$

mean life, $\tau = 5 \times 10^{-16}$ sec.

6.5 Estimate of Error

The error in the observed value of the mean life depends on the error ΔS in the estimation of satellite intensity (S). But the expression for the satellite intensity in terms of the measured intensity reductions also involves the mass absorption coefficient (K_s) of the absorbers for the satellites, the error in which is not known. The procedure adopted, therefore, was to obtain as a first approximation, the limits on S from an expression which involved the measured intensity reductions and the thickness of the absorbers, but not K_s. These limits were then used to obtain the errors in K_s and $e^{-K_s x}$. Knowing the errors in $e^{-K_s x}$ and the measured intensity reductions, the conventional method was applied to estimate the final value of ΔS and hence the limits on the mean life of the nuclear transition. The details of the calculation are given below:-

The expression for the satellite intensity in terms of R_1, R_2 etc. is

$$S = \frac{R_1 - R_1'}{R_1 - e^{-K_s x_1}} = \frac{R_2 - R_2'}{R_2 - e^{-K_s x_2}}$$

in which the factors (~ 1) multiplying the exponentials have been dropped.

This gives

$$e^{-K_s} = \left(\frac{R_1' + SR_1 - R_1}{S}\right)^{1/x_1}$$

$$e^{-K_s} = \left[\frac{R_2' + SR_2 - R_2}{S}\right]^{1/x_2}$$

Therefore,

$$\left[\frac{R_1' + SR_1 - R_1}{S}\right]^{1/x_1} = \left[\frac{R_2' + SR_2 - R_2}{S}\right]^{1/x_2}$$

Taking log of both sides and on rearranging the terms,

$$x_2 \log(R_1' + SR_1 - R_1) - x_2 \log S = x_1 \log(R_2' + SR_2 - R_2) - x_1 \log S.$$

Differentiating with respect to R_1, R_2 etc. (but not x_1 and x_2),

$$\frac{x_2}{R_1' + SR_1 - R_1}\left[\Delta R_1' + R_1 \Delta S + S\,\Delta R_1 - \Delta R_1\right] - x_2 \frac{\Delta S}{S}$$

$$= \frac{x_1}{R_2' + SR_2 - R_2}\left[\Delta R_2' + R_2 \Delta S + S\,\Delta R_2 - \Delta R_2\right] - x_1 \frac{\Delta S}{S}$$

or

$$\left[\frac{x_2 R_1}{R_1' + SR_1 - R_1} - \frac{x_1 R_2}{R_2' + SR_2 - R_2} + \frac{x_1}{S} - \frac{x_2}{S}\right] \Delta S$$

$$= \frac{x_1}{R_2' + SR_2 - R_2}\left[\Delta R_2' - (1-S)\Delta R_2\right] - \frac{x_2}{R_1' + SR_1 - R_1}\left[\Delta R_1' - (1-S)\Delta R_1\right].$$

Putting $F_1 = \dfrac{x_1}{R_2' + SR_2 - R_2}$ and $F_2 = \dfrac{x_2}{R_1' + SR_1 - R_1}$

in the above gives,

$$\left[F_2R_1 - F_1R_2 - \frac{(x_2-x_1)}{S}\right]\Delta S = F_1\left[\Delta R_2' - (1-S)\Delta R_2\right]$$

$$- F_2\left[\Delta R_1' - (1-S)\Delta R_1\right] \qquad (6.8)$$

This then is the expression which will give the limits on S without taking into account the error in K_s. Substituting the values of the various quantities for iridium measurements in equation (6.8) gave,

$$\Delta S = \pm .007$$

Since $S = 0.108$, S lies between 0.115 and 0.101 as a first approximation. Using these values of S in the expression $S = \frac{R_1 - R_1'}{R_1 - C}$, where C has been substituted for $e^{-K_s x_1}$, the following values for K_s and C were obtained:-

$S = .115$, $C = .498$, $K_s = 5.71$ gm./cm.^{2}

$S = .101$, $C = .467$, $K_s = 6.24$ gm./cm.^{2}

also for obsd $S = .108$, $C = .483$, $K_s = 5.97$ gm./cm.^{2}

Thus, $C = 0.483 \pm .016$.

This can now be used to estimate the final value of ΔS. since,

$$S = \frac{R_1 - R_1'}{R_1 - e^{-K_s x_1}} = \frac{R_1 - R_1'}{R_1 - C}$$

$$\left(\frac{\Delta S}{S}\right)^2 = \left[\frac{\Delta(R_1 - R_1')}{R_1 - R_1'}\right]^2 + \left[\frac{\Delta(R_1 - C)}{R_1 - C}\right]^2 \qquad (6.9)$$

From the results mentioned in Section (6.1),

$$\Delta(R_1 - R_1') = .007, \quad R_1 - R_1' = .026 .$$

Hence, $$\frac{\Delta(R_1 - R_1')}{R_1 - R_1'} = 0.27 .$$

Also, $$\Delta(R_1 - C) = \sqrt{(.005)^2 + (.016)^2}$$

$$= .017$$

and $$R_1 - C = .724 - .483$$

$$= .241 .$$

Therefore, $$\frac{\Delta(R_1 - C)}{R_1 - C} = .071 .$$

Substituting in (6.9),

$$(\frac{\Delta S}{S})^2 = (.27)^2 + (.071)^2$$

which gives

$$(\frac{\Delta S}{S}) = .28, \text{ i.e. error in S is about 28\%.}$$

Therefore,

$$\Delta S = .28 \times .108$$

$$= .030 .$$

Hence $$S = 0.108 \pm .030.$$

Thus S lies between .138 and .078. The extreme values of S correspond to the mean life 11×10^{-16} sec. and 20×10^{-16} sec. respectively for the 1720 keV E1 transition.

Applying the above procedure of error estimation to the data of osmium measurements gave the following results:-

(i) K_s lies between 8.10 and 9.31 gm./cm.^{2}, the observed value being 8.53 gm./cm.^{2}.

(ii) $C = 0.629 \pm .02$.

(iii) $\frac{\Delta S}{S} = 0.46$, i.e. error in S obtained from osmium measurements is about 46%.

Since observed $S = 0.234$, $\Delta S = .107$

or $S = .234 \pm .107$, i.e. S lies between .341 and .127. The extreme values of S in this case correspond to the mean life 3×10^{-16} and 12×10^{-16} seconds respectively for the 1720 keV E1 transition.

The final values of the mean life of the 1720 keV E1 transition in Pb^{206} as obtained in the present experiment from the two sets of measurements may be summarised as follows:-

From iridium measurements:

$$\tau = \begin{cases} 20 \times 10^{-16} \text{ sec (upper limit)} \\ 15 \times 10^{-16} \text{ " (observed value)} \\ 11 \times 10^{-16} \text{ " (lower limit} \end{cases}$$

From osmium measurements:

$$\tau = \begin{cases} 12 \times 10^{-16} \text{ sec (upper limit)} \\ 5 \times 10^{-16} \text{ " (observed value)} \\ 3 \times 10^{-16} \text{ " (lower limit)} \end{cases}$$

CHAPTER VII

DISCUSSION AND CONCLUSIONS

As described in Chapter IV, the method of lifetime measurement presented in this thesis is applicable to the E1 transitions of energy $\geq$ 1 Mev in medium and high Z K-capture nuclei. In such cases, nuclear and atomic level lifetimes are of comparable order and hence the nuclear transitions of this type are expected to be associated with K X-ray satellites. The fact that the nuclear level lifetime can be expressed in terms of atomic level lifetimes permits an estimation of the former as already discussed. That the satellite emission does occur has been experimentally demonstrated by the observed differences in the intensity reductions R_1 and R_1' on the one hand, and R_2 and R_2' on the other, for two different absorbers. The intensity reductions suggest that the K X-ray satellites are certainly very close to the K-edge of the absorbers used in the experiment. The mean energy of the satellite group according to the experimental values of intensity reductions for the iridium absorber is 76.03 keV whereas for osmium it lies in the range 75.8 - 80.05 keV. These values agree well with the Wentzel-Druyvestyn type of estimate for the lead KK satellite energy (~76 keV) calculated by Slater's method[111]. The experimental values of K_s = 5.97 gm./cm.^{2} and 8.53 gm./cm.^{2} for iridium and osmium absorbers respectively are also within the expected limits 2.2 - 9.4 and 2.3 - 9.8 for the two absorbers. The relatively small

intensity reduction observed in the case of osmium is mainly because the $K\alpha_1$ component of the lead K X-rays lies on the higher energy side of the osmium K edge. While calculating the satellite intensity (S) from equation (4.28), it was found that the value of S depended very sensitively on the difference between R_1 and R_1' or R_2 and R_2'. The relatively large error in estimation of S from osmium measurements as compared with that from iridium results is in accordance with this observation.

Since the osmium absorbers were made from a powder of ammonium chlorosmanate, any uncertainty in its thickness or uniformity might also have contributed to the results. It was, however, not possible to take into account the effects of these contributions. For these reasons, more reliance may be reposed on the results of iridium than those of osmium measurements. The osmium results can then be regarded as a corroborative piece of evidence in favour of the iridium results. The general contribution of the X-ray Compton background and of the Compton background in the neighbourhood of the conversion line to the coincidences observed, from which the satellite intensity was estimated has already been discussed. As explained in Section 5.11, the procedure adopted for recording coincidences was meant to eliminate the contributions from such effects. Another possibility of some contribution to the observed satellite intensity arises from the theory of Primakoff and Porter[110] already referred to in Section 3.5.4. According to these authors, when a nucleus decays

by orbital electron capture, there is a definite probability for the simultaneous excitation of a non-captured orbital electron as a consequence of sudden charge alteration. The probability per K capture for the production of a double hole in the K shell by this process is, however, very small ($P_{KK} \simeq {}^{3}/_{16Z^2}$). The only nucleus in which such a process has been observed is Ge^{71} for which the theory predicts a value of 10^{-4} for P_{KK}. For lead, P_{KK} will be $\sim 10^{-5}$, and hence even if such an effect exists, its contribution to the satellite intensity will be obviously negligible.

The mean life of the 1720 keV E1 transition as obtained in the present experiment from the iridium measurements is 15×10^{-16} seconds. The single particle estimate for this transition gives $\tau = .54 \times 10^{-16}$ seconds. The observed value, therefore, corresponds to a retardation of about 27. As mentioned in Section 1.5, two values for the lifetime of this transition are already available. Brunner et al. have reported a retardation of about 50, while Wu et al. obtained a retardation of about 600. None of these authors have quoted errors on the results reported. But since both these results were obtained by observations on monoenergetic positrons, they are expected to involve huge uncertainties. It has already been remarked in Section 2.7 that the estimation of lifetime by this method relies on the theoretical value of monoenergetic K-positron emission coefficient ($a^{K}_{e^+}$) for which the results of Lombard and Rys[59] differ from those

of Sliv by a factor of 2. Besides, the estimation of K-positron intensity in the presence of a large background also introduces a considerable error. The X-ray satellite method, on the other hand, used in the present experiment does not involve such uncertainties. The quantities involved in the calculations are either experimentally known or can be computed with a reasonable degree of accuracy. The value of lifetime obtained by this method is, therefore, expected to be better than that given by the method of monoenergetic positron emission.

The results of the present experiment seem to favour the value reported by Brunner et al. rather than the value obtained by Wu et al. In order to see whether the observed retardation of the 1720 keV E1 transition in Pb^{206} is reasonable, reference may be made to section 1.5 where the retardation of E1 transitions has been briefly discussed. The relatively small retardation obtained in the present experiment rules out any possibility of K-forbiddenness as the cause. This statement is supported by Rusinov's empirical rule (eq. (1.30), Chapter I), regarding the K-forbiddenness of E1 transitions in even-even nuclei. Moreover, the nucleus $_{82}Pb^{206}$ with only two neutrons short of doubly closed shell is less likely to be described in terms of the Nilsson model. The unusually high first excited state of Pb^{208} and the slow electric quadrupole transition rates in other lead isotopes provide strong evidence for the rigidity of the core and a weak surface coupling in these nuclei. The

works of Alburger and Pryce[118], True and Ford[119] and Kearsley[120] have shown that a very successful description of the energy levels in Pb^{206} up to about 3 Mev can be obtained from simple shell model considerations where the interaction between the two neutron holes is taken as a perturbation and the effects of nuclear deformations are ignored. Thus, most of the energy levels shown in the Bi^{206} decay scheme (Fig. 33) are accounted for in terms of simple two hole neutron configurations. The upper two levels (3403 and 3280 keV), however, have been ascribed by True and Ford to the core excitation formed, possibly by proton configurations $(s_{\frac{1}{2}})^{-1} h_{9/2}$ and $(d_{3/2})^{-1} h_{9/2}$ respectively. Such an assignment involves a change in the orbitals of three nucleons (2 neutrons and 1 proton) which is very unlikely because many particle transitions are generally expected to be slower compared with single-particle transitions by several orders of magnitude. The result of the present experiment seems to strengthen the confidence in the shell model description of the Pb^{206} nucleus. An application of the method described in this work to the lifetime measurement of the 1863 keV E1 transition in Bi^{205} may further strengthen this contention.

REFERENCES

1. M.E. Rose, Table of Internal Conversion Coefficients, 1958.
2. L.A. Sliv and I.M. Band, Coefficients of Internal Conversion of γ-radiation, 1956.
3. J.M. Blatt and V.F. Weisskopf, Theoretical Nuclear Physics.
4. S.A. Moszkowski, α, β and γ-ray Spectroscopy, Ch. XV, Vol. I (1965). Ed. K, Siegbahn.
5. M. Goldhaber and J. Wenesser, Annual Review of Nuclear Science 5, 1, 1955.
6. N.B. Gove, Nuclear Spin Parity Assignments (1966), 83-103, Ed. Gove and Robinson.
7. M.G. Mayer and J.H.D. Jensen, α, β and γ-ray Spectroscopy, Ch. IX, Vol. I (1965).
8. O. Nathan and S.G. Nilsson, α, β and γ-ray Spectroscopy, Ch. X (1965).
9. B. Mottelson, Proc. Rehovoth Conference on Nuclear Structure (1958).
10. A.K. Kerman, Nuclear Reactions, Chapter IX, Vol. I. Ed. Endt and Demeur.
11. J.M. Aranjo, Nuclear Reactions, Chapter IV, Vol. II, Ed. Endt.and Demeur.
12. Jha and Leonard, Phys. Rev. 136, 1585, 1964.
13. Sorensen, Phys. Rev. 132, 2270, 1963.
14. De Shalit, Phys. Rev. 105, 1531, 1957.
15. D.H. Wilkinson, Proc. Rehovoth Conference on Nuclear Structure (1958).
16. G. Alga, Phys. Rev. 100, 432, 1955.
17. Grin and Pavlichankov, Nuclear Physics 65, 686, 1965.
18. Vergnes and Rasmussen, Nuclear Physics 62, 233, 1965.
19. Bernthal and Rasmussen, Nuclear Physics 101A, 513, 1967.
20. Conlon et al., Nuclear Physics 104A, 213, 1967.
21. Brunner et al. Phys. Rev. Letters 2, 207, 1959.

REFERENCES (Contd.)

22. Wu et al., Phys. Rev. 130, 1069, 1963.

23. A.S. Bokosah, Ph.D. Thesis, Edinburgh University, 1965.

24. N. Feather and Dunworth, Proc. Roy. Soc. A168, 566, 1938.

25. Z. Bay, Phys. Rev. 77, 419, 1950.

26. T.D. Newton, Phys. Rev. 78, 490, 1950.

27. R.E. Bell, α, β and γ-ray Spectroscopy, Vol. II (1965).

28. Goldring, Nuclear Instruments & Methods 11, 29 , 1961.

29. R.C. Mobley, Phys. Rev. 88, 360, 1952.

30. Fowler and Good, Nuclear Instruments & Methods 7, 245, 1960.

31. S. Devons et al., Nature 164, 586, 1949.

32. J. Thirion and V.L. Telegdi, Phys. Rev. 92, 1253, 1953.

33. Sieveriens and Hanna, Phys. Rev. 104, 1612, 1956.

34. S. Devons et al., Proc. Phys. Soc. A68, 18, 1955.

35. L.G. Elliot and R.E. Bell, Phys. Rev. 74, 1869, 1948; Ibid. 76, 168, 1949.

36. J. Burde and S.G. Cohen, Phys. Rev. 104, 1093, 1956.

37. P.B. Moon, Proc. Phys. Soc. A64, 76, 1951.

38. R. Metzger, Prog. in Nucl. Phys. 7, 54, 1959.

39. L. Grodzin, Phys. Rev. 109, 1014, 1958.

40. Palathingal, Phys. Rev. 136B, 1553, 1964.

41. G.B. Beard & W.H. Kelley, Nuclear Physics 43, 523, 1963.

42. H. Frauenfelder, The Mössbauer Effect (1962).

43. R.L. Mössbauer, α, β and γ-ray Spectroscopy, Ch. XXI, Vol. II (1965).

44. Stephens, Diamond & Perlman, Phys. Rev. Letters 3, 435, 1959.

45. K. Alder et al., Reviews of Mod. Phys. 28, 432, 1956.

46. N.P. Heydenburgh and G.M. Temmer, Ann. Rev. Nucl. Science, 6, 77, 1956.

REFERENCES (Contd.)

47. R. Huby, Rep. Progr. Phys. 21, 59, 1958.

48. D. Alburger, α, β and γ-ray Spectroscopy. Ch. XII, Vol. I (1965).

49. P.H. Stelson and F.K. McGowan, Ann. Rev. Nucl. Sc. 13, 163, 1963.

50. N.P. Heydenburgh and G.M. Temmer, Phys. Rev. 100 150, 1955.

51. P.H. Stelson & F.K. McGowan, Phys. Rev. 99, 112, 1955.

52. D.H. Rester et al., Nucl. Phys. 22, 104, 1961.

53. B. Elbeck et al., Nucl. Phys. 19, 523, 1960.

54. W.C. Barber, Ann. Rev. Nucl. Sc., 12, 1, 1962.

55. G.R. Bishop, Nuclear Structure and Electromagnetic Interactions (1964). Ed. N. Macdonald.

56. R.H. Helm, Phys. Rev. 104, 1466, 1956.

57. H.L. Crannel and T.A. Griffy, Phys. Rev. 136B, 1580, 1964.

58. L.A. Sliv, Soviet Physics J.E.T.P. 25, 7, 1963.

59. R. Lombard & F. Rys, Nucl. Phys. 31, 163, 1962.

60. S.S. Vasilenko et al., Soviet Physics J.E.T.P. 12, 672, 1961.

61. C.F. Perdristat et al., Nucl. Phys. 31, 160, 1962.

62. S. Shimuzu et al., Nucl. Phys. 54, 265, 1964.

63. C.F. Perdristat et al., Nucl. Phys. 31, 157, 1962.

64. E.H.S. Burhop, The Auger Effect and Other Radiationless Transitions (1952).

65. I. Bergstrom and C. Nordling, α, β and γ-ray Spectroscopy, Ch. XXV, Vol. II (1965).

66. M.A. Listengarten, Izvestiya Akad. Nauk 24, 1041, 1960.

67. W.N. Asaad and E.H.S. Burhop, Proc. Phys. Soc. 71, 369, 1958.

68. W.N. Asaad, Proc. Roy. Spc. 294, 555, 1959.

69. M.A. Listengarten, Bull. Acad. Sciences, U.S.S.R., (English Translation) 25, 803, 1961.

70. M.A. Listengarten Do. 26, 182, 1962.

71. L.H. Toburen and R.G. Albridge, Nucl. Phys. A90, 529, 1967.

72. S.K. Haynes et al., Nucl. Phys. A90, 573, 1967.

73. C. Broyles, D. Thomas & H. Haynes, Phys. Rev. 89, 715, 1953.

74. J. Laberrigue, Frolow et al., J. Phys. Radium. 17, 530, 1956.

75. A. Wapstra et al., Nuclear Spectroscopy Tables (1959).

76. R.W. Fink et al., Rev. Mod. Phys. 38, 513, 1966.

77. E.H.S. Burhop, Proc. Roy. Soc. A148, 272, 1935.

78. L. Pincherle, Nuovo Cimento 12, 81, 1935.

79. H. Massey and E.H.S. Burhop, Proc. Roy. Soc. A153, 661, 1936.

80. H.L. Hagedoorn and A.H. Wapstra, Nucl. Phys. 15, 146, 1960.

81. Ross, Cochran, Hughes and Feather, Proc. Phys. Soc. A68, 612, 1955.

82. P.B. Rao and B. Craseman, Phys. Rev. 137B, 64, 1965.

83. L. Salgueiro et a l., Proc. Phys. Soc. 77, 657, 1961.

84. W.N. Asaad, Nucl. Phys. 66, 494, 1965.

85. F.K. Richtmyer, S.W. Barnes and E. Ramberg, Phys. Rev. 46, 843, 1935.

86. J.H. Williams, Phys. Rev. 45, 71, 1934.

87. F.K. Richtmyer, & S.W. Barnes, Phys. Rev. 46, 352, 1934.

88. R.E. Shrader, Phys. Rev. 49, 644, 1936.

89. L.G. Parratt, Phys. Rev. 54, 99, 1938.

90. E.G. Ramberg & F.K. Richtmyer, Phys. Rev. 51, 913, 1937.

91. J.A. Bearden & T.M. Snyder, Phys. Rev. 59, 162, 1941.

92. J.N. Cooper, Phys. Rev. 61, 234, 1942.

93. L.G. Parratt, Rev. Mod. Phys. 31, 616, 1959.

94. D. Coster and A. Bril, Physica IX, 84, 1942.

95. A. Bril, Physica XIII, 481, 1947.

96. H. Slätis and G. Lindström, Phys. Rev. 88, 1429, 1952.

97. G.D. Latyshev et al., Bull. Acad. of Sciences U.S.S.R. (English Translation) 20, 324, 1956.

REFERENCES (Contd.)

98. J.H. Dijkstra and De Vries, Nucl. Phys. 23, 524, 1961.

99. J.S. Geiger et al., Nucl. Phys. 48, 97, 1963.

100. E.J. Callan, Bull. Amer. Phys. Soc. 7N, 416, 1962.

101. F.R. Hirsh, Rev. Mod. Phys. 14, 45, 1942.

102. I. Edamato, Science Reports, Tohuku University A2, 56, 1950.

103. R.D. Deslattes, Phys. Rev. 133A, 399, 1964.

104. Cauchois and Hulubei, Tables des Constantes Numerique.
104(a) Shaw & Parratt – Phys. Rev. 50, 1010, 1936 104(c) Pearsall - Phys. Rev 46, 697, 1934.
104(b) Randall & Parratt – Phys. Rev. 57, 790, 1940.

105. D.J. Candlin. Proc. Phys. Soc. A68, 322, 1955.

106. Z. Horak, Proc. Phys. Soc. A77, 980, 1961.

107. V.P. Sachenko and V.F. Demekhin, Soviet Physics, J.E.T.P. 22, 532, 1966.

108. T. Aberg, Phys. Rev. 156, 35, 1967.

109. W. Von Oertzen, Zeitschrift für Physik 182, 130, 1964.

110. H. Primakoff and F.T. Porter, Phys. Rev. 89, 930, 1953.

111. J.C. Slater, Phys. Rev. 36, 57, 1930.

112. Y. Cauchois, Table of Mass Absorption Coefficients.

113. G.T. Seaborg et al., Rev. Mod. Phys. 585, 30, 1958.

114. Table of Critical X-ray Absorption Energies. Lewis Slack, Naval Research Laboratory, Washington, D.C. (1952).

115. C.J. Herrlander et al., Ark. Fys. 17, 315, 1960.

116. A.H. Compton and S.K. Allison, X-rays in Theory and Experiment (1935).

117. B.B. Kinsey, Canad. Jour. Res. 26, 404, 1948.

118. D.E. Alburger and M.H.L. Pryce, Phys. Rev. 95, 1482, 1954.

119. W.W. True and K.W. Ford, Phys. Rev. 109, 1675, 1958.

120. M.J. Kearsley, Nucl. Phys. 4, 157, 1957.